Acta Biomaterialia 207 (2025) 468–494

Contents lists available at ScienceDirect

Acta Biomaterialia

journal homepage: www.elsevier.com/locate/actbio

Review article

Beyond gadolinium: The potential of manganese nanosystems in MRI and multimodal imaging agents

Lorenzo Tei [a], Mauro Botta [a,*], Carlos F.G.C. Geraldes [b,c,*]

[a] Department of Science and Technological Innovation, University of Piemonte Orientale, Alessandria, Italy
[b] Department of Life Sciences and Coimbra Chemistry Center (CQC-IMS), Faculty of Science and Technology, University of Coimbra, Coimbra, Portugal
[c] CIBIT—Coimbra Institute for Biomedical Imaging and Translational Research, University of Coimbra, Coimbra, Portugal

ARTICLE INFO

Keywords:
Manganese ions
MRI contrast agents
Nanoparticles
Relaxivity
Multimodal agents
Theranostic nanoplatforms

ABSTRACT

Manganese-based nanoparticles (Mn-NPs) hold great promise as MRI contrast agents and components of theranostic nanoplatforms, serving as a promising alternative to the more established gadolinium(III)-based nanosystems. This potential stems from their unique physicochemical properties and improved safety profile. This review introduces the fundamental principles of relaxation to highlight the key physicochemical characteristics of Mn-based nanosystems that influence their effectiveness. We primarily examine two oxidation states of manganese, Mn(II) and Mn(III), to demonstrate the efficacy of Mn-NPs as relaxation probes, with a brief discussion of one Mn(IV) system. Subsequently, we review recent studies on Mn-NP-based MRI contrast agents, focusing on the correlation between nanoparticle structure and the oxidation state of the paramagnetic centre. For Mn(II), the most common strategy involves utilizing stable Mn-chelates anchored to or encapsulated within the nanoparticles. In contrast, for the higher oxidation state, Mn(III), Mn(III)-porphyrin and phthalocyanine NPs are the primary non-Mn oxide nanosystems of choice. Regarding nanoplatform composition, Mn(II)-based platforms utilizing lipids (micelles or liposomes), polysaccharides (nanogels), dendrimers, metal-organic frameworks, inorganic NPs, and silicas are among the most frequently investigated. While numerous *in vitro* and *in vivo* animal MRI studies of Mn nanoplatforms have been reported, none have yet received clinical approval. We describe innovative surface modification and functionalization procedures designed to improve NP characteristics (*e.g.*, size, stability, dispersibility, relaxivity, targeting, and toxicity) and impart multifunctionality for multimodal imaging. These strategies may provide valuable guidance for the development of Mn-NPs toward future clinical applications, particularly in cancer theranostics.

Statement of significance: This review provides a critical analysis of the current landscape of Mn-based nanoparticles, which are increasingly being explored as MRI contrast agents and for multimodal imaging. This growing interest is largely driven by concerns over the potential toxicity and environmental impact of traditional Gd-based systems. The review introduces the key structural and dynamic parameters that determine the effectiveness of these nanosystems, highlighting their direct relationship with molecular design. It also examines the crucial stability and kinetic inertness requirements that influence their development. By critically discussing selected recent examples across a diverse range of nanosystems, including micelles, liposomes, silica-based platforms, and MOFs, this review identifies existing challenges and provides key insights to guide their future clinical translation.

1. Introduction

The numerous and key innovations in constructing complex nanometre-sized particles and in understanding their size-dependent chemical-physical characteristics have promptly directed the attention of researchers towards their applications in biomedicine. In particular, the development of nanoprobes for bioimaging has seen rapid advancement over the past two decades [1–4]. Various imaging modalities are now available for preclinical applications, including magnetic resonance imaging (MRI), optical imaging (OI), computed tomography (CT), positron emission tomography (PET), single photon emission computed tomography (SPECT), and ultrasound (US). Each of

* Corresponding authors.
E-mail addresses: mauro.botta@uniupo.it (M. Botta), geraldes@ci.uc.pt (C.F.G.C. Geraldes).

https://doi.org/10.1016/j.actbio.2025.05.058
Received 7 February 2025; Received in revised form 16 May 2025; Accepted 22 May 2025
Available online 25 May 2025

these modalities has distinctive characteristics in terms of resolution, limit of detection, sensitivity, acquisition time and management costs [5]. Furthermore, each of them greatly benefits from the use of nanoparticles (NPs) as contrast enhancing agents (CAs) able to improve the characteristics of the images and therefore their diagnostic efficacy. To this purpose, a wide range of nanomaterials have been designed, developed and utilized [6–8]. Although various properties of NPs are a direct consequence of their surface to volume ratio, shape and size, it is well known that the functionalization of their surface with suitable ligands or chemical groups is able to modulate characteristics such as solubility, colloidal stability, targeting ability, the mechanism of action that defines their functionality (optical, magnetic, etc.), biocompatibility and biodistribution. The surface of NPs is also relevant for the possibility it offers to provide them with multiple functions, *e.g.* to act as nanoprobes for combined imaging modalities or as CAs and therapeutic transport vehicle (theranostic) [9].

Among various imaging modalities, MRI has rapidly acquired a prominent role because of its many favourable characteristics. These include non-invasiveness, high intrinsic contrast, lack of use of ionizing radiation during the scan, unlimited penetration, outstanding resolution in the time and space (mm scale) domains and ability of application to any area of the body. The development of the technique and its widespread diffusion in clinical diagnostics have also been favoured by the ready availability of effective CAs [10,11]. CAs are commonly used in MRI to increase the image contrast, reduce the acquisition time and improve confidence of the diagnosis. In clinical practice, these consist of hydrophilic, low molecular weight paramagnetic complexes formed by Gd^{3+} ions and octadentate polyaminocarboxylic ligands, both open chain and macrocyclic. All these complexes share the characteristic of having their metal ion with a bound water molecule in the inner coordination sphere, which undergoes rapid chemical exchange with the bulk water in solution [12]. This exchange process enables the paramagnetic relaxation effect of the Gd(III) ion to be transmitted to the nearby solvent water molecules surrounding the complex, ultimately leading to shorter nuclear magnetic relaxation times T_1 and T_2 [13]. This rapid shortening of relaxation times near the CAs alters (increases) the T_1-weighted MRI signal intensity, thereby enhancing image contrast.

CAs are also widely used in preclinical studies and MR-based molecular imaging investigations. Often a key objective of these studies concerns the targeting of sites of biological importance present at very low concentrations and this raises the problem of the intrinsic low sensitivity of the MRI technique. To overcome this limitation, effective approaches to amplify the signal and contrast have been developed over the years. By far the most common and successful strategy aims to find the best compromise between two interdependent objectives: a) use a macromolecular or nanosized platform to attach a very large number of paramagnetic complexes to the same unit (10^3–10^5 metal-complexes per particle) [14]; b) maximize the effectiveness (relaxivity) of the individual metal complexes, used as building blocks, optimizing their physicochemical characteristics [15]. At typical MRI magnetic field strength values, the ability of a CA to increase contrast depends mainly on its rotational dynamics. Low molecular weight clinical CAs tumble rapidly, and their efficacy is rather limited. The reduction in molecular tumbling, measured by the rotational correlation time τ_R, produces a greater capacity of the Gd-complex to decrease the T_1 and T_2 values of the water solvent. Therefore, binding many Gd-complexes to a nanoparticle (NP) entails not only confining a very high number of paramagnetic centres on a single scaffold but also, due to the very slow molecular tumbling of the NP (slow rotation; long τ_R values), the efficacy of each of the conjugated Gd complexes is much greater than that of the free complex (fast rotation; short τ_R values). Over the past two decades, a variety of paramagnetic nanosystems have been designed, prepared and tested both *in vitro* and *in vivo*, generally demonstrating enhanced effectiveness. The interest of the researchers was directed both to NPs in which the metal complexes were linked to (or incorporated into) organic materials (*e.g.* dendrimers, micelles, liposomes, proteins, polymers, nanogels, dendrimersomes, viral capsids) and to NPs based on inorganic/organic hybrid systems (*e.g.* gold NPs, quantum dots (QDs), metal oxides, fluorides, zeolites, mesoporous or amorphous silicas, metal-organic frameworks) [16–19]. While clinical MRI currently relies on Gd-based complexes, other paramagnetic metal ions from both the lanthanoid and early transition metal series have been explored for the development of NPs in preclinical MRI applications. In particular, those Mn-based have been extensively studied and many systems have been designed, prepared and tested [19–21].

Manganese, a first row transition metal with the electronic configuration $[Ar]3d^5 4s^2$, can exist in multiple oxidation states within the 0 to +7 range. The magnetic properties of Mn ions arise from the distribution of unpaired electrons across the five d orbitals, with the degree of paramagnetism increasing with the number of unpaired electrons. In its high-spin divalent state, Mn(II) serves as an effective paramagnetic relaxation agent due the high values of its electronic spin quantum number value ($S = 5/2$) and effective magnetic moment ($\mu_{eff} = 5.9$ μB/atom), as well as favourable electronic relaxation times (relatively long, in the 0.1–1 ns range) and fast exchange kinetics of water molecules within the metal ion's coordination sphere. These advantageous properties position Mn(II)-based systems as a viable alternative to Gd(III) analogues for use as MRI CAs [22,23]. Mn(II) typically coordinates with donor atoms such as carboxylate oxygen and amino nitrogen, while the harder and smaller Mn^{3+} ion favours strongly electron-donating ligands like phenolate or catecholate groups. In fact, in the Mn(III) oxidation state, manganese, with its $3d^4$ electronic configuration, typically forms high-spin ($S = 2$) paramagnetic complexes. These compounds exhibit a reduced effective magnetic moment ($\mu_{eff} = 4.9$ μB per atom). In fact, their efficiency as relaxation agents is limited by their inherently shorter electronic relaxation times (approximately 10 ps), despite also exhibiting rapid water exchange rates. Additionally, manganese readily reacts with oxygen forming a multiplicity of paramagnetic ions and complexes, such as in the MnO, Mn_3O_4, Mn_2O_3, and MnO_2 Mn oxides, with +2, mixed +2/+3, +3, and +4 Mn oxidation states, respectively. Mn(IV) ($3d^3$ electronic configuration) complexes exhibit lower paramagnetism ($S = 3/2$, $\mu_{eff} = 3.87$ μB/atom) due to the lower number of unpaired electrons. Consequently, the high *in vivo* contrast enhancement observed for MnO_2-like NPs arises from the release of free Mn^{2+} ions upon particle dissolution, which is typically triggered by endogenous stimuli. However, excess free Mn^{2+} ions in the body can cause severe toxicity issues, so it is important that they are stably and safely chelated by a polydentate organic ligand [24]. Manganese is a vital element found in all documented living organisms, serving a crucial function as a cofactor for enzymes and receptors. As an illustration, the enzyme involved in the conversion of water molecules into oxygen during photosynthesis incorporates four manganese ions. In mammalian tissues, manganese is typically present at concentrations ranging from 0.3 to 2.9 mg per gram of wet tissue. The highest levels are found in bones, with progressively lower amounts in the brain, pancreas, kidneys, liver, muscles, and pigment-rich tissues like the retina. Within these tissues, manganese primarily exists in its Mn(II) oxidation state. The average human body comprises around 12 mg of manganese, with a daily intake of approximately 4 mg from various food sources like nuts, bran, whole-grain cereals, tea, and parsley. Proper manganese assimilation is essential for normal growth, function, development, and cellular homeostasis [25]. However, excessive exposure to manganese can result in adverse health effects, including disruptions in redox balance and changes in central nervous system activity. Elevated manganese levels, especially in the brain, can have neurotoxic effects. Its excessive accumulation has been linked to the development of manganism, a neurological disorder that mimics the symptoms of Parkinson's disease [26].

This article reviews recent research on nanosized, Mn-based MRI CAs, with a specific emphasis on the relationship between the structural characteristics of the paramagnetic centres and the properties of the NPs in terms of their effectiveness as relaxation probes. Cutting-edge investigations also encompass approaches involving the surface

modification or functionalization of nanoparticles, aiming to enhance their properties (such as good dispersibility, targeting capabilities, and low toxicity) and achieve multifunctionality. Our focus is primarily directed towards manganese complexes that are either covalently linked to or physically incorporated within organic nanomaterials, as well as nanoparticles constructed from inorganic/organic hybrid systems. Consequently, this review deliberately excludes a detailed discussion of manganese oxides, a class of materials that has been the subject of comprehensive reviews by other researchers over the past decade [27–31]. Furthermore, we have intentionally refrained from extensively analyzing studies that utilize free Mn^{2+} ions as a direct source of MRI signal enhancement. Therefore, our discussion centers on more sophisticated and biocompatible manganese-based contrast agents.

2. General properties of manganese ions used as MRI contrast agents

2.1. Background and theory

2.1.1. Basic principles of paramagnetic relaxation

Relaxivity (r_i, where $i = 1$ or 2) provides a straightforward way to determine how effectively a paramagnetic agent functions as an MRI probe. This parameter quantifies the increase in longitudinal or transverse relaxation rates (R_i, where $i = 1$ or 2) of water protons, adjusted to a standard concentration of 1 mM of the metal ion [11–12]. The observed longitudinal proton relaxation rate (R_1^{obs}) consists of a diamagnetic component corresponding to the contribution of the water solvent (R_1^{w}), and a paramagnetic component, which is directly proportional to the concentration of the paramagnetic ion:

$$R_1^{obs} = R_1^{p} + R_1^{d} = r_1[\mathrm{Mn}] + R_1^{d} \quad (1)$$

Relaxivity (expressed in $mM^{-1}\ s^{-1}$ units) is typically factorized into two contributions, the so-called inner- (r_1^{is}) and outer-sphere (r_1^{os}) terms:

$$r_1 = r_1^{is} + r_1^{os} \quad (2)$$

The outer-sphere term, typically interpreted according to Freed's model, describes the long-range interactions between a paramagnetic metal ion and water molecules diffusing in its vicinity and its contribution to r_1 of Mn-based nanosystems is in most cases negligible, especially at typical MRI fields [13]. The inner-sphere term accounts for the contribution of the q water molecules (where q is one or more) that reside in the metal ion's inner coordination sphere for an average duration of τ_M, commonly in the 10^{-9} to 10^{-6} s range [23,32]. These water molecules exchange with those in the bulk solvent with a rate $k_{ex} = 1/\tau_M$ and this process effectively propagates the nucleus-electron interaction (water protons-Mn ion) to the rest of the solvent.

The inner sphere relaxivity is given by:

$$r_1^{IS} = \frac{p_M}{T_{1M} + \tau_M} \quad (3)$$

where p_M denotes the molar fraction of water molecules belonging to the inner coordination sphere of the Mn ion ($p_M = q$ [M]/55.6), which exhibit a longitudinal nuclear magnetic relaxation time of T_{1M}. This has a pronounced dependence on the Larmor frequency of observation and therefore also the relaxivity is frequency dependent [33]. When considering magnetic fields typically used in MRI (*i.e.*, above 10 MHz), the ^{1}H longitudinal relaxation rate of the water molecule(s) bound to a metal ion can be conveniently calculated using the following equation:

$$\frac{1}{T_{1M}} = \frac{C}{r_H^6}\left[\frac{3\tau_{C1}}{1+\omega_H^2\tau_{C1}^2}\right] \quad (4)$$

$$\frac{1}{\tau_{C1}} = \frac{1}{\tau_R} + \frac{1}{\tau_M} + \frac{1}{T_{1e}} \quad (5)$$

where C groups together a series of constants and, in the case of the Mn (II) ion, corresponds to the value of 2.88×10^{-31} (in CGS units), r_H represents the distance between the manganese ion and the protons of the coordinated water molecule(s), while ω_H denotes the proton Larmor frequency. The overall correlation time τ_{C1} (Eqs. (4) and (5)) encompasses the three mechanisms that contribute to the time-dependent nucleus-electron coupling. These mechanisms are the molecular reorientation (τ_R), water exchange ($k_{ex} = 1/\tau_M$) and electron relaxation (T_{1e}) which is in turn frequency dependent. Due to the dependence of r_1 on the applied magnetic field, the most convenient approach to analyse and evaluate the efficacy of a paramagnetic probe as a potential MRI CA is the measurement of relaxivity as a function of the Larmor frequency over a sufficiently broad range of values. The values of r_1 plotted as a function of ω_H are called NMRD profiles (Nuclear Magnetic Relaxation Dispersion) and are measured using a commercially available instrumentation, the Field Cycling Relaxometer [34,12,13]. The analysis of the NMRD profiles through Eqs. (1)–(5) allows to obtain the molecular parameters that associate the relaxivity with the structural properties and the dynamics of the paramagnetic centres. While in small rapidly rotating complexes τ_R (*ca.* 50–100 ps at 298 K) generally dominates τ_C, in slowly tumbling systems it becomes comparable or even longer than τ_M and/or T_{1e}. This has a profound influence on the shape and amplitude of the ^{1}H NMRD profiles, as can be clearly seen in the simulations below (Fig. 1) relating to a monohydrate Mn(II) complex ($q = 1$) characterized by increasing τ_R values, from 0.05 to 10 ns.

It is of great importance to note that the variation of r_1 with the decrease of the molecular tumbling has a strong dependence on the frequency of observation. As τ_R increases, the relaxivity maximum gradually increases, becomes narrower and moves towards lower frequencies. From these simulations, we can deduce that the Mn(II)-based nanosized systems become less and less effective as T_1 CAs as the frequency increases. Therefore, it makes little sense to draw conclusions about the efficacy of an MRI nanoprobe based on data obtained only at high field, *e.g.* at 3 or 7 Tesla. Furthermore, in low molecular weight complexes T_{1M} (~ 3–7 μs) is very often much greater than τ_M and therefore the water exchange rate is not a factor that limits the achievable r_1. This condition ($\tau_M << T_{1M}$) is known as the fast exchange regime. However, in the case of nanosystems T_{1M} becomes much shorter (due to the lengthening of τ_R) and therefore it could be comparable (intermediate exchange regime) or even longer than τ_M (slow exchange regime) [15]. In these cases, the relaxation enhancement is limited by the water exchange (Eq. (3)), as shown in Fig. 1B. If the system is in the fast exchange regime, then its relaxivity shows a clear increase with decreasing temperature.

Another relevant aspect that can limit the expected relaxation enhancement is the presence of a large component of local rotational motion involving the Mn-chelate linked to a nanosized structure. Weak correlation between global and local motions counteracts the effects associated with increasing molecular size and allows for limited increases in r_1, often only a fraction of those predicted by theory. When this situation occurs, the NMRD profiles can be analysed using the model-free Lipari-Szabo approach to account for rotational dynamics [15]. This model considers the presence of a slow motion (overall rotation of the nanoparticle; τ_{RG}) and a fast motion (local reorientation; τ_{RL}) whose degree of correlation is described by the parameter S^2 (Eqs. (6) and (7)). S^2 assumes values between zero (motions fully independent) and one (strongly correlated motions).

$$\frac{1}{T_{1M}} = \frac{K}{r_H^6}\left[\frac{3S^2\tau_{CG}}{1+\omega_H^2\tau_{CG}^2} + \frac{3(1-S^2)\tau_{CL}}{1+\omega_H^2\tau_{CL}^2}\right] \quad (6)$$

$$\frac{1}{\tau_{CG}} = \frac{1}{\tau_{RG}} + \frac{1}{\tau_M} + \frac{1}{T_{1e}};\quad \frac{1}{\tau_{CL}} = \frac{1}{\tau_{CG}} + \frac{1}{\tau_{RL}} \quad (7)$$

The effects of an increasing difference between global and local motions are shown in Fig. 2, which reports the variation of simulated

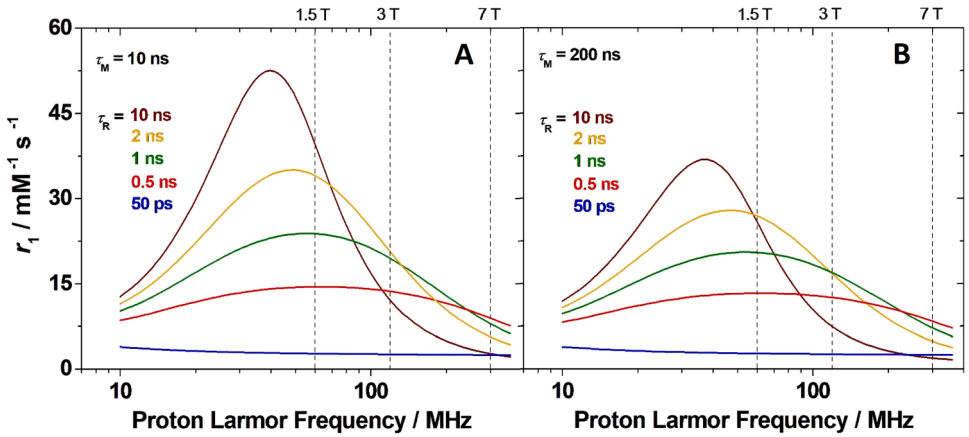

Fig. 1. ^{1}H NMRD profiles calculated for a Mn(II) chelate ($q = 1$) as the rotational correlation time (τ_R) was progressively increased. Other parameters are: $\Delta^2 = 6.9 \times 10^{19}$ s^{-2}, $\tau_V = 28$ ps, $r = 2.83$ Å, $a = 3.6$ Å, $D = 2.3 \times 10^{-5}$ cm^2 s^{-1}. **A**: exchange lifetime $\tau_M = 10$ ns; **B**: exchange lifetime $\tau_M = 200$ ns.

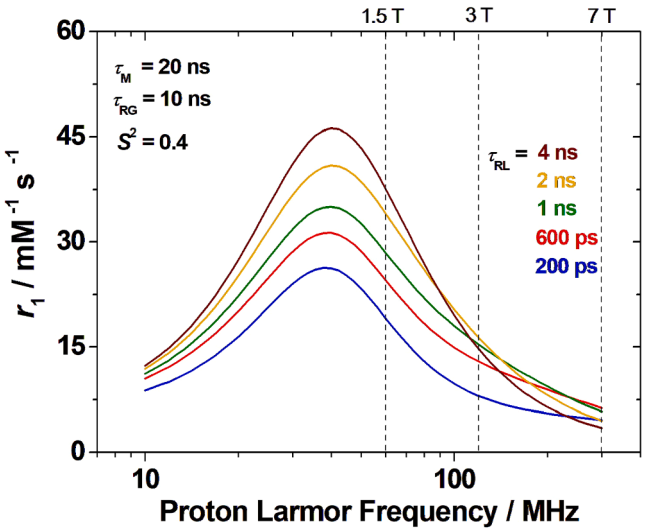

Fig. 2. ^{1}H NMRD profiles for a Mn(II) chelate with $q = 1$ calculated for different values of the local rotational correlation time τ_{RL}. Other parameters are: $\Delta^2 = 6.9 \times 10^{19}$ s^{-2}, $\tau_V = 28$ ps, $r = 2.83$ Å, $a = 3.6$ Å, $D = 2.3 \times 10^{-5}$ cm^2 s^{-1}.

NMRD profiles as a function of τ_{RL} in the high-frequency Larmor region.

In conclusion, the goal of relaxivity enhancement of MRI nanoprobes must consider the need for fine control of several parameters: i) a high number of paramagnetic centres per nanoparticle; ii) an optimal water exchange rate in the metal ion's inner sphere; iii) a good degree of correlation between the local rotational flexibility of the complex and the global tumbling of the nanoparticle.

Finally, the following recommendations should be followed to ensure correct interpretation of the results:

a) Measure R_1 at two or more Larmor frequency values, one in the range 20–80 MHz;
b) Measure R_1 at three or more different temperature values (about 15–45 °C) and identify the exchange regime: slow, intermediate or fast;
c) Determine the concentration of the paramagnetic ion very accurately, preferably using two different procedures.

2.1.2. MRI contrast agents

The clinical success of MRI is associated with the fact that the relaxation rates R_1 ($R_1 = 1/T_1$) and R_2 ($R_2 = 1/T_2$) of mobile tissue water protons vary from tissue to tissue and from pathological to normal tissue [35]. To increase the image contrast between pathological tissue and normal tissue, relaxation-enhancing agents (contrast agents; CAs) are often introduced that selectively influence the T_1 and T_2 relaxation times in these tissues [11]. The mechanism of action of MRI CAs involves the reduction of T_1 and T_2 relaxation times of nuclei (predominantly water) within the target tissue, resulting in their classification as either T_1 or T_2 agents. Paramagnetic Gd(III) and Mn(II) complexes are typical MRI CAs as well as superparamagnetic magnetite particles [13]. By reducing water proton T_1 and/or T_2 relaxation times, these probes enhance contrast in MRI. This manifests as increased signal intensity (brightening) on T_1-weighted images and decreased signal intensity (darkening) on T_2-weighted images. The most used contrast media are paramagnetic positive agents that primarily accelerate the $1/T_1$ longitudinal relaxation rate in the regions where they distribute, allowing brighter T_1-weighted images [36]. Complexes of Dy(III) or Tm(III), superparamagnetic or ferromagnetic nanoparticles behave as negative CAs. In these cases, the predominant effect is the shortening of T_2, resulting in darker appearances of the "enhanced" regions in T_2-weighted images [36].

In addition to r_1 and r_2, the r_2/r_1 ratio (which is always > 1) is a key parameter in identifying MRI contrast agent type. Optimal T_1 agents (for positive contrast) have a ratio near one, whereas T_2 agents have a large ratio (originating negative contrast). At 37 °C and 1 T, this ratio is 1.1 and 1.3 for the clinical CAs $[Gd(DTPA)]^{2-}$ and GdHPDO3A (HPDO3A= (10-(2-Hydroxypropyl)-1,4,7,10-tetraazacyclododecane-1,4,7-triacetate), respectively. Instead, it increases to 1.4 for GdDTPA-17 [37], a dendritic gadolinium chelate carrying 24 ions, and to 2.3 for ultrasmall superparamagnetic iron oxide nanoparticles (AMI-227) [38]. However, r_2 can exhibit a pronounced increase with the applied field and indeed the r_2/r_1 ratio for AMI-227 becomes equal to 42.1 at 4.7 T It follows that the identification of a probe as a T_1 or T_2 agent may depend not only on the nature (magnetic properties) of the metal ion, but also on the molecular dimensions and the Larmor frequency of observation.

The different frequency-dependence of r_1 and r_2 for a slowly tumbling system is shown in the following figure (Fig. 3).

2.1.3. Basic properties of manganese ions

The manganese-based compounds of interest for the design and development of magnetic probes for MRI applications refer to oxidation states II, III and IV of the element, strictly in order of relevance and diffusion.

Mn(II). The Mn(II) ion is by far the most widely used in the design of macromolecular or nanoparticle systems. Mn(II) chelates offer a compelling combination of characteristics for effective MRI probe design. Their high chemical stability across a broad pH range

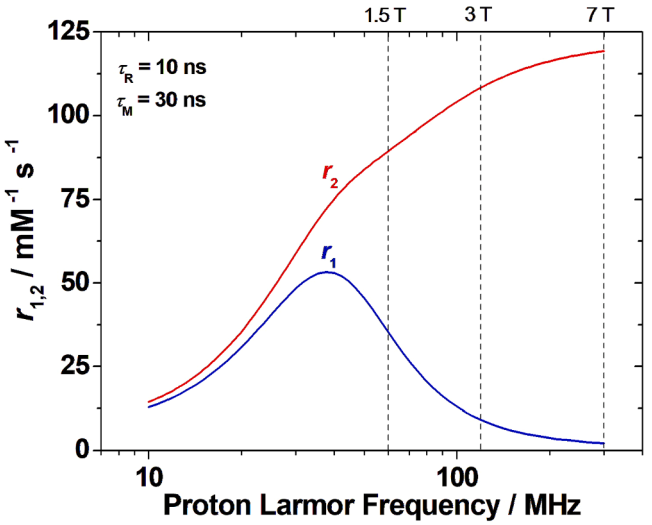

Fig. 3. Proton $1/T_1$ and $1/T_2$ NMRD profiles calculated for a macromolecular $q = 1$ Mn(II) system characterized by a rotational correlation time τ_R of 10 ns and by an exchange lifetime τ_M of 30 ns. Other parameters are: $\Delta^2 = 6.9 \times 10^{19}$ s^{-2}, $\tau_V = 28$ ps, $r = 2.83$ Å, $a = 3.6$ Å, $D = 2.3 \times 10^{-5}$ cm^2 s^{-1}.

encompassing physiological values is complemented by a high effective magnetic moment (characteristic of the d^5 high spin configuration), long electron relaxation times, and relatively fast inner-sphere water exchange rates (Table 1). It is worth noting that in Mn(II) complexes the r_H distance (Eq. (6)) is shorter (*ca.* 2.8 Å) compared to the value assumed by Gd(III) complexes (3.1 ± 0.1 Å). Due to the inverse sixth-power dependence of the dipolar contribution to the relaxation rate on the internuclear distance (Eq. (6)), the shorter separation between nuclear and electron spins helps partially offset the weaker magnetic moment of Mn(II). It is noteworthy that, despite these beneficial characteristics, only a single Mn(II)-based contrast agent has received clinical approval (mangafodipir trisodium, [Na_3[Mn(H_3DPDP)] (DPDP = dipyridoxyl diphosphate), TESLASCAN®) [39]. However, this Mn agent was withdrawn from the US market in 2003 and from the European market in 2012. It is hypothesized that the diminished charge and absence of crystal field stabilization energy in high-spin Mn(II) ions contribute to the challenges encountered in achieving the necessary high thermodynamic stability and kinetic inertness. However, the Mn-PyC3A (PyC3A = *N*-picolyl-*N*,*N*',*N*'-trans-1,2-cyclohexenediaminetriacetate) complex has passed the rigorous tests required for human studies and has successfully completed the Phase I clinical trial [40]. In addition, the Mn(II) complexes of 2,4-pyridyl-disubstituted bispidine ligands have been shown to be characterized not only by relaxivities comparable to those of the corresponding Gd(III) complexes but also by a very high kinetic inertness, unprecedented for Mn(II) chelates [41].

Mn(III). The high-spin $3d^4$ cation Mn(III) has $S = 2$. Its electron relaxation time assumes the value of *ca.* ≤ 10 ps for the hexaaqua complex and about 100 ps when chelated to porphyrins [42]. Given the inherent instability of the Mn(III) ion in aqueous media, coordination with appropriate multidentate ligands is requisite for its stabilization. In particular, porphyrins and phthalocyanines show a particularly high affinity for Mn(III) and the resulting complexes have received considerable attention. For example, a recent study showed that Mn(III)-$TPPS_3NH_2$ ($TPPS_3NH_2$ = 5-(4-aminophenyl)-10,15,20-(tri-4-sulfonatophenyl)porphyrin) is endowed with high thermodynamic stability and kinetic inertness against transmetalation by Zn^{2+} in neutral and acidic conditions, over two orders of magnitude higher than Gd(DOTA) [43]. In these complexes the Mn(III) ion has an octahedral coordination geometry, characterized by a plane comprised of four nitrogen atoms and the metal ion, with two axially positioned water molecules exhibiting weaker binding. These low-molecular-weight complexes have $q = 2$ and exhibit relaxivity values that are typically between 5–15 mM^{-1} s^{-1} in the frequency range 20–60 MHz and at 298 K. Even higher values can be obtained by restricting the molecular dynamics or by confinement in slowly tumbling systems. A recent review has fully and comprehensively described these compounds [44].

Mn(IV). Manganese has an accessible 4+ oxidation state, but there is no role for such a species in the preparation of metal complexes either discrete or anchored to macromolecular substrates. The investigated systems essentially concern MnO_2-based nanoparticles. The $3d^3$ electronic configuration of Mn(IV) leads to lower paramagnetism ($S = 3/2$, $\mu_{eff} = 3.87$ μ_B/atom; Table 1) due to the presence of only three unpaired electrons. Therefore, the contrast enhancement in MnO_2-based NPs is given by free Mn^{2+} release after dissolution of the particle prompted by endogenous stimuli. However, excess free Mn^{2+} ions in the body can cause severe toxicity issues, so it is important that they are stably and safely chelated by a polydentate organic ligand.

3. MRI contrast agents based on manganese nanosystems

3.1. Mn(II) systems

Mn(II)-based nanosystems can be divided in two main classes: 1) various types of inorganic nanoparticles (*i.e.* Mn(II) silicates, phosphates, etc.) and T_1-based Mn-oxide (MnO) and 2) Mn(II)-chelates or Mn(II)-clusters attached on or enclosed into soft and/or hard nanostructures. The topics of MnO NPs' preparation, characterization, MR-imaging, and toxicological properties have been covered by many reviews [27–31], in addition to delving into the chemistry and magnetic resonance capabilities of responsive MnO-based CAs [45]. Therefore, in this review the focus will be mainly on NPs functionalized with stable Mn(II)-chelates and on Mn(II)-containing inorganic NPs which have not yet been comprehensively examined [20,21].

It should be emphasized that certain Mn-containing NPs can release Mn^{2+} over extended periods, resulting in tissue accumulation and severe toxicity problems as demonstrated by various toxicological studies [46–49]. Thus, the use of polydentate polyaminocarboxylate ligands that form stable and inert complexes with Mn^{2+} is crucial to avoid any release of free Mn^{2+} in the body [23,50]. Different types of NPs, from silica to lipid-based systems, can be functionalized with these paramagnetic chelates to form nanosized MRI agents. For safe *in vivo* use, the Mn-chelate used in NP preparation must be thoroughly evaluated for thermodynamic stability and kinetic inertness [50]. Besides its stability, the Mn(II) complex is chosen depending on the functional groups present on the bifunctional chelating agent (BFCA) that should be complementary to those on the nanosystem [51]. The BFCA ligand is

Table 1
Key chemical and physical properties of metal ions utilized as MRI contrast agents.

Metal ion	Free ion ground state/ configuration	Spin-only magnetic moment (μ_B)	Ionic radius (Å)	Coordination number	Electronic relaxation times (s)	Mn-H_w distance (Å)
Mn(II)	$^6S_{5/2}$ (d^5)	5.9	0.83/0.90	6/7 (high spin)	10^{-10} - 10^{-8}	~2.8
Mn(III)	$^5D_0$ (d^4)	4.9	0.645	6 (high spin)	10^{-11} - 10^{-9}	2.6 - 2.8
Mn(IV)	$^4F_{3/2}$ (d^3)	3.9	0.39/0.53	4/6	n.a.	n.a.
Fe(III)	$^6S_{5/2}$ (d^5)	5.9	0.64	6–7	10^{-11} - 10^{-9}	2.6 - 2.7
Gd(III)	$^8S_{7/2}$ (f^7)	7.9	1.05/1.11	8/9	10^{-10} - 10^{-8}	~3.0

Table 2
Overview of fundamental characteristics of some Mn(II)-based NPs as MRI (and multimodal) CAs described in this section.[c.]

NPs components	Mn(II)-chelate	Relaxivity (mM^{-1} s^{-1}), 298 K[a], B_o (T) [b]	Imaging/ therapeutic modalities	Cell/Animal Model	Reference
a) Mn(II)-based micelles or liposomes					
Dextran-based	Mn(Pyridine-bis-pipecolinate)	r_1 = 13.3 (1.5 T)	MRA	Sprague-Dawley (SD) rats	[58]
Functionalized-texaphyrin	Mn-Texaphyrin	r_1 = 0.99; r_2 = 13.59 r_2/r_1 = 13.73 (7 T) [b]	T_2 MRI	VX-2 cancer cells on rabbits	[59]
MnL-micelles	Mn(HCDTA) Mn(DD-DO2A) Mn(DH-DO2A)	Mn(HCDTA) NPs r_1 = 18.4; Mn(DD-DO2A) NPs r_1 = 12.6 (0.5 T)	MRI	—	[60]
MnL-liposomes	Mn(HCDTA) Mn(DD-DO2A)	Mn(HCDTA) NPs r_1 = 17.3; Mn(DD-DO2A) NPs r_1 = 16.3 (0.5 T)	MRI	—	[63]
$P2MVP_{41}$-b-PEO_{205}	Mn(tris-dipicolinate)	r_1 = 10.8 (0.5 T)	MRI	* *in vivo model not indicated*	[64]
mPEG-p(MnL-a-HDMI)-mPEG	Mn-pyridine-bis-hydroxyproline	r_1 = 23.2 (0.5 T) r_1 = 9.7 (3 T)	MRA	Sprague-Dawley (SD) rats	[65]
MnL/DSPE-PEG2000 (1:19) micelles	MnL	r_1 = 24.9 (1.5 T) [b]	MRI	4T1 tumour bearing BALB/c mice	[66]
Mn(C18-PhDTA)/ PEG (1:10) micelles	Mn(C18-PhDTA	r_1 = 13.3 r_2 = 23.8; r_2/r_1 = 1.8 (1.5 T) [b]	T_1 MRI	4T1 tumour bearing BALB/c mice	[67]
b) Mn(II) chelates on dendrimeric systems					
Lysine G3 Dendrimers	MnDOTAMA MnNOTA-MA	r_1 = 3.13; r_2 = 8.74 r_2/r_1 = 2.79 (3 T) r_1 = 3.80; r_2 = 24.5 r_2/r_1 = 6.45 (3 T)	T_1-T_2 MRI	MDA-MB-231 human breast carcinoma	[71]
CLT1 peptide on MnL G3 dendrimer	MnDOTAMA	r_1 = 3.13; r_2 = 8.74 r_2/r_1 = 2.79 (3 T)	T_1-T_2 MRI	MDA-MB-231 human breast carcinoma	[72]
MnDOTA-PAMAM- hyaluronate-FITC-Au NPs	MnDOTAMA	r_1 = 5.4 (0.5 T)	CT/MRI	orthotopic HCCLM3 tumour model	[73]
MnDOTA core-dendrimer	MnDOTA-amides (mixed)	r_1 = 3.1 (1.5 T)	MRI	Healthy mice	[74]
c) Polysaccharides NPs functionalized with Mn(II) chelates					
MnL on cellulose NCs	Mn-polydopamine	r_1 = 38.0 (3 T) for $(Mn\text{-}PDA)_4$@CNCs	MRI/ PTT	—	[75]
MnL on cellulose NCs	MnDTPA-amide	r_1 = 57 (3 T) for MnDTPA@DCNC-8	MRI/PTT	RAW 264.7 and HUVEC cell lines	[76]
Chitosan-(Mn-DTPA)n	MnDTPA-amide	r_1 = 15.42 (3 T)	MRI	Sprague-Dawley (SD) rats	[77]
Alginate-PDA Ca/Mn NGs	Mn-alginate-PDA	r_1 = 12.54; r_2 = 141.38 r_2/r_1 = 11.27(7 T) [b]	T_2 MRI	BALB/c mice	[78]
Cross-linked chitosan NGs	Mn-*t*-CDTA-amide	r_1 = 30.5 (0.5 T)	MRI	Breast tumours	[79]
d) Mn(II) chelates anchored on silica, carbon or iron oxide NPs					
MSNs-MnDTPA	MnDTPA-amide	r_1 =7.18 (1 T) [b]	MRI	C57BL/6j mice	[81]
SNPs-MnCDTA	MnCDTA	r_1 = 18.6 (0.5 T)	MRI	C57BL/6j mice	[82]
Porous silica NPs	Mn(pyridine-bis-picolinate)	r_1 = 8.46; r_2 = 33.15 r_2/r_1 = 3.92 (1.41 T)	T_1-T_2 MRI	*In vitro* HeLa cells	[83]
Nanodiamonds-MnEDTA (or MnDOTA)	MnEDTA-monoamide or MnDOTA	MnEDTA: r_1 = 8.1; r_2 = 72.7; r_2/r_1 = 8.98 (7 T) MnDOTA: r_1 = 9.4; r_2 = 211.7; r_2/r_1 = 22.5 (7 T)	T_1/T_2 MRI	Murine hepatic tumours	[84]
Mn@CC carbon NPs	Mn-gluconate and aspartic acid	r_1 = 42.9 (1.5 T)[b]	MRI and bioluminescence	orthotopic brain tumours	[85]
Mn@CD carbon NPs	Mn-gluconate and aspartic acid	r_1 = 10.8 (3.0 T)[b]	CE-MRI	Acute Kidney Injury	[86]
SPIO NPs core-shell with Mn (Dopa-EDTA)	Mn(Dopa-EDTA) (d = 4 and 7 nm)	(d = 4 nm): r_1 = 8.4: r_2 = 14.7; r_2/r_1 = 7.8 (0.5 T) r_1 = 5.4; r_2 = 28.4; r_2/r_1 = 5.26 (3.0 T) (d = 7 nm): r_1 = 10.0; r_2 = 150.0; r_2/r_1 = 15.0(3.0 T)	MRA and T_1/T_2 MRI	Sprague-Dawley (SD) rats and BALB/c mice	[87]
e) Other types of Mn(II) chelate-containing nanoassemblies					
Mn-DTPA cystamine copolymer Mn-EDTA cystamine copolymer	Mn-DTPA Mn-EDTA	r_1 = 4.74 r_2 = 10.38 r_2/r_1 = 2.19 (3 T) [b] r_1 =6.41; r_2 = 9.72 r_2/r_1 = 1.52 (3 T) [b]	T_1 MRI	MDA-MB-231 breast cancer mice	[88]
P(MnL-PEG200)-3 copolymer	MnL	r_1 = 23.9 (1.5 T) [b]	MRI	H22 liver tumour BALB/c mice	[89]
MnL-BODIPY-BSA-PEG-FA	Mn(bis-2-pyridil methyl) amine	r_1 = 40 (3 T) [b]	MRI/PTT	HEPG2 tumour in IPC mice	[90]
$NaScF_4$-PAA-Mn-porphyrin-HSA-RGD	Mn-porphyrin	r_1 = 21.5 (7 T) [b]	PDT/MRI/OI	Glioma tumour U87 cells	[91]
Mn^{2+} on surface of Ti carbide (Ti_3C_2) nanosheet	Mn-surface of Ti_3C_2	r_1 = 1.05 (3 T) [b]	MRI/PTT/CDT	4T1 tumour-bearing mice	[92]
Ag-In-Ga-Zn-S QDs/ Mn-stearate	Mn-stearate	r_1 = 0.28; r_2 = 0.75; r_2/r_1 = 2.68 (1.41 T) [b] r_1 = 0.15; r_2 = 0.57; r_2/r_1 = 3.8 (2.34 T) [b]	T_1/T_2 MRI/OI	—-	[93]

(*continued on next page*)

Table 2 (*continued*)

NPs components	Mn(II)-chelate	Relaxivity (mM^{-1} s^{-1}), 298 K[a], B_o (T) [b]	Imaging/ therapeutic modalities	Cell/Animal Model	Reference
f) Mn-containing metal organic frameworks (MOFs)					
$Mn(BDC)(H_2O)_2$ and $Mn_3(BTC)_2(H_2O)_6$ MOFs	Terephthalic (BDC) and trimesic (BTC) acid bridging ligands	r_1= 5.5; r_2 = 80.0; r_2/r_1 =14.5 (BDC) (3.0 T) r_1= 7.8; r_2 = 70.8; r_2/r_1 = 9.1(BTC) (3.0 T)	T_2 MRI/OI	HT-29 cells incubated with c(RGDfK)-targeted and nontargeted MOFs	[97]
$[Mn_2(Cmdcp)_2(H_2O)_2$ MOFs	N-(4-carboxybenzyl)-(3,5-dicarboxyl) pyridinium bromide	r_1 = 17.5 (0.5 T, 303 K)	MRA	Healthy mice	[98]
PEG-Mn-MOF-74	2,5-dihydroxy terephthalic acid	r_1 = 13.5; r_2 = 46.8; r_2/r_1 = 0.29 (1T)	T_1 MRI	BALB/c nude mice	[99]
MTX-Mn@PEG	Mn-methotrexate (Methotrexate) and DSPE-PEG	r_1 = 7.8 (0.5 T)	MRI/ChT	BALB/c nude mice bearing HeLa tumours	[100]
DOX@Mn(II)-PBC MOF	Mn(II)-PBC	r_1 = 3.73 (0.5 T)	MRI/ChT	*In vitro* HeLa cells	[101]
GMTF NSs	Mn(II)-TCPP-Gd^{3+}-F-127	r_1 =4.40 (3T)	MRI/CDT/SDT	CT26 tumor-bearing mice	[103]
g) Paramagnetic Mn(II) clusters and other inorganic NPs					
$Mn_3(O_2CCH_3)_6(Bpy)_2$ cluster Mn_3Bpy-Pam nanobeads	Bipyridine and acetate	r_1 = 6.9; r_2 = 124.7; r_2/r_1 = 18.07(Cluster) (9.4T) r_1 = 54.4; r_2 = 144; r_2/r_1 = 2.65 (NPs) (9.4 T)	T_1/T_2 MRI	healthy mice and with xenograft tumours	[104]
$K_{4-2x}Mn_xRe_6Se_8$ NPs	hexarhenium clusters	r_1 = 8.9; r_2 = 10.9; r_2/r_1 = 1.22 (0.47 T, 310 K)	T_1/T_2 MRI	——-	[105]
HA-$MnWO_4$ NPs	Hyaluronic acid and $MnWO_4$	r_1 = 0.78; r_2 = 6.76; r_2/r_1 = 8.67 (1.2 T)[b]	T_1/T_2 MRI/CT	Kunming or MDA-MB-231 tumour-bearing mice	[106]
PEG-coated $KMnF_3$ NPs	$KMnF_3$	r_1 = 23.15; r_2 = 74.1; r_2/r_1 = 3.2 (3.0 T)	T_1/T_2 MRI	Kunming naked mice	[109]

[a] Unless otherwise stated
[b] Temperature not indicated
[c] r_2 not shown when not calculated.

characterized by its strong affinity for the Mn^{2+} ion and the presence of a functional group that facilitates stable covalent conjugation to a vector via a variety of chemical linkages. A detailed discussion of polydentate ligands employed in Mn(II) complexation, as well as the relaxometric and stability properties of the resulting Mn(II)-chelates, is not included here, as these topics have been addressed in recent review articles [23, 51].

Mn(II)-based NPs containing Mn(II)-chelates and used for MRI, multimodal and theranostic applications are the main focus of this section. Six main categories of Mn(II)-based NPs can be identified in the literature: 1) lipid-based NPs formed from self-assembling amphiphilic paramagnetic units; 2) nanoglobular dendrimeric systems containing Mn(II)-chelates; 3) polysaccharide NPs or nanogels (NGs) functionalized with Mn(II)-complexes; 4) silica, carbon or iron oxide NPs with Mn(II)-chelates bound at the surface or held in porous structures; and 5) more complicated nanoassemblies, including polymeric systems, containing different types of Mn(II)-chelates in interaction with other parts of the nanosystem. This section will be concluded with an overview of the different types of Mn(II)-based NPs including Mn-containing metal organic frameworks (MOFs), Mn(II)-containing clusters, Mn(II) inorganic NPs employed as T_1 MRI CAs. The main properties as MRI or multimodal CAs of the examples reported are summarized in Table 2.

3.1.1. *Mn(II)-based micelles or liposomes*

The use of paramagnetic complexes linked to a hydrophobic moiety that allows the spontaneous self-aggregation into micelles or liposomes in aqueous solution have been largely employed as a strategy for developing high-relaxivity Gd-based systems [52–54]. Other types of self-assembled nanosystems have also been proposed, which contain block-copolymers, such as polymersomes [55], or dendritic molecules such as dendrimersomes [56]. In general, whereas the defining feature of micelles is their core-shell structure, with diameters typically between 5 and 50 nm, liposomes are nanovesicles made up by a phospholipid bilayer and an aqueous core with diameter in the range 50 to 1000 nm. The structural properties of these lipidic nanosystems are amenable to control, thereby enabling the modulation of size, surface charge, and membrane composition, as well as the conjugation of targeting vectors for applications in molecular imaging [57].

In the case of Mn-based micellar systems, there are fewer examples than those reported for Gd-systems, although the results are somehow intriguing. Ai et al. reported the first example of Mn-based micelles, which were built by conjugating a dextran amphiphilic polymer to a pyridine-based constrained Mn(II)-complex through an azide-alkyne 1,3-dipolar cycloaddition reaction (Fig. 4) [58]. At 1.5 T and 298 K, the ~85 nm lipidic aggregates showed a relaxivity of 13.3 mM^{-1} s^{-1}, almost triple that of the mononuclear complex. A 3T magnetic resonance angiography (MRA) investigation in rats demonstrated large signal enhancement within the vasculature, affording a 50-minute imaging window with the use of a rather low dose of 0.1 Mn mmol/kg body weight.

A second notable example was reported by Zheng et al. using Mn-texaphyrin-phospholipidic nanoparticles to visualize by MRI the lymphatic drainage from the tumour region to neighbouring lymph nodes (Fig. 5) [59]. In this example, the pentaaza Schiff base macrocycle of texaphyrins bears a phospholipidic moiety and can self-assemble in a nanostructure after Mn-complexation and in the presence of cholesterol and a pegylated phospholipid as coadjuvant. The Mn-nanotexaphyrins exhibit a size of 100 nm and a r_1 at 7 T of 0.81 $mM^{-1}s^{-1}$. The relaxivity value is even lower than that of the Mn-texaphyrin-phospholipid complex (0.99 $mM^{-1}s^{-1}$) probably due to the formation of a nanovesicle with an aqueous core: the Mn-complexes are distributed between the inner and the outer compartments and generate two different contributions depending on the water permeability through the lipid bilayer. We can presume that, in this example, the permeability is low and the Mn-complexes pointing inwards do not contribute to the overall relaxivity. It should also be noted that paramagnetic nanosized systems exhibit a T_1 relaxivity that peaks at magnetic fields around 0.4 to 1 Tesla, reaching its maximum values. At B_0 values $\geq$ 3 T, it is established that nanosized systems are not efficient as T_1 agents [15]. Nevertheless, Mn-nanotexaphyrins were studied *in vitro* to determine their stability in serum and *in vivo* on rabbits to show a strong contrast enhancement in the lymph nodes after subcutaneous injection in the tumour area [59].

Furthermore, amphiphilic Mn(II) chelates based on EDTA (ethylenediaminetetraacetate) and 1,4-DO2A (1,4,7,10-tetraazacyclododecane-1,4-diacetate) bearing one or two carbon chains on the ligand structure were shown to form micelles in water or by combining them with specific phospholipids (Fig. 6A) [60] $[Mn(EDTA)]^{2-}$ is a mono-aquo complex with a sufficient thermodynamic stability ($\log K_{ML}$ = 12.95) and a good relaxivity (3.3 mM^{-1} s^{-1}), although its kinetic inertness is insufficient for *in vivo* applications ($t_{1/2}$ at pH 7.4 = 4.56 min). On the other hand, Mn(1,4-DO2A) is a neutral complex that exists in equilibrium between two forms: a monohydrate (q = 1) hepta-coordinated species and a hexacoordinated species lacking a bound water molecule. The approximate ratio of these species is 87:13 [61]. Its relaxivity is lower than for $[Mn(EDTA)]^{2-}$ (2.1 mM^{-1} s^{-1}), but it largely exceeds in terms of stability and kinetic inertness in physiological conditions ($\log K_{MnL}$ = 15.68; $t_{1/2}$ at pH 7.4 = 57 h) [62]. Good relaxivity values and sizes in the range 13–84 nm were displayed by the micelles based on amphiphilic MnEDTA-like or Mn(1,4-DO2A)-like complexes carrying one (or two) C_{12} or C_{16} aliphatic chain(s). In particular, the chelates with two aliphatic chains show a partially blocked local rotation once they are incorporated into the lipidic nanoparticle resulting in high relaxivity values (Fig. 6B: r_1 = 18.4 $mM^{-1}s^{-1}$ for $[Mn(HCDTA)]^{2-}$ and 12.6 mM^{-1} s^{-1} for MnDD-DO2A, at 298 K, 0.5 T) (HCDTA = 13, 14-hexacosanediamine-*N,N,N′,N′*-tetraacetic acid, DD-DO2A = 1,4,7, 10-tetraazacyclododecane-7,10-didodecyl-1,4-diacetate) [60]. The same EDTA and DO2A-like Mn-chelates were also embedded in the phospholipid bilayer of liposomes, and the study revealed that the formation of liposomes (~110 nm size), non-vesicular bicelles (~14 nm size), or a combination of both, as well as the size and morphology of the nanoaggregates, are influenced by the length and position of the aliphatic chains, as shown in Fig. 6C for the diamagnetic Zn^{2+} analogues [63]. The relaxivities of the nanosystems were similar to those found for the previously reported micelles, *i.e.*: with 20 % of Mn-chelate in the formulation DPPC 75 % and DSPE-PEG2000 5 % (DPPC = dipalmitoylphosphatidylcholine, DSPE =1,2-distearoyl-sn-glycero-3-phosphoethanolamine) the relaxivity values at 298 K and 0.5 T were 17.3 $mM^{-1}s^{-1}$ for $[Mn(HCDTA)]^{2-}$ (bicelles) and 16.3 mM^{-1} s^{-1} for Mn (DD-DO2A) (liposomes). No *in vivo* studies have been reported on these lipidic nanoparticles yet. However, they hold great promise as MRI agents and as theranostic platforms for targeted drug delivery and controlled release to pathological sites [63].

Another example of micellar aggregates containing Mn-chelates was reported by Cohen Stuart et al. and consists of the assembly of three components (a polycationic diblock co-polymer, Mn^{2+} ions and tri- or dimeric ligands) held together mainly by electrostatic interactions (Fig. 7) [64]. These nanoparticles have the peculiarity of being stable at high concentrations of salts (*i.e.* buffers) owing to the presence of tris-dipicolinic acid (DPA) ligands that stabilise the nanoconstructs. The micelles containing the tris-DPA ligand exhibit a r_1 of 10.8 mM^{-1} s^{-1} (0.47 T, 298 K). They were also tested *in vivo* at 0.5 T and at a dose of 30 μmol kg^{-1} showing a good signal enhancement at 2 h post injection.

Recently, a two-step polycondensation reaction involving the chelator pyridine-bis-hydroxyproline, hexamethylene diisocyanate (HMDI), and polyethylene glycol of varying molecular weights (mPEG-P(L-a-HMDI)-mPEG) was developed to obtain a series of polyurethane-based amphiphilic polymers [65]. The resulting Mn(II)-chelates (mPEG-P(MnL-a-HMDI)-mPEG) aggregate in 48 nm size micelles having a low critical micelle concentration (CMC) of 4.7 mg L^{-1}, and high relaxivity (in case of the mPEG2k system, r_1 = 23.2, 14.4 and 9.7 mM^{-1} s^{-1} at 0.5 T, 1.5 T and 3.0 T, respectively). This aggregated system was selected to carry out an *in vivo* MRA study, and demonstrated outstanding performance in T_1 contrast enhancement, showcasing good vascular imaging and effective stenosis detection, all without Mn(II) brain accumulation. The same Mn-chelate functionalized with two C12 aliphatic pendant arms was used in the preparation of mixed micelles with DSPE-PEG2000 phospholipid. Different ratios of the Mn-chelate *versus* DSPE-PEG2000 formed micelles with different sizes and relaxivities, with lower manganese doping density exhibiting increased q and enhanced relaxivity (r_1 of the micelle with DSPE-PEG2000/MnL mass ratio: 19:1 is 24.9 Mn mM^{-1} s^{-1} at 1.5 T). *In vivo* sentinel lymph node (SLN) imaging was performed showing that DSPE-PEG/MnL mixed micelles could differentiate metastatic SLN from inflammatory lymph nodes [66].

Finally, aiming to obtain MR images of SLNs, Chen et al. used a similar approach to construct hybrid micelles by replacing the Mn chelate with an amphiphilic Mn(PhDTA) (PhDTA = *o*-phenylenediamine-*N,N,N′,N′*-tetraacetic acid) complex and the DSPE-PEG2000 with a C18-PEG polymer. In this case the maximum relaxivity at 1.5 T was reached with the 1:10 MnL-PEG-C18 mass ratio, being 13 mM^{-1} s^{-1}. The injection of these lipidic NPs at 125 μg Mn/Kg allowed to obtain bright images of lymph nodes at 2 h *p.i.* without signal intensity alteration in non-lymphoid regions [67].

3.1.2. Mn(II) chelates on dendrimeric systems

The use of dendrimers, in particular polyamidoamine (PAMAM) dendrimers, for the conjugation of a growing number of Gd-chelates at the outer edge and for increasing the relaxivity has been largely investigated since 1994 [68–70]. In fact, dendrimeric scaffolds offer several favourable properties such as well-defined size and shape, low polydispersity, safety and ease of chemical functionalization. In the case of Mn(II) systems, the first examples were reported by Tan et al. who functionalized a generation 3 (G3) lysine dendrimer with silsesquioxane core functionalized with MnDOTA-monoamide (DOTA = 1,4,7,10-tetraazacyclododecane-1,4,7,10-tetraacetate) chelates and a peptide that binds the fibrin-fibronectin complexes or oncofetal fibronectin in tumour stroma (CLT1) (Fig. 8) [71]]. The nanoglobular agent had a well-defined size of 5.2 nm comprising two peptide units and 42 MnDOTAMA (DOTAMA = DOTA-monoamide) chelates on the surface of the dendrimer, with r_1 and r_2 of 3.13 and 8.74 mM^{-1} s^{-1} per Mn(II) chelate at 3 T and 298 K, respectively. The low T_1 relaxivity is due to the lack of coordinated water molecule in the MnDOTAMA chelates (q = 0). Nevertheless, the targeted nanoglobular agent could be readily excreted via renal filtration and specifically bound to tumour tissue in tumour bearing mice with low nonspecific accumulation in the liver, showing enhanced tumour contrast in comparison to a nontargeted control at a 0.03 mmol-Mn/kg dose [71]. The same group functionalized the silsesquioxane-lysine G2-G4 dendrimeric systems with MnDOTAMA and MnNODAGA (NODAGA = 1,4,7-triazacyclononane-*N,N,N*-1,4-diacetate-7-glutarate) chelates to investigate size and chelate effect on the Mn-based nanoglobular MRI CAs (Fig. 8) [72]. The relaxivities decreased with the increasing generation of the dendrimers resulting in higher r_1 values for the G3 nanoglobular MnNODAGA conjugate (r_1 = 3.8 mM^{-1} s^{-1}) than the corresponding MnDOTAMA conjugate (r_1 = 2.4–3.3 mM^{-1} s^{-1}). Again, although the *per Mn* relaxivity is low since the Mn-chelates are q = 0, these nanoprobes were successful at a low dose for the contrast enhancement in cancer imaging within a mouse tumour model and were readily excreted via renal filtration [72].

In 2016 Wang et al. modified a G5 PAMAM dendrimer with MnDOTA, fluorescein isothiocyanate and hyaluronic acid (HA) to obtain multifunctional NPs able to target CD44 receptor-expressing cancer cells for dual-mode MRI/CT imaging [73]. Gold nanoparticles (AuNPs) were also entrapped within the dendrimeric structure to achieve NPs with a hydrodynamic diameter of 188 nm, good water dispersibility, stability under different conditions, and cytocompatibility. The final NPs displayed a high X-ray attenuation intensity thanks to the AuNPs and r_1 of 5.4 mM^{-1} s^{-1} at 0.5 T and 298 K. This nanosystem was employed to image human hepatocellular carcinoma (HCC) cells *in vitro* and in an orthotopically transplanted HCC tumour model through the CD44 receptor-mediated endocytosis pathway. The tumor tissue exhibited higher CT density and MR signal intensity values compared to the normal liver tissue [73].

Finally, an unusual dendrimeric/multinuclear system obtained by conjugating several DOTA units together in a globular fashion (up to

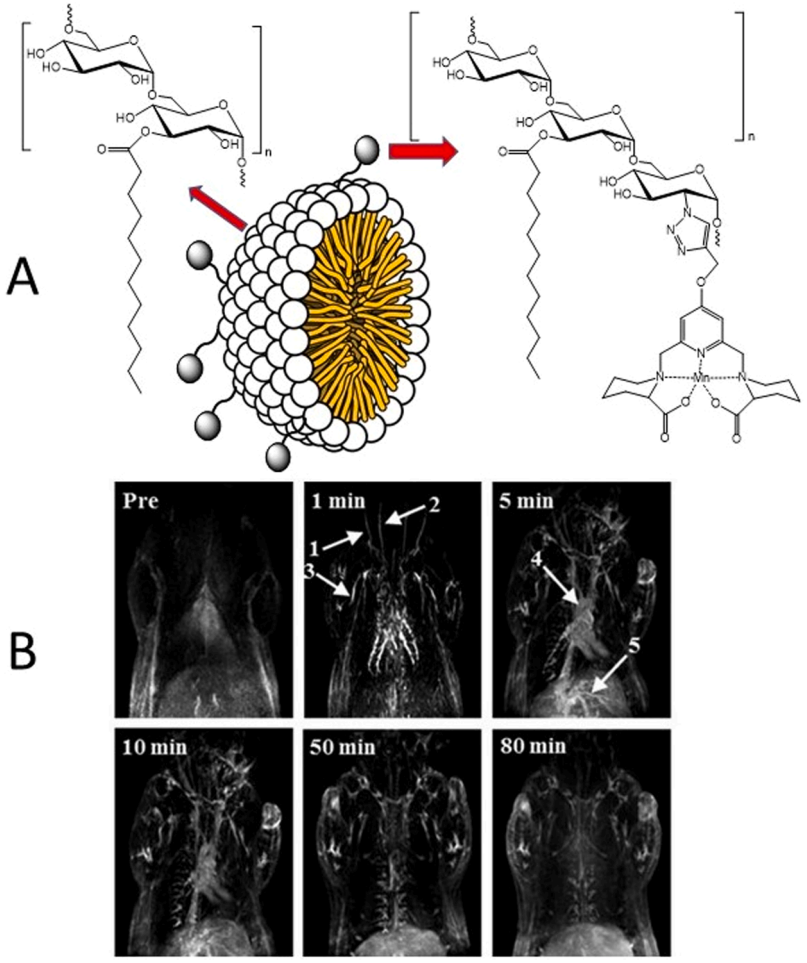

Fig. 4. A. Mn-complexes conjugated to dextran-based micelles; B. 3.0 T clinical Magnetic Resonance Angiographic (MRA) of SD rats with contrast enhancement, focusing on jugular vein (1), carotid artery (2), subclavian vein (3), aortic arch (4), and hepatic portal vein (5). Adapted from ref 58.

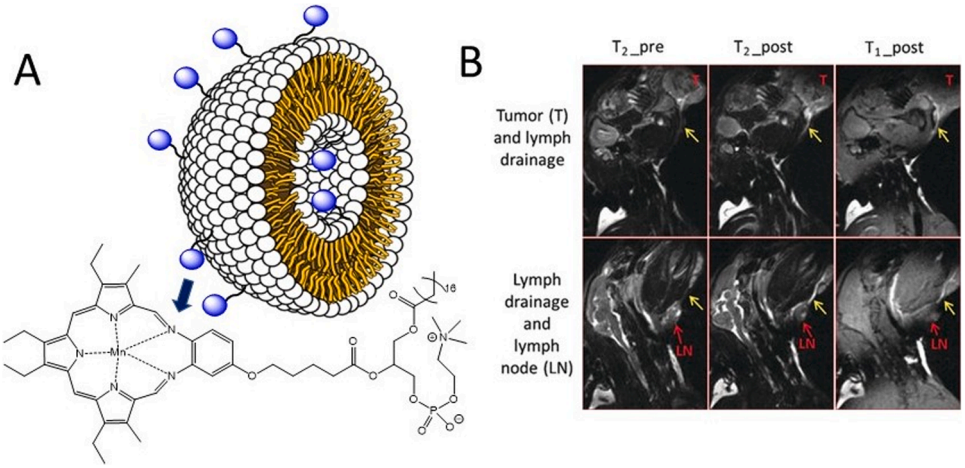

Fig. 5. A. Chemical structure of the Mn-texaphyrin-phospholipid self-assembled in Mn-nanotexaphyrins; B. T_1- and T_2-weighted images of the tumour region and lymph node of a head and neck VX-2 rabbit tumour on a 7 T preclinical MRI system pre- and 2 h post-injection. (Adapted from ref 59).

generation 3) was used to build a Mn(II) based nanosystem after complexation with Mn^{2+} (Fig. 9) [74]. The G3 system showed a hydrodynamic diameter of 6.4 nm, an enhanced kinetic inertness of the Mn-chelates, probably due to spatial confinement and electrostatic repulsion within the dendrimeric core, and a relaxivity of 3.1 mM^{-1} s^{-1} at 1.5 T. An *in vivo* dynamic MRI study further demonstrated that Mn(II) united-DOTA complexes could offer greater and enduring contrast enhancement compared to both MnDOTA and Magnevist, although in case of the Mn-G3 system a large accumulation in the liver, spleen, and kidney was observed, probably due to the larger hydrodynamic diameter (6.7 nm) than the renal filtration threshold (5.5 nm).

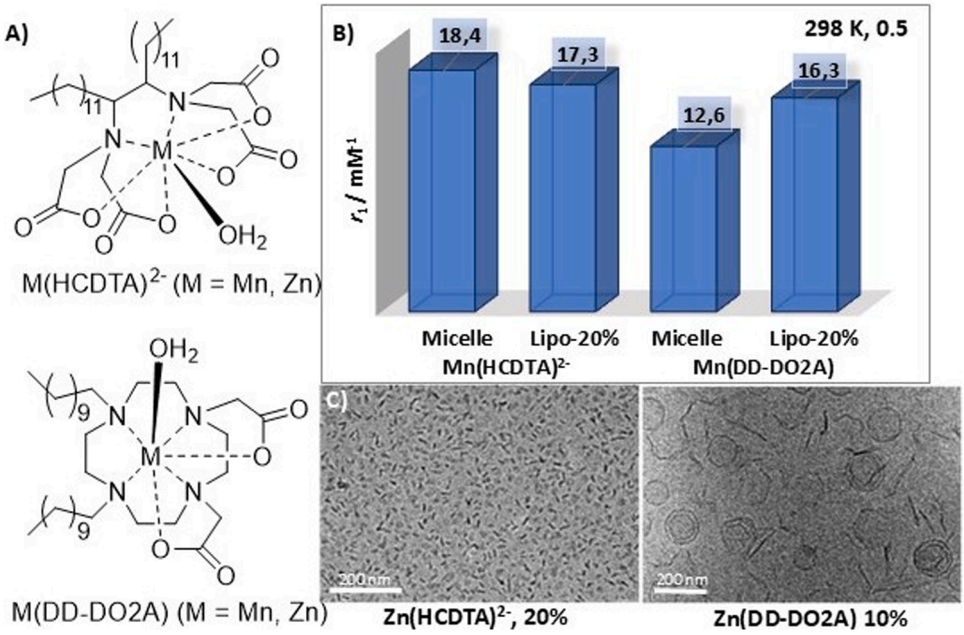

Fig. 6. A) EDTA- or 1,4-DO2A-based Mn(II) or Zn(II) amphiphilic chelates; B) Relaxivity data for micellar and vesicular aggregates containing Mn^{2+}-amphiphilic complexes; C) Cryo-TEM images of nanoaggregates incorporating 20 % $[Zn(HCDTA)]^{2-}$ and 10 % Zn(DD-DO2A) [60,63].

3.1.3. Polysaccharides NPs functionalized with Mn(II) chelates

Ligand modified polysaccharides or cellulose nanocrystals (CNCs) were also used for the coordination of Mn(II) ions to prepare biocompatible and biodegradable Mn-based nanosystems [75–79]. Different methods have been reported conjugating Mn(II)-chelating units like diethylenetriamine pentaacetic acid (DTPA) or dopamine to alginate, carboxymethyl chitosan and CNCs to form polymeric or rod-shaped NPs. Thus, Shen et al. conjugated Mn-dopamine complexes to CNCs at different ratios to form NPs with Mn^{2+} incorporated into polydopamine (PDA) coated CNCs [$(Mn\text{-}PDA)_{1-6}$@CNCs] for MRI/photothermal (PTT) theranostic applications (Fig. 10A) [75]. The authors stated that the highly cross-linked anisotropic CNC surface by PDA coating enabled *in vivo* application by inhibiting the aggregation of Mn(II)-NPs. These NPs had a rod-shaped architecture (size ~150–200×10 nm) and r_1 = 38 $mM^{-1}s^{-1}$ (3 T, 298 K) for $(Mn\text{-}PDA)_4$@CNCs. Conversely, increasing the (Mn-PDA)/CNCs ratio enhanced the photothermal conversion efficiency (η) of PDA from 17.7 % to 44.4 %, rendering these NPs suited for cancer therapy and therefore, a theranostic nanosystem. The same group reported the synthesis of MnDTPA@CNSs NPs by conjugating various amounts of DTPA-bis-anhydride to CNCs. The relaxivity of these NPs increased with the number of MnDTPA-chelates conjugated to the surface of the CNCs (Fig. 10B) [76]. The relaxivity at 25 °C and 3.0 T was 57 $mM^{-1}\ s^{-1}$ for Mn^{2+}@DCNC-8, that is a really high value for a $q = 0$ Mn (II) complex anchored on NPs' surface. Furthermore, the cytotoxicity assay on RAW 264.7 and human umbilical vein endothelial cell (HUVEC) lines showed that these nanoprobes are non-toxic with a cell viability higher than 80 %.

Another MnDTPA-based carboxymethyl chitosan (CMCS) macromolecular CA was reported displaying great water solubility, positive biocompatibility and controlled biodegradability [77]. About 14.5 % of MnDTPA chelates were grafted onto CMCS-$(Mn\text{-}DTPA)_n$ and a relaxivity of 15.42 $mM^{-1}s^{-1}$ (at 3 T) and suitable cellular and blood biocompatibility were measured. Moreover, the administration of CMCS-$(Mn\text{-}DTPA)_n$ resulted in a strong image contrast enhancement in liver and kidneys even at a dose as low as 0.03 mM Mn/kg b.w. Additionally, the compound was naturally excreted within 10 days without causing discernible pathological changes in the rat liver.

Furthermore, Addisu et al., inspired by adhesive proteins in mussels, prepared and investigated nanogels (NGs) composed by Ca(II)/Mn(II) complexed by alginate−polydopamine or dopamine conjugated to alginate [AlgPDA/DA(Ca/Mn)] [78]. The surface functionalization with polyethylene glycol (PEG) molecules of these NPs also allowed to increase their blood circulation half-life. The surface charge of these nanogels was negative and the size was 66 nm for AlgPDA(Ca(Mn) and 135 nm for AlgDA(Ca/Mn). They showed a relaxivity of 12.54 $mM^{-1}s^{-1}$ for AlgPDA(Ca/Mn) and 10.13 $mM^{-1}s^{-1}$ for AlgDA(Ca/Mn) NGs (at 7 T). However, it must be noted that an r_2/r_1 ratio of 13.2 and 14.0 was measured for the two nanogels preventing their full effectiveness as T_1 MRI agents.

Another type of nanogel (NG) based on chitosan crosslinked by Mn-*trans*-CDTA-amide (CDTA = 1,2-diaminocyclohexane-*N,N,N',N'*-tetraacetic acid) complexes was recently reported [79]. It should be noted that $MnCDTA^{2-}$ and derivatives are stable Mn-complexes (log K_{MnCDTA} = 14.32; $t_{1/2}$ at pH 7.4 = 12 h) and they present one coordinated water molecule that guarantees high relaxivity values at clinical fields ($q = 1$, $r_{1(MnCDTA)} = 3.6\ mM^{-1}\ s^{-1}$ at 0.5 T and 298 K). In this example (Fig. 11), the stable and inert MnCDTA-complexes are covalently linked to the NGs and act both as paramagnetic and crosslinking agents allowing to achieve high relaxivities and high stability of the nanosystem. In fact, the combination of a restrained Mn-complex mobility and a fast metal-bound water exchange allowed to reach relaxivity values of 30.5 $mM^{-1}\ s^{-1}$ for these NGs (at 0.5 T, 298 K), surpassing by sevenfold those of typical $q = 1$ Mn(II) chelates. Moreover, the NGs formulation exhibited excellent stability over time in both aqueous solution and in biological environment, excluding concerns regarding particle aggregation or the release of free metal ion. The authors investigated through a full ^1H and ^{17}O NMR relaxometric study not only the Mn-NGs, but also model Mn-CDTA-mono and bis-glucosamide chelates to support that the Mn(II) complex has one coordinated water molecule in fast exchange with the bulk. Mn-NGs were then tested in mice bearing a subcutaneous breast cancer, showing good extravasation and accumulation in the tumour with a *ca.* 20 % signal enhancement at 1 T at 24 h post-injection, as also confirmed by Mn quantification by ICP-MS (inductively coupled plasma-mass spectrometry) analysis of the explanted organs [79].

3.1.4. Mn(II) chelates anchored on silica, carbon or iron oxide NPs

In the last 15 years, mesoporous or amorphous silica nanoparticles have been largely employed as scaffold for the conjugation of

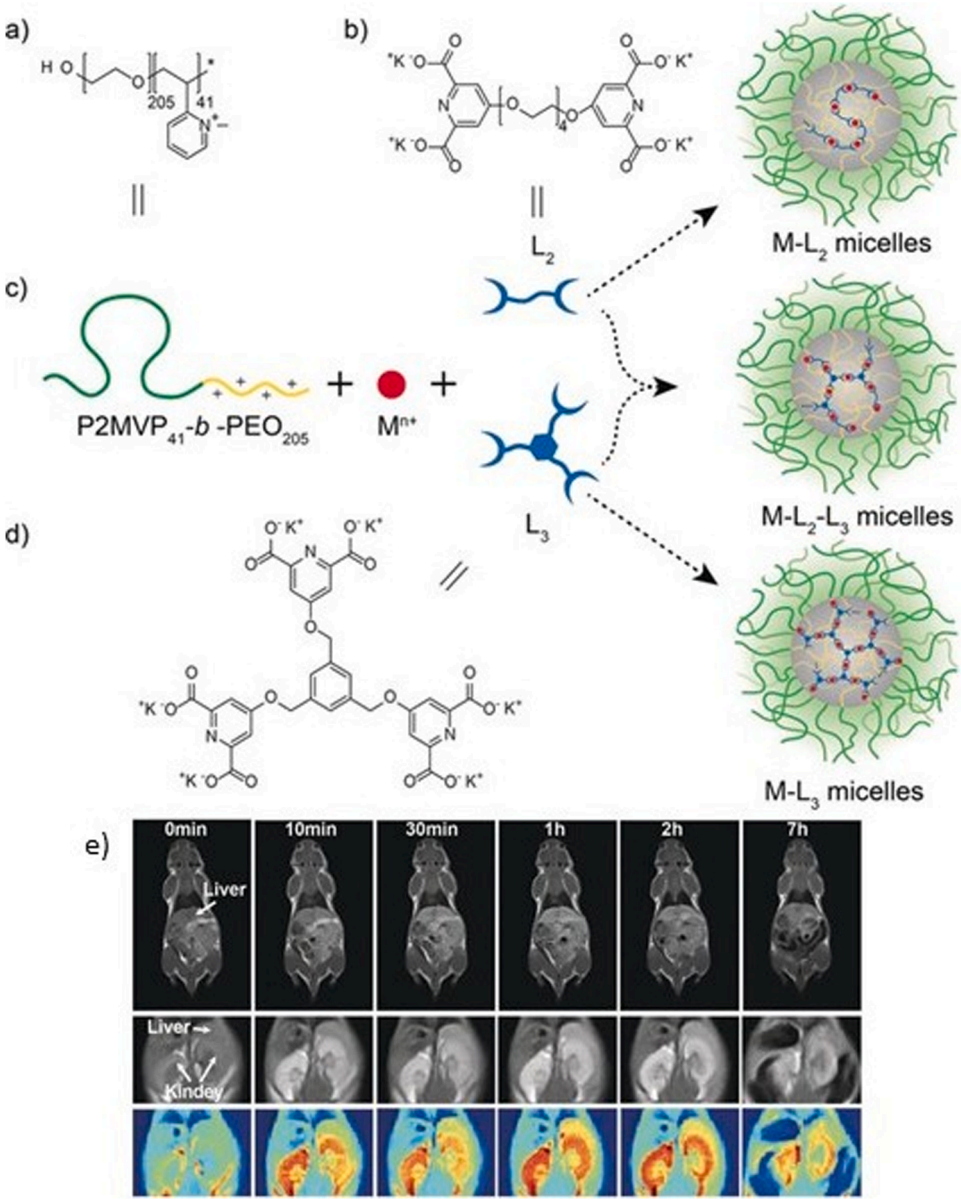

Fig. 7. a) Structure of P2MVP$_{41}$-*b*-PEO$_{205}$. b)Structure of bis-ligand L_2. c)Depiction of the formation of M-L_2-L_3 micelles. d)Chemical structure of tris-ligand L_3. e) *Invivo* T_1-weighted and colour mapped MR images (0.47 T) of a mouse at different time post-injection of micelles based on Mn-L_3 at a dose of 30μmol kg^{-1}. (Adapted from ref 64).

paramagnetic chelates, in particular for Gd-based probes [80], but only few examples relative to Mn-chelates are reported. Varga et al. proposed the first nanoprobe by surface functionalization of amino-modified silica NPs with DTPA chelators for Mn(II) complexation (Fig. 12A) [81]. Although [Mn(DTPA)]$^{3-}$ provides only outer sphere relaxation contribution ($q = 0$), the nanoprobes exhibited a relaxivity value of *ca.* 7.2 mM^{-1}s^{-1} at 1 T, and showed considerable liver-specific T_1-weighted MRI contrast after injection in mice.

Analogous amino-functionalized silica NPs have been recently conjugated to a bisamide derivative of MnCDTA (Fig. 12B) [82]. The final NPs have a size of about 90 nm, spherical shape, and relaxivity of 18.6 mM^{-1} s^{-1} (0.5 T, 298 K), about 250 % higher than the free chelate. Finally, preliminary *in vivo* investigations on healthy mice at 1 T showcased the efficacy of the MnCDTA-modified silica NPs as T_{1w}−MRI probes, leading to a signal enhancement in the liver of approximately 60 %.

Recently Mukherjee et al. exploited a reverse-microemulsion method to encapsulate a pyridine-picolinate Mn-complex within porous silica NPs [83]. Thus, aqueous nanodroplets containing the Mn-chelates were first prepared and then the silica nanoparticles were created around the water droplets, thus confining the complexes inside. A size of 14 nm and a $r_1 = 8.46$ mM^{-1} s^{-1} (1.41 T, 298 K), almost three times higher than the free Mn-chelate, were measured for these paramagnetic Si-NPs. It was also demonstrated that the nanoprobes are biocompatible to HeLa cells and stable in the presence of excess Zn^{2+} ions and other physiologically relevant anions (phosphate, citrate or bicarbonate).

Furthermore, Mn-chelates such as mono-hydrated MnEDTA^{2-} and $q = 0$ MnDOTA^{2-} were conjugated to the surface of nanodiamonds (ND). In particular, EDTA-anhydride or activated DOTA-NHS (NHS = *N*-hydroxysuccinimidyl ester) were reacted on the surface of NDs bearing hydroxyl groups or functionalized with amino groups and then the paramagnetic nanoprobe was obtained after Mn^{2+} complexation [84]. Relaxivities $r_1 = 8.1$ mM^{-1} s^{-1} for ND-MnEDTA ($r_2 = 72.7$ mM^{-1} s^{-1}) and $r_1 = 9.4$ mM^{-1} s^{-1} for ND-MnDOTA ($r_2 = 211.7$ mM^{-1} s^{-1}) are reported (7 T, 298 K). Finally, an *in vivo* dual-mode T_1 and T_2 MRI study on a murine hepatic tumour model showed good contrast (both T_{1w} and

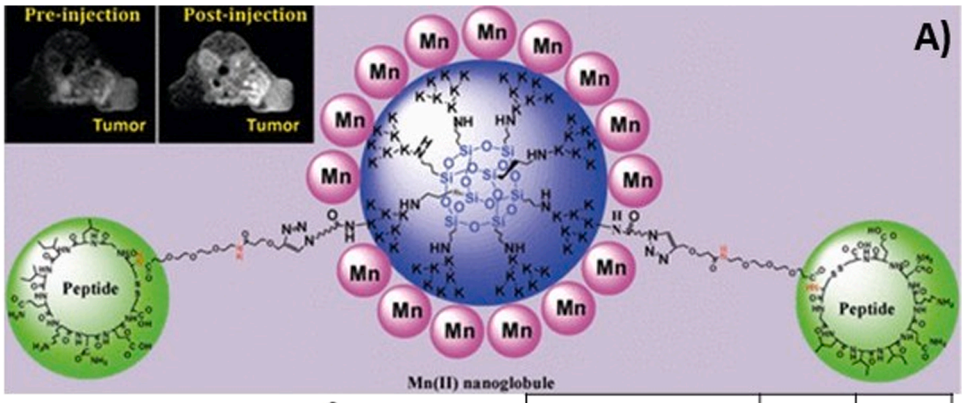

Dendrimer NP	r_1 - 3 T, 298 K	r_2 - 3 T, 298 K
G3-MnDOTA-MA	2.8	12.6
G3-MnNODAGA	3.8	24.5
G3-MnDOTAMA-CLT1	3.13	8.74

Fig. 8. A) Generation 3 silsesquioxane-lysine dendrimer conjugated to DOTA and PLT1 peptide and T_1-weighted MRI of the targeted nanoprobe; B) Mn-DOTAMA and MnNODAGA chelates linked to the G3 dendrimer and relaxivity values of the nanoprobes. (Adapted from Refs. [71 and 72]).

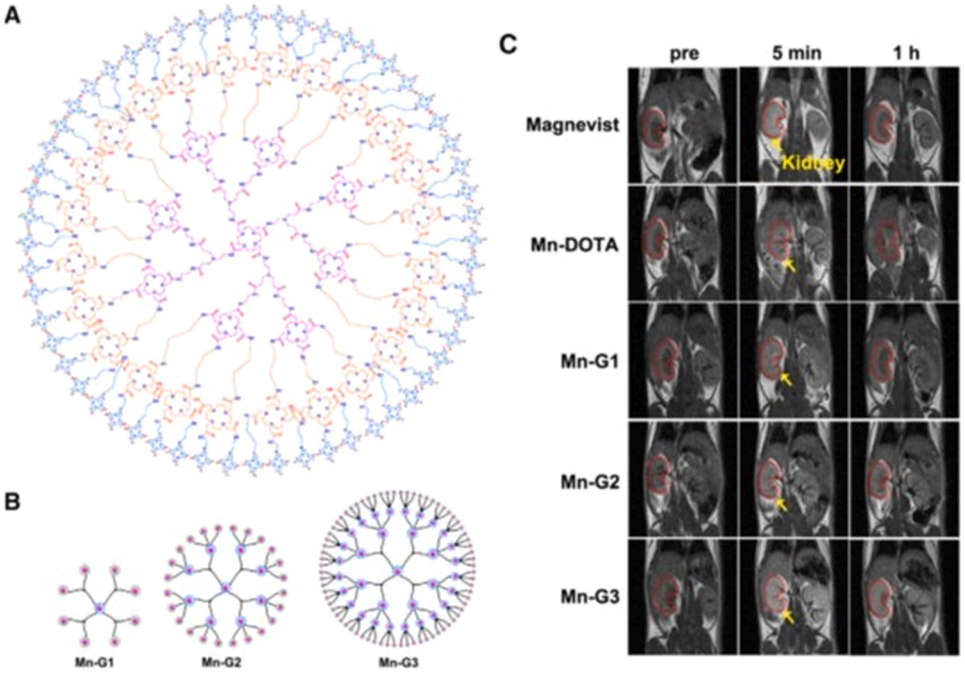

Fig. 9. A) Chemical structure of the third generation (G3) of dendrimeric/multinuclear DOTA-amide system; B) Correspondent Mn-complexes; C) T_1-weighted MR images of mice at 1.0 T before and after intravenous injections of the dendrimers (0.1 mmol/kg body weight) (Adapted from ref. 74).

T_{2w}) between hepatic tumour nodules and normal liver tissue.

Carbon-based Mn-NPs (Mn@CCs) were synthesized by Qui et al. by carbonizing Mn(II)-gluconate and aspartate complexes in an autoclave at 180 °C for 4 h (Fig. 13). The resulting NPs had a size of 11.6 nm and a zeta potential close to zero, ensuring good suspendability in physiological media and serum [85]. High relaxivity values at various magnetic field strengths (31.1 $mM^{-1}s^{-1}$ at 7 T) and good cellular viability in standard cell lines were shown by these Mn@CCs. Additionally, they were capable of crossing the intact blood-brain barrier in healthy mice and were readily excreted via kidneys within 4 h post-injection, with minimal tissue deposition. *In vivo* MRI and light-sheet fluorescence microscopy (LSFM) imaging revealed that Mn@CCs selectively targeted glioma tissues, achieving uniform distribution and high penetration in an intracranial mouse model and enabling a clear delineation of brain tumor edges and multinodular liver tumors. A follow up of this study was performed by Huang et al. who used Mn-loaded carbon dots (Mn-CDs) for the delineation of acute kidney injury (AKI model) [86]. The Mn-CDs, prepared as described previously for Mn@CCs, have a size

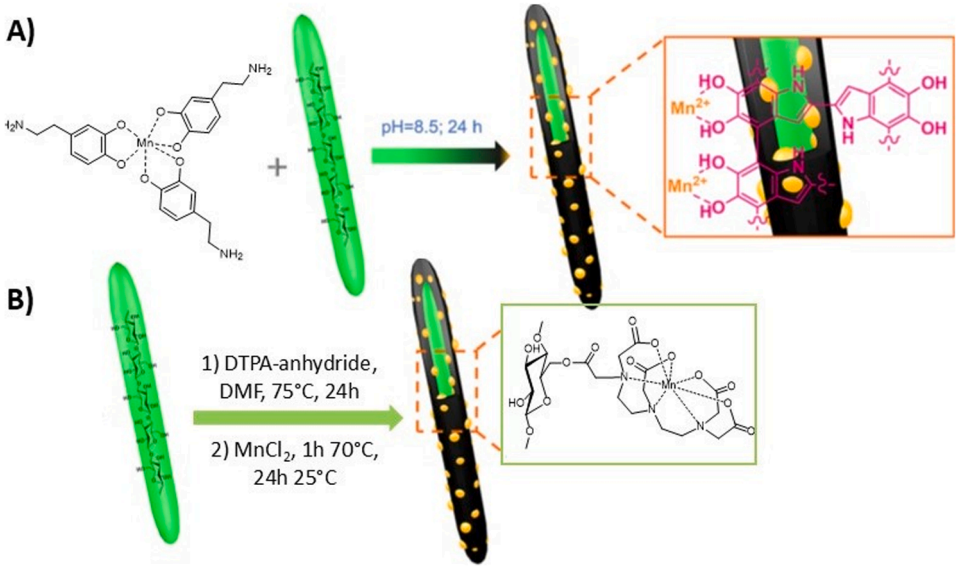

Fig. 10. A) Schematic illustration of the preparation of MnDTPA@CNC nanoparticles and B) of (Mn-PDA)@CNC nanoparticles (Adapted from Refs. [75 and 76).

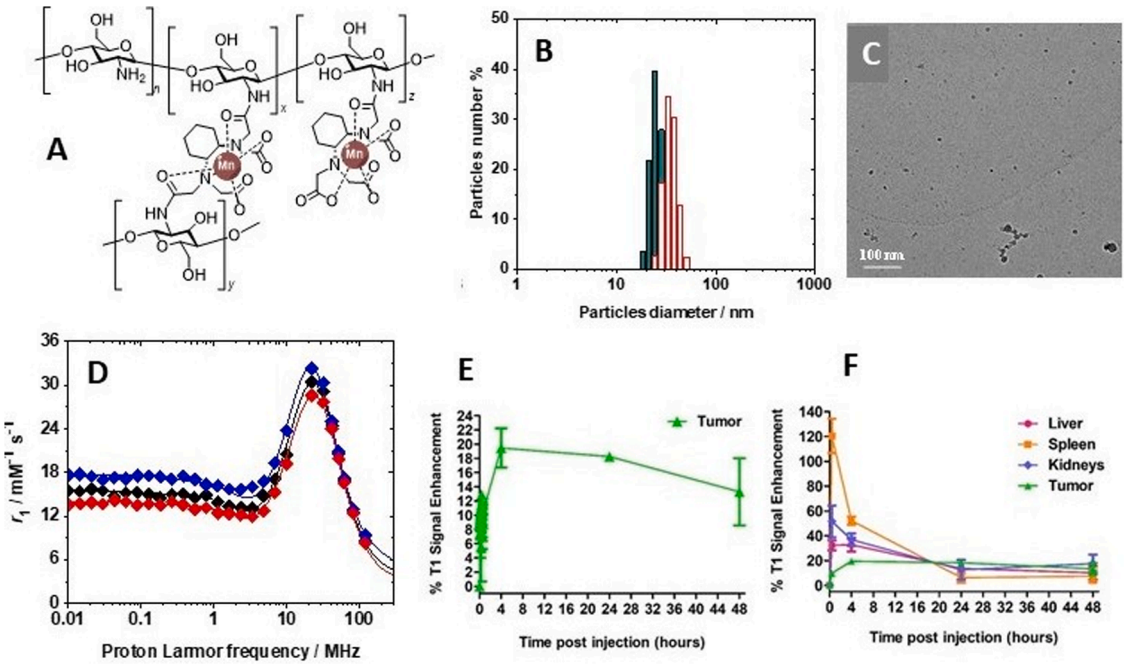

Fig. 11. A) schematic illustration of the MnCDTA-amide NGs; B) NG-1 (green) and Mn-NGs (red) particle size distribution in aqueous solution at physiological pH; C) Cryo-TEM micrographs of Mn-NGs at low magnifications; D) ^{1}H NMRD profiles Mn-NG-1 at neutral pH and at 283 (blue), 298 (black) and 310 K (red); E) % T_1 SE measured in the tumour only and (F) in the liver, spleen, kidneys, and tumour at different time points after intravenous administration of the MnCDTA-amide NGs (Adapted from ref. 79).

of 5 nm, acceptable biocompatibility, and a good r_1 value (10.8 mM^{-1} s^{-1}, 3.0 T). As a result, they achieved substantial signal enhancement in the kidneys, effectively revealing detailed structures such as the cortex, outer, and inner medulla. In the AKI model, CE-MRI using Mn-CDs proved capable of accurately diagnosing the damaged kidney and identifying the injury site by detecting signal variations in the entire kidney and the outer medulla. Additionally, these Mn-NPs, through CE-MRI, could show functional changes in the damaged kidney, encompassing parameters such as peak time, peak value, and relative renal function.

As a final example of this class of Mn-based NPs, we introduce the use of a Mn-(DOPA-EDTA)$^{2-}$ (DOPA = 3,4-dihydroxy-L-phenylalanine) bifunctional chelate for coating superparamagnetic iron oxide (SPIO) nanocrystals to form core-shell NPs [87]. Two types of NPs were produced with 4 and 7 nm size: the latter, with a high r_2/r_1 ratio of 15 at 3 T, tend to work as T_2 CAs while the 4 nm NPs, with a lower r_2/r_1 ratio of 5.3 at 3.0 T (r_1 = 8.4 mM^{-1} s^{-1} at 0.5 T, 298 K), could behave as T_1–T_2 dual-modal CA. *In vivo* imaging with the 4 nm Fe/Mn hybrid NPs allowed efficient vascular imaging showcasing distinct signal intensity variations between the liver parenchyma and blood vessels. This results in a synergistic contrast enhancement for hepatic imaging using both T_{1W} and T_{2W} sequences.

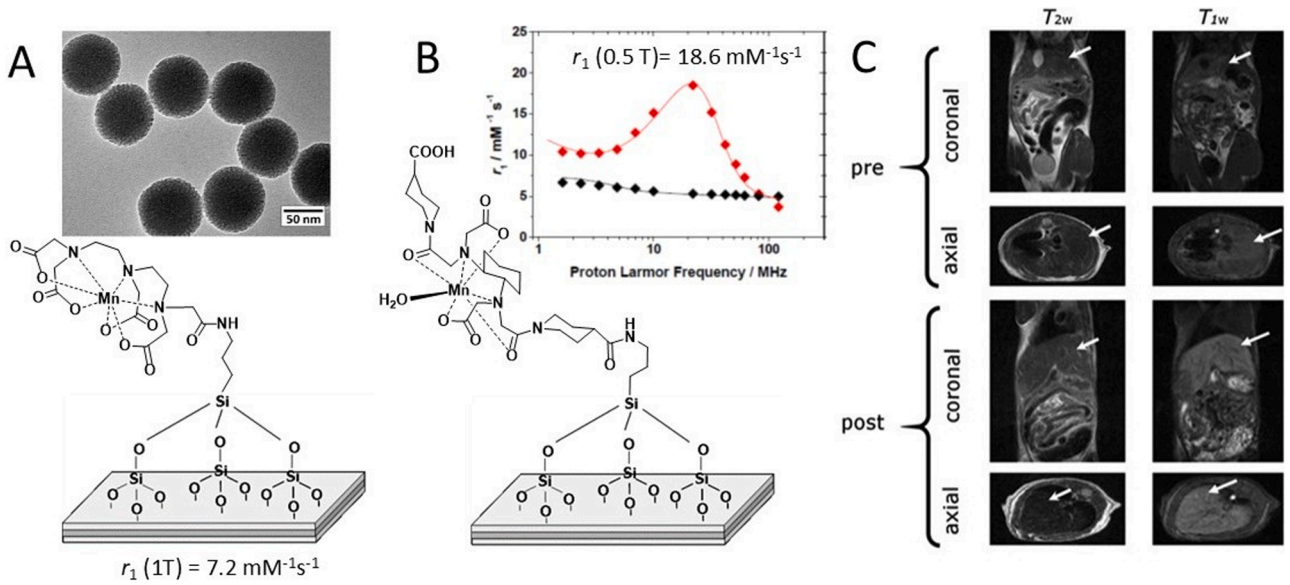

Fig. 12. A. Mn-DTPA-like chelate conjugated to silica NPs of *ca.* 115 nm; B. Mn-CDTA-bis-amide complex conjugated to SiNPs and NMRD profiles in comparison to the free Mn-complex; C. Coronal and axial T_{2w} and T_{1w} MR-images at 1 T of a mouse before and after ($t = 20$ min) intravenous administration of MnCDTA-like-SiNPs. White arrows indicate the mouse's liver (Adapted from Refs. [81,82]).

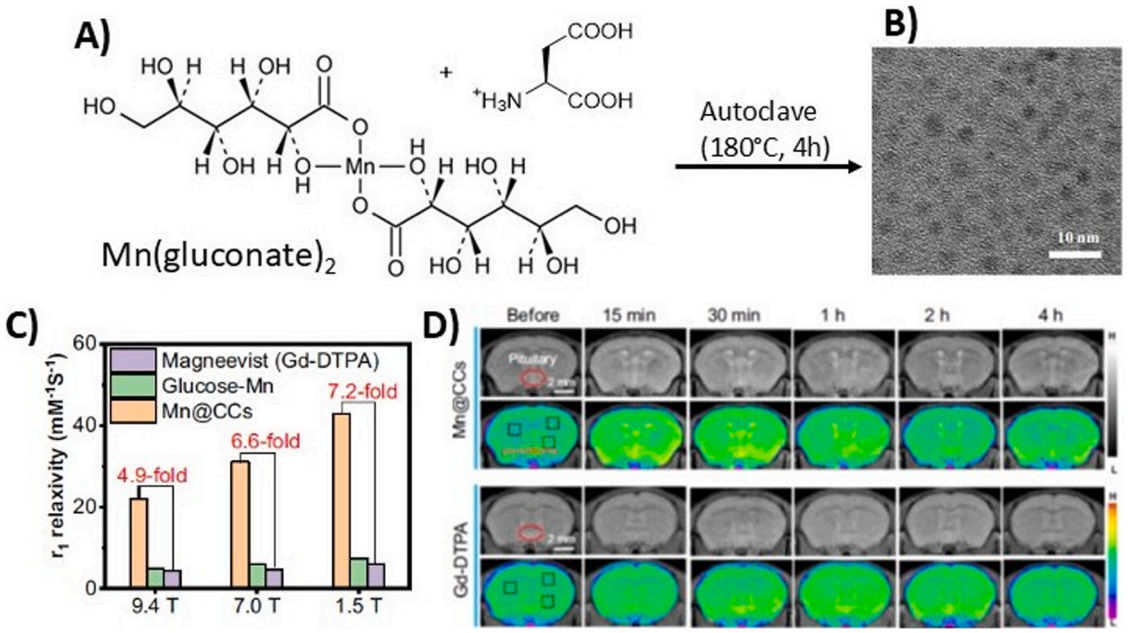

Fig. 13. A) Synthesis scheme of Mn@CC NPs; B) Transmission electron microscopy (TEM) of the 5 nm NPs; C) comparison of relaxivities of Mn@CCs, glucose-Mn, and $[Gd(DTPA)]^{2-}$; D) *in vivo* MR images of healthy mice after *iv* injection of Mn@CCs and $[Gd(DTPA)]^{2-}$. (Adapted from ref 85).

3.1.5. Other types of Mn(II) chelate-containing nanoassemblies

Polydisulfide biodegradable polymeric Mn(II)-based CAs were developed by Ye et al. by reacting DTPA and EDTA-anhydrides with cystamine followed by Mn^{2+} complexation. The MnL-cystamine co-polymers showed r_1 and r_2 of 4.74 and 10.38 mM^{-1}s^{-1} at 3T for Mn-DTPA (M_n = 30.50 kDa) and 6.41 and 9.72 mM^{-1}s^{-1} for Mn-EDTA (M_n = 61.80 kDa). Both polydisulfide MnL polymers were bio-degraded at different rates (Mn-EDTA polymers faster than MnDTPA ones) after incubation in 15 μM cysteine aqueous solution (the plasma concentration of free thiols) at physiological pH. Finally, injection of both paramagnetic polymers in mice bearing MDA-MB-231 human breast cancer showed high liver, myocardium and tumor MR-enhancement [88].

Another polymeric Mn-based CA was recently proposed by Fu et al. who synthesized in one-pot a pyridine-bis-acylhydrazone $q = 2$ Mn(II)-chelate copolymerized with PEG2000 polymers. The P(MnL-PEG)-3 polymer, obtained by using a 72 h polymerization time, showed an ultrasmall 1.5 nm size and a r_1 of 23.9 mM^{-1} s^{-1} at 1.5 T. After *i.v.* injection of 0.05 mmol of Mn/kg of BW), the distribution of P(MnL-PEG)-3 and its metabolic pathway in female BALB/c mice showed an initial localization in organs such as the liver and kidneys followed by hepatin and renal excretion within 48 h. Finally, the potential of P(MnL-PEG)-3 for liver cancer detection was assessed by injecting the polymeric agent in mice bearing an orthotopic H22 liver tumors, which allowed the clear visualization of H22 liver tumor boundaries [89].

Chen et al. reported the formation of a Mn(II)-containing nanosystem

able to act as a theranostic agent through T_1 MRI contrast enhancement and phototherapy of hypoxic cancer. In particular, a Mn(II) complex with a functionalized bis(2-pyridylmethyl)amine (PDPA) ligand interacts via hydrogen bonding with a BODIPY (boro-dipirromethene) derivative able to aggregate in a supramolecular structure probably thanks to the interaction between aromatic anisole and phthalate moieties (Fig. 14) [90]. This supramolecule was then embedded within bovine serum albumin (BSA) and conjugated to polyethylene glycol–folic acid (PEG–FA) via dicylohexylcarbodimide (DCC) activation to obtain spherical NPs with 5 nm size. At pH 5 the BODIPY unit in these NPs exhibits the ability to catalyse the water oxidation reaction when exposed to red-light emitting diode (LED) light, resulting in the production of O_2 and heat, and thus acting as a phototherapeutic agent. Moreover, the paramagnetic NPs have a high relaxivity of *ca.* 40 mM^{-1} s^{-1} at 3.0 T and could selectively accumulate in the tumour tissues with distinct T_1 MRI signal enhancement. The nanosystems also demonstrated an efficient inhibition of tumour growth *in vivo* while maintaining a low toxicity to the healthy organs.

Another theranostic system was assembled by Shen et al. by using a near-infrared (NIR) light activated upconverting nanoplatform conjugated to a Mn-porphyrin-like chelate-Human Serum Albumin (HSA) adduct and to an acyclic Arg–Gly–Asp peptide (cRGDyK) with the aim to target glioma tumours, visualise them by T_1 MRI and treat by photodynamic therapy (PDT) [91]. In more detail (Fig. 15), monodisperse $NaScF_4$:Yb(40 %):Er(2 %) NPs were first synthesised and coated with a CaF_2 shell to obtain the upconverting platform. The surface was then coated with polyacrylic acid (PAA) in order to conjugate the carboxylates to the lysine amino groups of the adduct between HSA and the Mn(II)-Chlorin-e6 (Ce6) complex by EDC/NHS (ECD =1-ethyl-3-(3--dimethylaminopropyl)carbodiimide) approach. The further functionalization with a thiolated RGD peptide was accomplished after modification of the protein with a sulfo-SMCC crosslinker (sulfo-SMCC = 4-(*N*-Maleimidomethyl)cyclohexane-1-carboxylic acid 3-sulfo-*N*-hydroxysuccinimide ester sodium salt). For glioma-targeting PDT, the Ce6-Mn complex was excited by irradiation with a 980-nm NIR laser light to produce reactive oxygen species (ROS) and then activate U87 cell apoptosis and abolish glioma tumour growth through energy transfer from the upconverting NPs, with a high emission intensity at 660 nm. The relaxivity of this nanoconstruct at 7 T was 21.5 mM^{-1} s^{-1}, about 2.9 times higher than that of the Mn-Ce6 precursor. Finally, *in vivo* T_1-weighted MRI at 24 h post-injection showed an intensity five-fold higher in the U87 tumour area compared to the healthy tissue.

A MRI/PTT theranostic nanosystem was proposed by An et al. who complexed Mn(II) ions on the negatively charged surface of titanium carbide (Ti_3C_2) two-dimensional nanosheets [92]. Then, in order to improve the water solubility and biocompatibility, cooperative electrostatic self-assembly with NH_2-PEG molecules was carried out (Mn-Ti_3C_2@PEG). Unfortunately, the relaxivity of this system is quite low (r_1 = 1.05 $mM^{-1}s^{-1}$ at 3 T) and no stability studies were reported. However, due to Fenton-like catalytic and magnetic properties of Mn-units, Mn-Ti_3C_2@PEG NPs were also able to convert cellular H_2O_2 into highly toxic OH radicals for chemodynamic therapy (CDT). In order to highlight the theranostics potential, simultaneous MRI and dual-modal PTT and CDT treatment was also tested for effective tumour elimination with reduced side effects both *in vitro* and *in vivo*.

In a last example of this class, a semiconductor Ag−In−Ga−Zn−*S* quantum dot (QD) was doped with Mn(II)-stearate to investigate the influence of the Mn^{2+} loading on the photoluminescence (PL) and the potential applicability for bimodal PL/MRI probes [93]. Mn:AIGZS QDs were then suspended in aqueous solution using glutathione (GSH) tetramethylammonium that substitutes the native oleylamine ligands and binds to the surface of the QDs via metal−*S* bonds. Mn:AIGZS QDs showed a size of ~2 nm, a high PL quantum yield (up to 41.3 % for a 2.5 % doping in Mn^{2+}), and good photo- and colloidal stabilities. The quite low relaxivity of Mn:AIGZS QDs (r_1 = 0.15 mM^{-1} s^{-1} and r_2 = 0.57 mM^{-1} s^{-1} at 298 K and 2.34 T) can be interpreted by the presence of a large amount of Mn^{2+} ions inside the nanoparticles that are silent from a relaxometric point of view, since not involved in magnetic coupling with the solvent molecules.

3.1.6. *Mn-containing metal organic frameworks (MOFs)*

Metal–organic framework (MOF) are hybrid materials with periodic structure obtained by self-assembly of inorganic building blocks (*i.e.* often metal ions) with organic linker molecules. In particular, the building blocks are assembled by coordination of the positively charged metal-containing units by the neutral or negatively charged organic moieties. The possibility to obtain highly functionalized hybrid crystalline porous nanomaterials has opened the door to their biomedical application as theranostic or MRI CAs [94–96]. The main field of research on MOFs for MRI applications is focused on Gd-systems, but a

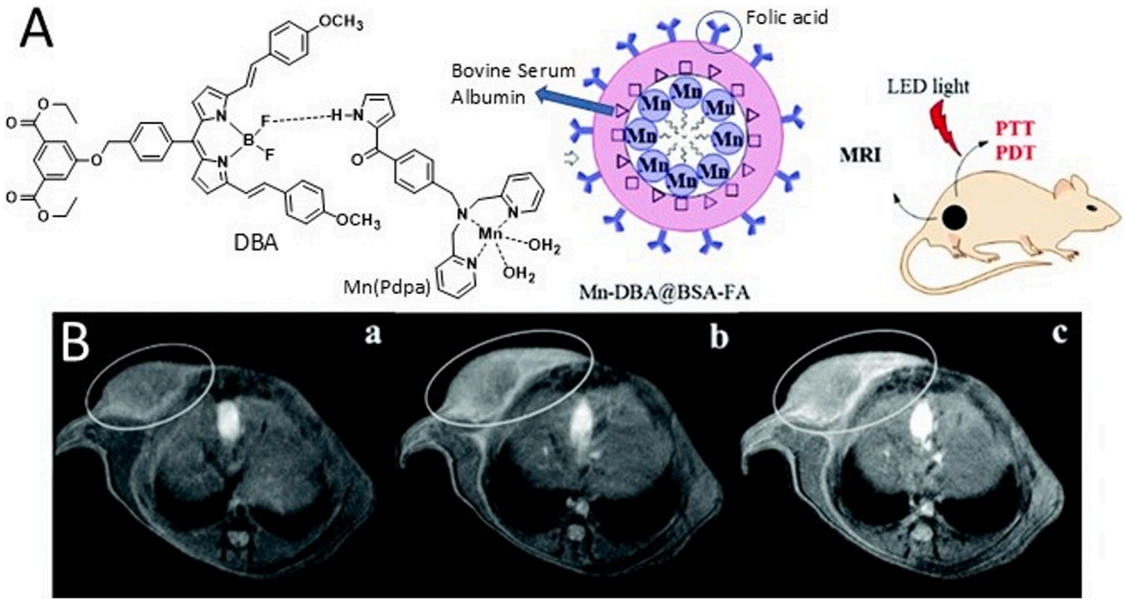

Fig. 14. A. Schematic illustration of Mn-DBA@BSA-FA nanoparticles for theranostic MRI and PDT applications. B. *In vivo* T1-weighed MR imaging of HepG-2 tumour bearing mice at three time points after the intravenous administration of Mn–DBA@BSA-FA NPs (a, 0 min; b, 10 min; c, 20 min) (Adapted from ref 90).

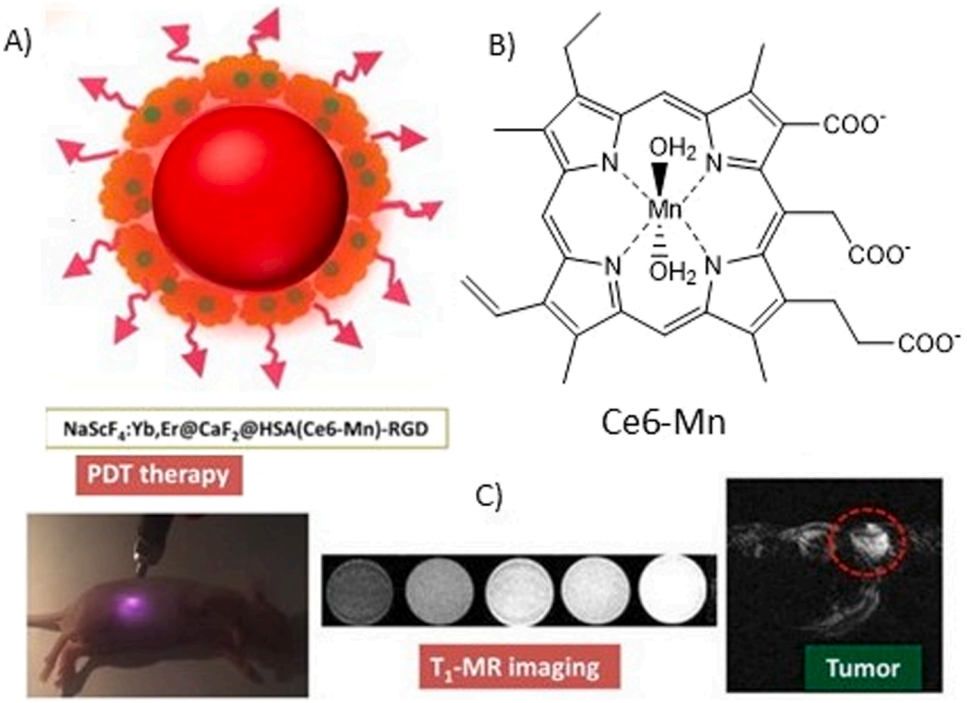

Fig. 15. A) Schematic illustration of the near-infrared (NIR) light activated upconverting nanoplatforms conjugated to a Mn-porphyrin-like chelate (Ce6-Mn, B)-HSA adduct and to cRGDyK peptide. C) Illustration of the application of the probe for photodynamic therapy and T_1-weighted MRI (Adapted from ref 91).

few examples on Mn(II) based MOFs have also been reported [96].

The first example was reported by Taylor et al. who synthesized, in reverse-phase microemulsion at room temperature or under microwave irradiation, Mn-MOFs with terephthalic and trimesic acid as bridging structures (Fig. 16A) [97]. The NPs were also coated with a thin silica shell and conjugated to a RGD peptide and a fluorophore (Fig. 16B). Large rod-shaped NPs were obtained depending on the synthetic procedure, showing r_1 values up to 7.8 mM^{-1} s^{-1} and r_2 of 70.8 mM^{-1} s^{-1} at

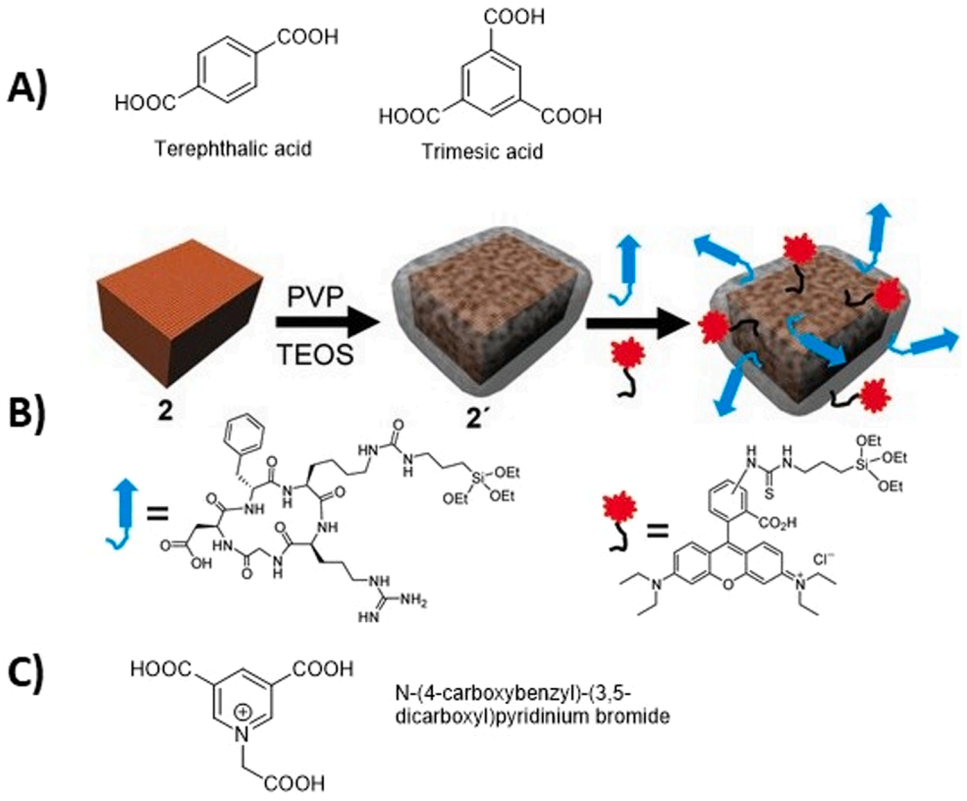

Fig. 16. A) and C) Chemical structure of the building blocks used for Mn-MOF synthesis. B) Schematic illustration of the preparation of Mn-MOF-RGD-FITC (Adapted from Refs. [97,98]).

3 T. However, leaching studies indicated that these Mn-MOFs release 50 % of free Mn^{2+} ions in 7.5 h, thus confirming that their expected toxicity is the key disadvantage of these Mn-MOF NPs. Then, in 2017, Qin and co-workers reported a zwitterionic Mn-MOF based on N-(4-carboxybenzyl)-(3,5-dicarboxyl)pyridinium bromide as the organic bridging ligand (Fig. 16C) [98]. The NPs had a hydrodynamic diameter of *ca.* 80 nm and r_1 of 17.5 $mM^{-1}s^{-1}$ at 0.5 T, quite stable over 24 h both in deionized water and in Tris–HCl buffer. *In vivo* studies showed a positive signal enhancement after 15 min in both kidneys, persisting for about 240 min and then slightly attenuating after 24 h. The low accumulation in liver suggests a renal clearance that, however, requires particles disintegration into smaller size macromolecules and gradual degradation over time before excretion. Another Mn-MOF has been recently reported made by dropwise mixing of 2,5-dihydroxyterephthalic acid (DHTP) and Mn(II) acetate and successively functionalized with variable number of PEG-5000 moieties to avoid aggregation phenomena (Fig. 17A) [99]. The size of the NPs was around 20–50 nm and the longitudinal relaxivity in PBS (phosphate-buffered saline), at 1.0 T and 24 °C, reached a value of 13.5 $mM^{-1}s^{-1}$ (r_2 = 46.8 $mM^{-1}s^{-1}$). Finally, a PBS solution of the Mn-MOF NPs was injected in a colon-26 tumour--bearing BALB/c nude mouse showing a 117 % signal enhancement in tumour at 30 min post-injection (Fig. 17B). Finally, a coordination polymeric nanoplatform based on Mn(II)-methotrexate (MTX) adducts coated with PEG moieties was reported as a theranostic nanosystem for MRI guided chemotherapy (ChT) [100]. The size of the amorphous NPs obtained was around 90 nm and r_1 = 7.8 $mM^{-1}s^{-1}$ at 0.5 T. The idea was that degradation of MOF NPs would have released the chemotherapeutic drug in the tumour, after accumulation via the enhanced permeability and retention (EPR) effect. Unfortunately, together with the release of MTX, also toxic Mn^{2+}ions are released into the body.

Finally, Yu et al. reported the Mn(II)-PBC MOF (PBC = pyridine-3,5-bis(phenyl-4- carboxylate), with r_1 = 3.73 mM^{-1} s^{-1} (0.5 T), suitable for T_{1w} MRI contrast. Mn(II)-PBC produced two kinds of free radicals ($O_2^{\cdot}$ and $OH^{\cdot}$) in the presence of methylene blue to kill HeLa cancer cells through the CDT mechanism. The DOX-loaded MOF (DOX@Mn(II)-PBC) released the anticancer drug efficiently at the acidic pH (pH =5.0) of the tumour microenvironment (TME), showing high toxicity to HeLa cells. Thus, the DOX@Mn(II)-PBC) MOFs displayed promising theranostic properties *in vitro* for application as a T_{1w}-MRI CA and for tumor multimodal (ChT/CDT) therapy [101].

Several porphyrinic MOFs with the framework formed by Mn^{2+}-chelated porphyrins as organic ligands have been reported, some of which incorporating additional imaging or therapeutic components as multifunctional nanocomposites. Hang et al. reported an MRI guided chemodynamic and sonodynamic therapy (CDT/SDT) theranostic nanosystem made up of Mn(II)-TCPP ions (TCPP = 5,10,15,20-tetrakis (4-carboxyphenyl) porphyrin) connected by Gd(III) ions (GMT) nanosheets (NSs) encapsulated with pluronic F-127 to form a sonosensitizer (GMTF NSs), where the reduction of the HOMO-LUMO energy gap led to the production of ROS in high yields upon US irradiation, effective for SDT. The Mn^{2+} ions generated hydroxyl radicals through a Fenton reaction capable of inducing cell death via the CDT mechanism. The Mn (II) and the Gd(III) ions in the NSs led to a large r_1= 4.4 mM^{-1} s^{-1} (3.T). SDT and CDT were used to inhibit colon cancer tumour growth in CT26 tumor-bearing mice, monitored by time-dependent *in vivo* T_{1w} MRI images upon i.v. injection of GMTF NSs [102]. In another example, Geng et al. reported Mn(II)-PpIX (protoporphyrin *IX*) coordination polymers (MnPPs) as efficient nanosystems for MRI guided synergistic PDT/SDT theranostics, as shown by *in vivo* tumor mice studies under light/US irradiation [103].

3.1.7. Paramagnetic Mn(II) clusters and other inorganic NPs

Another approach to nanosized Mn(II)-based systems is the cluster-nanocarrier design. Since clusters have high tendency to speciate,

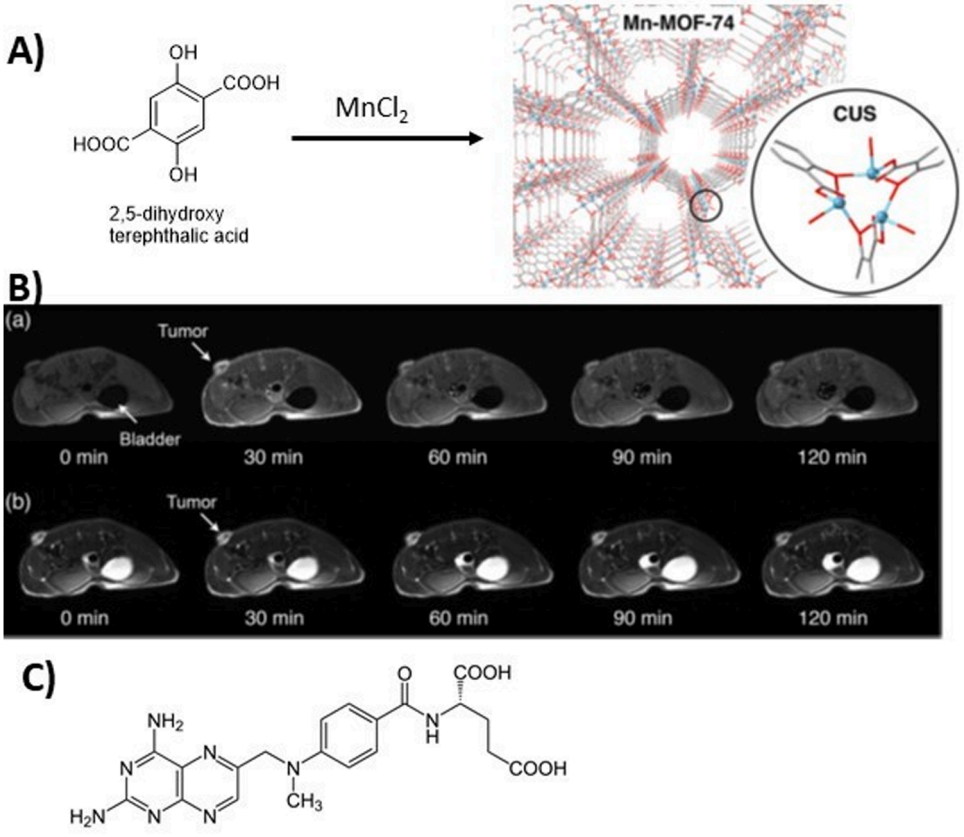

Fig. 17. **A**) Scheme of the preparation of Mn-MOF-74; **B**) Time course of (a) T_1- and (b) T_2-weighted MR images of colon-26 tumour-bearing BALB/C mouse after administration of PEG1-Mn-MOF-74; C) Chemical structure of methotrexate (Adapted from Refs. [99,100]).

polymeric nanocarriers were used by Dahanayake et al. to stabilize a $Mn_3(O_2CCH_3)_6(Bpy)_2$ (Bpy = bipyridyl) cluster and prevent both speciation and metal leaching [104]. This cluster has a linear trinuclear array of Mn(II) atoms bridged by acetate groups and the metal ions are weakly antiferromagnetically coupled based on magnetic susceptibility and electron paramagnetic resonance measurements. Then, monodispersed polymer nanobeads, termed Mn_3Bpy-Pam, were formed in acrylamide using the inverse-miniemulsion technique (size 125 nm) (Fig. 18). Unfortunately, the suspension of Mn_3Bpy-Pam in water led to substantial swelling due to the polymer's hydrophilicity, resulting in an increase in the hydrodynamic diameter to ~221 nm. The relaxivity at 9.4 T, 25 °C and pH 7 of Mn_3Bpy-Pam increased dramatically compared to the cluster alone: $r_1 = 54.4\ mM^{-1}\ s^{-1}$ and $r_2 = 144\ mM^{-1}\ s^{-1}$ ($r_1 = 6.9\ mM^{-1}\ s^{-1}$ and $r_2 = 124.7\ mM^{-1}\ s^{-1}$ for the cluster). The leaching of free Mn^{2+} ions was measured in different media and the highest release detected over a 7-day period was 0.35 % of the initial composition. The authors studied also the possibility to functionalize the surface of the nanobeads by the addition of a co-monomer bearing a free amino group (*i.e. N*-(3-aminopropyl)methacrylamide) to the miniemulsion polymerization. The amino groups on the surface were then reacted to a near-IR cyanine dye and to a folate-receptor targeting ligand such as methotrexate. *In vivo* MRI was finally performed by injecting the particles both in healthy and tumour bearing mice observing a signal enhancement in T_1-weighted images considerably higher compared to $[Gd(DTPA)]^{2-}$.

Akhmadeev et al. introduced the use of hexarhenium clusters ($[\{Re_6Q_8\}(CN)_6]^{4-}$, $Q = S^{2-}$, Se^{2-} or Te^{2-}) for the construction of Mn(II) based NPs stabilized by using different types of pluronic (F-68, P-123, F-127) to improve the colloidal stability [105]. The results highlighted that the $K_{4-2x}Mn_xRe_6Se_8$ NPs decorated by F-127 have a hydrodynamic diameter of 180 nm, good relaxivity ($r_1 = 8.9$ and $r_2 = 10.9\ mM^{-1}s^{-1}$ at 0.47 T and 310 K), low levels of hemoagglutination activity and low cytotoxicity. The leaching of Mn^{2+} ions from the NPs in buffered solutions of BSA-based model plasma was lower than 5 % after one week and their T_1- and T_2-weighted contrast ability was validated through phantom imaging at a whole body 1.5 T scanner.

With the aim to develop a facile method to prepare a nanosized CA able to provide multimodal imaging ability in the same system, a facile one-step hydrothermal procedure was used to synthetise hyaluronic-acid-modified Mn-tungstate NPs (HA-$MnWO_4$ NPs) [106]. Beside the paramagnetic behaviour of Mn(II) for T_1/T_2-weighted MRI applications, tungsten with high atomic number provides high X-ray attenuation coefficient for CT imaging. The NPs had a plate like shape, a hydrodynamic diameter of 164.1 nm and quite low relaxivities of 0.78 $mM^{-1}s^{-1}$ (r_1) and 6.67 $mM^{-1}s^{-1}$ (r_2) at 1.2 T. Furthermore, both *in vitro* and *in vivo* toxicology assessments demonstrated the low toxicity and good biocompatibility of HA-$MnWO_4$ NPs. Additionally, T_1/T_2-weighted MR and CT imaging revealed a substantial contrast effect, clearly displaying liver structures through CT imaging and renal structures through MR imaging. Moreover, the presence of hyaluronic acid allowed good targeting ability as demonstrated by cellular assay and *in vivo* tumour MR imaging.

Finally, in analogy with variably coated Gd fluorides NPs which have demonstrated high efficiency as MRI CAs [107,108], pegylated fluoroperovskite $KMnF_3$ nanoparticles were developed by Liu et al. as T_1 weighted CA with high longitudinal relaxivity at 3 T (r_1 = 23.15 $mM^{-1}s^{-1}$) and low r_1/r_2 ratio (3.2) [109]. Cytotoxicity tests proved that the PEGylated $KMnF_3$ NPs are non-toxic and *in vivo* MRI study distinctly showcased good biocompatibility and detailed anatomical characteristics in brain imaging at a low dosage of 5 mg of Mn per kg, with potential renal clearance attributed to their small size (20 nm).

3.2. Mn(III) systems

The Mn(III)- porphyrin NPs are the only Mn(III)-based nanosystems covered in this review, as Mn_3O_4 (oxo) [27–31,110,111] and polyoxo based NPs are excluded [112–114]. Mn(III)-porphyrins, such as Mn

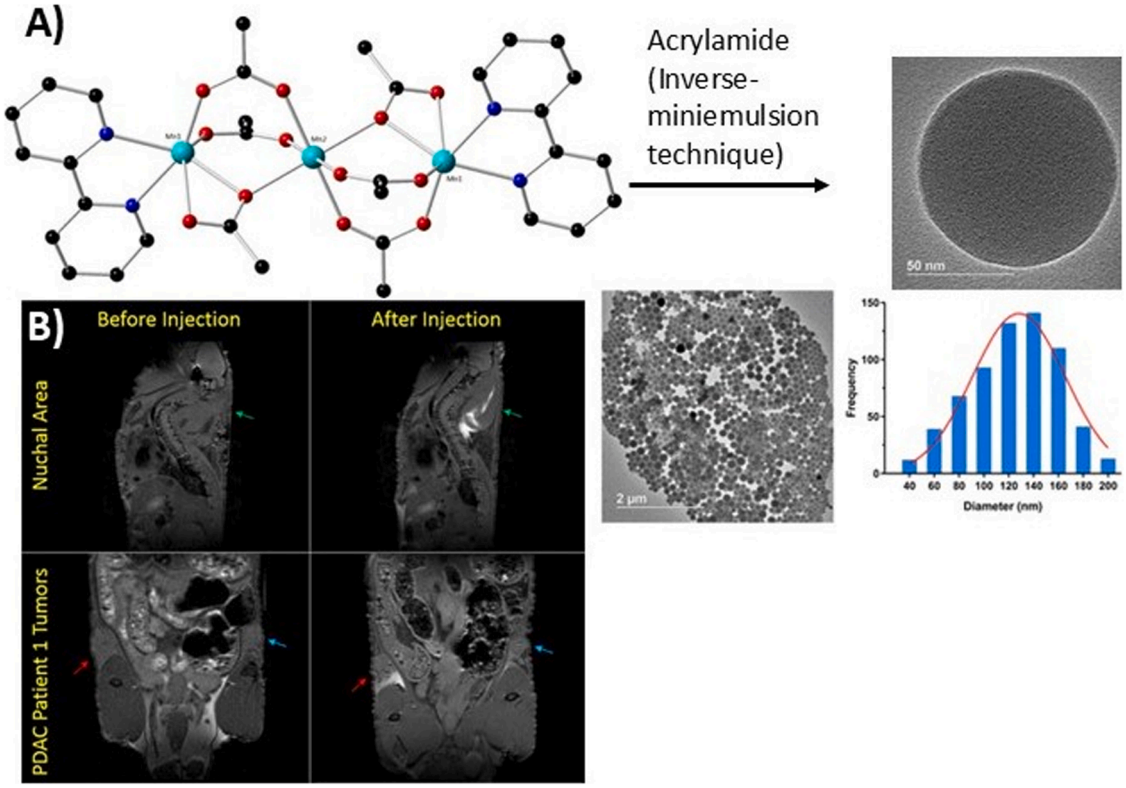

Fig. 18. A) Schematic representation of the synthesis of Mn_3Bpy-PAm nanobeads, TEM image with average size of 125 ± 35 nm; B) T_{1w} images of the nuchal area administered with Mn_3Bpy-PAm NPs (green arrow), (top). Pancreatic Ductal Carcinoma (PDAC) tumour sites administered with Mn_3Bpy-PAm NPs (red arrow) and $[Gd(DTPA)]^{2-}$ (blue arrow), (bottom) (Adapted from Ref. [104]).

(III)-TPPS$_3$NH$_2$, have high thermodynamic stability and kinetic inertness (see Section 2.1.3).

3.2.1. *Mn(III) porphyrins NPs as MRI CAs*

Many studies have reported nanoparticles containing Mn(III) porphyrins in their structure as MRI CAs [115]. Here some examples of Mn (III)-porphyrins conjugated to proteins or incorporated in micelles, liposomes, polymers, hydrogels, MOFs, virus capsids and microbubbles are described as potential MRI CAs (Fig. 19). Porphyrin-based MOFs comprise two categories, porphyrin@MOFs and porphyrinic MOFs, depending on the role of the porphyrins/metalloporphyrins in the MOFs. While in porphyrin@MOFs, they are guest molecules bound within the MOFs pores by host-guest interactions or bound at the MOFs surface, in porphyrinic MOFs they are part of the MOFs framework as organic ligands bridging metal ions or clusters [116].

Self-assembly of amphiphilic porphyrins obtained from hydrophobic analogues was used to obtain micelles incorporating Mn(III) porphyrins. This is the case for micelles formed by conjugation of Mn(III)-5,15-diphenylporphyrin to an amphiphilic PEG-dendron, which have a low r_1 = 5.0 s^{-1} mM^{-1} (9.4 T) due to their high degree of local mobility [117]. Self-assembly of an amphiphilic block copolymer (P(PEGMA--co-APMA)-b-PMMA, APMA = *N*-(3-Aminopropyl)methacrylamide) containing the Mn(III)-TCPP porphyrin led to higher r_1 = 9.53 s^{-1} mM^{-1} (3 T) due to the restricted mobility of the cross-linked amphiphilic chains [118].

Evaluation of the dextran-conjugated Mn(III)-5-(4-aminophenyl)-10,15,20-tris(4-sulfonatophenyl) porphyrin showed high *in vitro* r_1 = 8.90 mM^{-1} s^{-1} (4.7 T) of the conjugate and tumour targeting specificity shown in T_{1w} MRI of ICR male mice implanted with H22 hepatoma tumour upon *i.v.* administration of the Mn(III)-porphyrin [119].

Vollett et al. reported HSA conjugates of the Mn(III)-TPPS$_3$ porphyrin producing a large reduction in T_1 values, with relaxation rates increasing linearly with the degree of HSA tagging and with a relaxivity r_1 of 15.4 mM^{-1} s^{-1} when using 0.05 mM of bound MnTPPS$_3$, as shown by *in-vitro* MRI (1.5 T). These results suggested that MnTPPS$_3$NCS is a very good platform for protein conjugation [43].

Hong and colleagues reported a new NO-activatable T_1 MRI CA based on the Mn(III)-TPPS$_3$-diaminotoluene conjugated to the NO-responsive group *N*-acyl-*o*-phenylenediamine, which, in the presence of NO under aerobic conditions, is converted to an acyl benzotriazole that is cleaved, allowing the MRI-active Mn(III)-porphyrin to acylate proteins and accumulate in inflammed tissue. Its efficacy in detecting NO *in vivo* in a mouse model of myocardial inflammation was verified by the observed enhancent of T_1 MRI contrast in response to the high endogenous NO levels [120].

Liposome-like porphysome nanovesicles were built using the porphyrin-phospholipid (PoP) conjugate Mn(III)-HPPH-lipid (Fig. 19, HPPH is 1-hexyloxyethyl]−2-devinyl pyropheophorbide-*a*) and Mn(III)-*N*-HPPH-lipid (*N*—HPPH is the amine-modified version of HPPH-lipid). The capacity of amines of forming hydrogen bonds with water led to an increase of the intra-bilayer water content, which improved the r_1 and MRI contrast in Mn-PoP bilayers. Mn(III)-HPPH is located inside the hydrophobic bilayer of the PoP vesicle, where only a small number of water molecules can get access, leading to a lower relaxivity (r_1 = 0.98 s^{-1} mM^{-1}) than that of Mn(III)N—HPPH-lipid nanovesicles (r_1 = 2.46 s^{-1} mM^{-1}). This was confirmed using MD calculations by the presence, inside the hydrophobic bilayer, of a much higher amount of water molecules hydrogen bonded to *N*—HPPH [121].

A Mn(III)-bacteriopheophorbide (Mn(III)-Bpheid) was evaluated as a potential MRI CA. It showed in solution a high r_1 (29.1 mM^{-1} s^{-1}, at 4 T), possibly due to self-aggregation in solution. Mn(III)-Bpheid showed tumour targeting specificity and accumulation, as monitored by T_1-weighted MRI (7 T) in C6 glioma bearing CD1 mice after *i.v.* injection of the Mn(III) conjugate [122].

The Mn(III)-PP (PP= protoporphyrin IX, Fig. 19) was conjugated with a cross-linked polymer, obtained from aminoethyl methacrylate and N,N'-methylenebisacrylamide (x-AEA), and loaded into the bacteriophage P22 virus capsid cavity (90 to 3646 molecules *per* capsid) (P22-xAMEA-Mn(III)-PP). The relaxivity for the loaded capsids was found to be little dependent on the loading degree and almost equal to that of free Mn(III)-PP, r_1 = 1.5–3.7 mM^{-1} s^{-1} (2.1 T, 298 K), leading to huge r_1 relaxivities *per* particle (eg. $r_{1,particle}$ = 7098 mM^{-1} s^{-1} (298 K, 2.1 T) for a 3646 Mn(III) PP molecules loading/capsid). The low r_1 values of Mn (III)PP were attributed to the self-assembly of the Mn(III)PP units inside

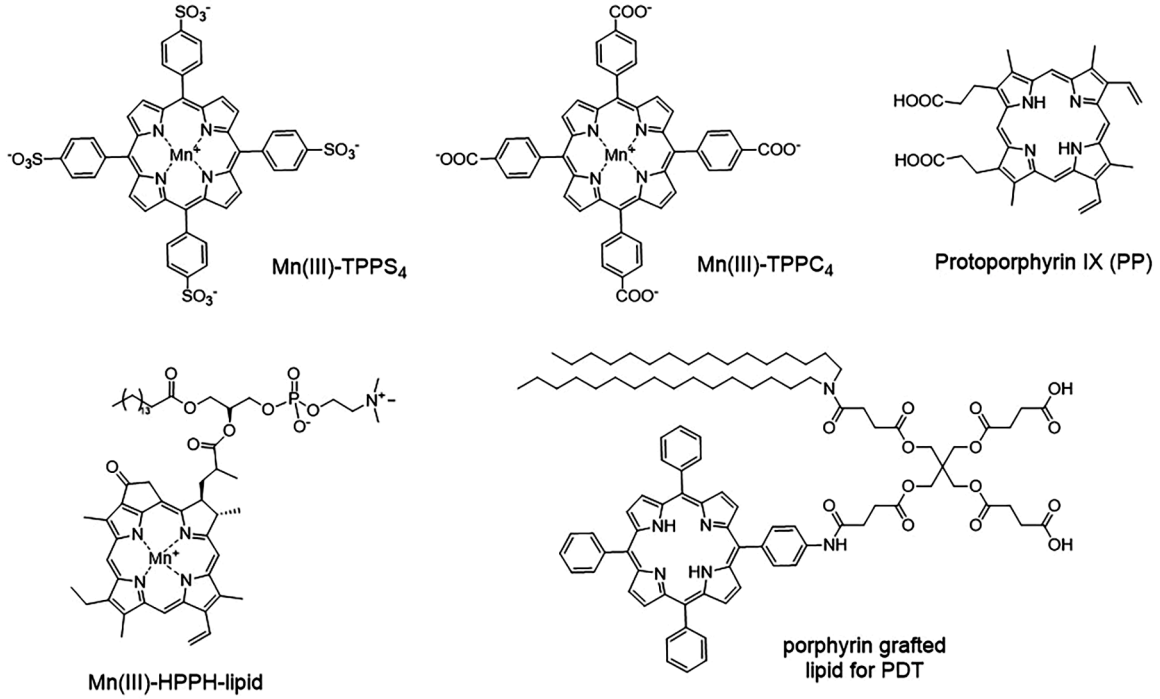

Fig. 19. Representative structures of porphyrins used for the preparation of Mn(III)-based NPs.

the capsid. Much higher r_1 values result for NPs having the Mn(III)-porphyrin complexes located at its outer surface. Antiferromagnetic coupling between neighbouring Mn(III) cations inside the capsids justified their observed decrease of r_2 when the Mn(III)PP degree of loading increased. This *in vitro* study showed that these capsids have potential as efficient positive MRI CAs [123].

Finally, a Mn(III)-porphyrin-graft lipid (PGL, Fig. 19) was encapsulated in the inert gas perfluoropropane forming gas-encapsulated microbubbles (MBs). The MnP-MBs were characterized by UV–vis spectrophotometry and optical microscopy, showing the effectively dispersed MBs (average diameter ~1.14 μm). The effect of ultrasound (US) exposure of MBs was their efficient conversion into smaller NPs, with 20–70 nm diameters (TEM) and hydrodynamic diameters in water suspensions in the 40 −150 nm range obtained by dynamic light scattering (DLS), which could be a consequence of the MnP NPs hydration in solution. US images of MnP-MBs in a latex tube showed an *in vitro* contrast enhancement with increasing concentrations, with potential for *in vivo* contrast-enhanced ultrasound (CEUS) imaging. The MnP NPs had r_1 =1.61 mM^{-1} s^{-1} (7 T). Their ability as an *in vivo* MRI CA in T_{1w} images, as well as enhanced US imaging ability were proven after i.v. injection in U87 glioblastoma tumour-bearing nude mice. Under the guidance of US imaging, they caused *in vivo* tumour MRI contrast enhancement in <30 min [124].

3.2.2. Mn(III) porphyrins NPs in MRI guided theranostics

NPs incorporating Mn(III) porphyrins are versatile platforms for MRI-guided theranostics. This is illustrated here with some examples for chemotherapy (ChT), photothermal therapy (PTT), radiotherapy (RT), photodynamic therapy (PDT), and sonodynamic therapy (SDT). Their main characteristics are summarized in Table 3. Many of the examples involve tumour theranostics, due to the known tumour affinity of Mn (III) porphyrins [44].

3.2.2.1. MRI-guided chemotherapy. Mn(III)-labelled nanobialys NPs of toroidal shape (with diameter of 190 nm) were formed as inverted micelles resulting from self-assembled amphiphilic branched polyethyleneimine (PEI) and linoleic acid, with Mn(III)-PP and biotin-caproyl-DSPE bound at the surface. Their r_1 = 3.7 mM^{-1} s^{-1} (1.5 T, 298 K) resulted from the water exposure of the Mn(III)-PP complexes. However, these NPs had very high relaxivities per particle (r_{1part} = 612 307 mmol [nanobialy])$^{-1}$ s^{-1} and r_{2part} = 866 989 mmol [nanobialy])$^{-1}$ s^{-1}) as a consequence of each containing about 165,000 Mn(III) chelates. *In vitro* targeting to fibrin clots was resulted from applying the avidin-biotin approach using biotinylated fibrin-specific monoclonal antibodies. The fibrin-targeted Mn(III) nanobialys were positively contrast enhanced in MR images of the clots obtained at 3 T The *in vitro* release of the hydrophilic (DOX) and hydrophobic (camptothecin, CPT) drugs loaded in the nanobialys demonstrated their potential utility as theranostic agents for micro thrombi in ruptured atherosclerotic plaques [125].

Covalent attachment of the Mn(III)-$TPPS_3NH_2$ porphyrin at the surface of DOX-loaded poly(lactic acid) (PLA) led to NPs (MnP-PLA/DOX) with a diameter of 98.6 nm and a much higher r_1 (27.8 mM^{-1} s^{-1}) than the free Mn(III)-$TPPS_3NH_2$ (6.70 mM^{-1} s^{-1}), both at 0.5 T This higher r_1 results from the slower tumbling rate of the immobilized Mn (III)-porphyrin. These NPs provided selective positive contrast of the tumour in T_{1w} MRI images (7.0 T) *in vivo* upon i.v. injection of HT-29 tumour bearing nude male mice. The NPs also showed capacity for pH-sensitive tumour delivery of the DOX drug [126].

Table 3
Overview of fundamental characteristics of the MRI guided theranostic nanosystems containing Mn(III)-porphyrins covered in this section.

NPs components	Mn(III)-porphyrin	Relaxivity (mM^{-1} Mn s^{-1}), 298K[a] B_o (T)	Therapeutic modalities	Therapeutic target/animal model	Reference
Mn(III)-P/PEI/biotin-caproyl-DSPE	Mn(III)-PP	r_1 = 3.7, r_2 = 5.2 r_2/r_1 = 1.41; 1.5 T	ChT (DOX, camptothecin)	*In vitro* fibrin clots	[126]
Mn(III)-P-PLA/DOX	Mn(III)-PP	r_1 =27.8[c]; 0.5 T	ChT (DOX)	*In vivo* HT-29 tumour mice	[127]
Mn(III)PS (porphysome)	Mn(III) -porphyrin lipid	r_1 = 4.0; r_2 = 12.9 r_2/r_1 = 3.23; 7 T	PTT	No *in vitro* or *in vivo* study	[128]
DOX@PLA@Au-PEG-Mn(III)-P	Mn(III)$TPPS_3NH_2$	r_1 = 22.18[c] 0.5 T; 310 K	PTT, ChT (DOX)	*In vitro* HT-29 cells *In vivo* HT-29 tumour mice	[129]
Mn(III)P-Zr_6-SNO NMOF	Mn(III)-TCPP	r_1 = 26.9 [c] 1.2 T	PTT, ChT (NO)	*In vivo* MCF-7 tumour mice	[130]
Mn(III)P-Hf_6-FA NMOF	Mn(III)-TCPP	r_1 = 16.75 [c] 3 T	PTT/RT/ChT (FA)	*In vivo* S180 tumour BALB/c mice	[131]
HCPT@NMOF−*S* − *S*−HA	TCPP/Mn(III)-TCPP	r_1 = 31.2 [c] 1.2T	ChT/PDT/PTT	Hela cells MCF-7 tumor mice	[132]
IR825@P(PEGMA-co-APMA)-b-PMMA@TCPP/MnP	Mn(III)-TCPP	r_1 = 9.53 [c] 3 T	PTT/PDT	*In vitro* 4T1 cells *In vivo* 4T1 tumour Balb/c mice	[133]
TPD $TPPS_3$-PGL/Mn(III)-$TPPS_3$	Mn(III)-$TPPS_3$- PGL	r_1 = 20.58 0.5 T	PDT	*In vivo* HT-29 tumour mice	[134]
PCN-222 (Zr6/MnP) NMOF	Mn(III)TCPP	r_1 = 35.3; r_2 = 42.5 r_2/r_1 = 1.20; 1 T	PDT	*In vitro* 4T1 cells *In vivo* 4T1 tumour Balb/c mice	[135]
Mn(III)-TCPP NMOF	Mn(III)TCPP	r_1 = 2.65 (no GSH) ➔ 6.08(2.5 mM GSH) [c] 7 T	PDT	*In vitro* 4T1 cells *In vivo* 4T1 tumour Balb/c mice	[136]
Mn(III)$TPPS_4$-PMMA	Mn(III)$TPPS_4$	Not measured T_{2w} MRI, 7 T	SDT	*In vitro* neuroblastoma SH-SY5Y *In vivo* Mat B III breast cancer rat	[137, 138]
HMONs-MnPpIX-PEG	Mn(III)-PpIX	r_1 = 9.43[b,c]	SDT	*In vitro* 4T1 cells *In vivo* 4T1 tumour Balb/c mice	[139]
DOX/Mn-$TPPS_4$@RBCs.	Mn-$TPPS_4$	r_1 = 18.32 [c] 3 T	SDT/ChT (DOX)	*In vivo* MCF-7 tumour mice	[140]

[a] Unless specified otherwise.
[b] B_o not reported.
[c] r_2 not reported.

3.2.2.2. MRI-guided photothermal therapy. Several studies illustrated the use of Mn(III) porphyrins included in NPs for MRI-guided PTT alone or synergistically with other therapeutic modalities, such as ChT and PDT. Mn(III)-containing porphysomes (MnPS), which are liposome-like NPs (~120 nm size), were formed by self-assembly of amphiphilic Mn (III)-porphyrin lipids. Despite the high density of packed porphyrins per particle (>80 000), their relaxivities were lower than those of free porphyrin-peptide conjugates, as shown by the increased r_1 and r_2 upon detergent-mediated disruption of the supramolecular structure (r_1: 1.2 → 4.0 mM^{-1} s^{-1}; r_2: 7.0 → 12.9 mM^{-1} s^{-1} at 7 T). The relatively low liposomal $r_{1,2}$ values were related to a limitation of water access into the bilayer Mn^{III} cations, but still corresponded to *per* particle values of r_1 = 96,000 mM^{-1} s^{-1} and r_2 = 560,000 mM^{-1} s^{-1}. These MnPS systems led to positive contrast in T_{1w} MRI phantom images. Additionally, the luminescence of the Mn(III) porphyrins was quenched by the presence of the paramagnetic Mn^{3+} ion via non-radiative decay pathways and improved their photostability by suppressing their ability to generate ROS following self-destructive photochemical reactions and PDT activity. Thus, the MnPS decay occurred by a pure, efficient photothermal mode. These favourable properties give these single functional component organic NPs high potential for MRI-guided PTT [127]. Furthermore, their large aqueous core could be loaded for applications in multimodal theranostics [128].

Some theranostic Mn(III)-porphyrin NPs were developed for MRI-guided synergistic PTT and ChT. One example consists of Au nanoshells surrounding PLA NPs entrapping DOX, and binding a Mn(III)-porphyrin derivative to the Au shell surface through PEG moieties (DOX@PLA@Au-PEG-Mn(III)P NPs). The PEGylation of these NPs (diameter 123.6 nm) made them colloidally stable and provided extended circulation times in blood. The presence of Mn(III)-P chelates at the surface of the NPs led to high r_1 = 22.18 mM^{-1} s^{-1} (0.5 T). NIR light irradiation of the NPs provided an efficient *in vitro* (HT-29 cells) PTT effect and the release of DOX triggered by the high capacity of the Au nanoshell to efficiently absorb NIR light. A positive *in vivo* MRI (7.0 T) contrast effect in T_{1w} images was observed in the tumour region of HT-29 tumour-bearing nude mice upon i.v. injection of the NPs. This was used to locate the tumour site accurately and for its photothermal ablation by guided external NIR laser irradiation. These *in vivo* experiments illustrated a synergistic improvement of the therapeutic effect of the theranostic NPs and combined ChT and PTT therapies relative to their separate use (Fig. 20) [129].

A porphyrinic nanoMOF (NMOF) was obtained by hydrothermal synthesis from Zr^{4+} cations, the bridging Mn(III)-TCPP porphyrin and *S*-nitrosothiol (SNO), which was bound at the surface of the NMOF (MnP-Zr_6-SNO), for MRI-guided PTT and delivery of nitric oxide (NO). In water solutions, these NMOFs had 265.5 nm hydrodynamic size and r_1 = 26.9 mM^{-1} s^{-1} (1.2 T) due to the high water access to Mn(III)-TCPP through the MOF channels. Irradiation with NIR light initiated the photothermal effect, leading to the heat-sensitive generation of nitric oxide (NO) facilitated by SNO. In T_{1w} MRI images (3 T) a positive contrast was observed 1 h post i.v. injection of the NMOFs into MCF-7 tumour-bearing nude mice, demonstrating their accumulation in the tumour, whose growth was completely inhibited upon exposure to a NIR laser, showing their effectiveness for MRI-guided NO release and PTT synergetic therapy [130].

Hydrothermal synthesis of another porphyrinic NMOF from Mn(III)-$TPPC_4$ and a hexa-Hafnium (Hf_6) cluster, which was functionalized with folic acid (FA) at the Hf nodes, provided the MnP-Hf_6-FA NMOF. *In vitro* characterization of the NPs showed a high r_1 = 16.75 mM^{-1} s^{-1} (3 T) value, high photostability and high photothermal conversion efficiency under 808 nm laser irradiation. The NMOFs were rapidly internalized by HeLa cells, resulting in positive contrast in T_{1w} MRI upon cell uptake. *In vitro* cytotoxicity of the NMOF to Hela cells was absent before irradiation, but a large and synergistic decrease of their survival was observed upon 10 min 808 nm laser irradiation or with 4 Gy X-rays, used separately or together. The NMOFs also generated O_2 from H_2O_2 and $^1O_2$ upon X-ray irradiation, showing potential as synergistic PTT/RT/CT activators of tumours. The agent had effective tumour targeting, demonstrated by T_{1w} MRI positive contrast in subcutaneously implanted S180 tumour cells in BALB/c mice. The presence of the high-Z Hf atoms led to CT attenuation in the tumour site, which also showed photoacoustic imaging (PAI) contrast resulting from the PT properties of Mn (III)-TCPP. Therefore, this multifunctional NMOF is effective in multimodal imaging (MRI, X-ray computer tomography and PAI) guided synergistic PTT/RT/CT of tumours [131].

A different strategy to obtain multifunctional porphyrinic NMOFs is to combine free porphyrin molecules with metalloporphyrins in the same mixed-ligand MOF structure, integrating the physicochemical properties of each component to increase the diversity and versatility of conventional NMOFs. An example was recently reported by Yin et al.,

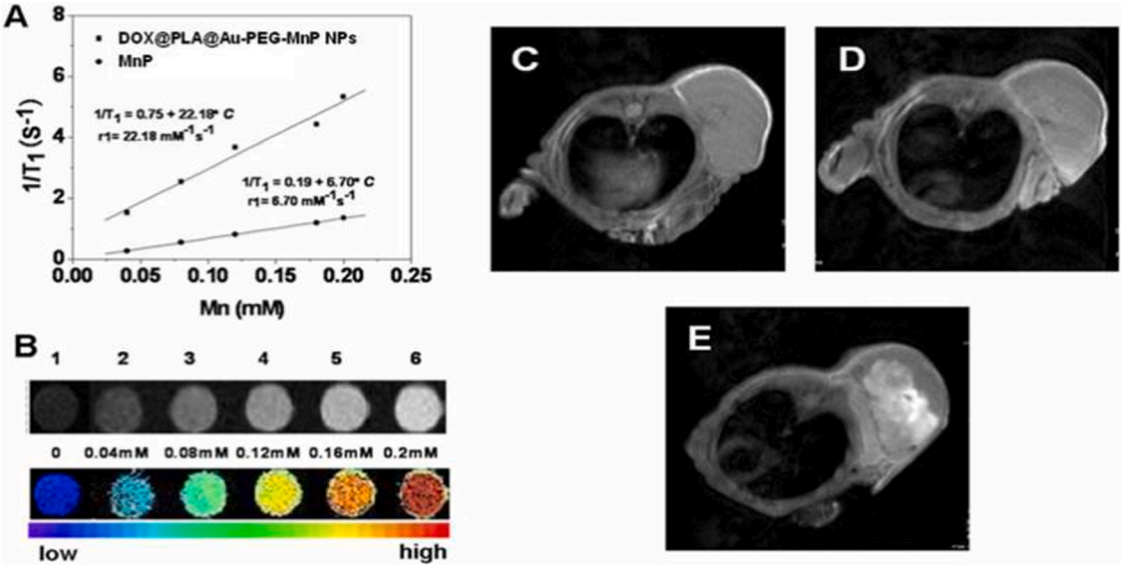

Fig. 20. (A) The T_1 relaxation rate ($1/T_1$) is proportional to the Mn^{3+} ion concentrations in DOX@PLA@Au-PEG-MnP NPs (■), and MnP (●) in water (0.5 T, 310 K); (B) T_{1w} MRI images of DOX@PLA@Au-PEG-MnP NPs phantoms as [Mn^{3+}] increases. *In vivo* MRI images of DOX@PLA@Au-PEG-MnP NPs (100 μL, 8 mg/mL): (C) before injection, (D) 30 min after injection, (E) 24 h after injection. Reproduced from Ref. [129].

who used alkali porphyrin TCPP and Mn(III)-TCPP as mixed ligands in 1:1 ratio in the presence of Zr^{4+}in one-pot hydrothermal synthesis to obtain NMOFs, integrating TCPP for fluorescence imaging (FI) and PDT and Mn(III)-TCPP for T_{1w} MRI and PTT. The NMOF was loaded with the HCPT (10-hydroxycamptothecin) drug and coated with hyaluronic acid for specific targeting to CD44 cells. The tumour-targeted redox-responsive release of HCPT from the HCPT@NMOF−$S-S$−HA platform in MCF-7 resulted from the dissociation of the $-S-S-$ bond upon reaction with GSH in the TME and was monitored by multimodal T_{1w}−MRI/OI and synergistic ChT/PDT/PTT therapy [132].

Finally, multifunctional organic nano-micelles were prepared by self-assembly of the amphiphilic block copolymer poly[(poly(ethylene glycol) methyl ether methacrylate)-co-(3-aminopropyl methacrylate)]-block-poly(methyl methacrylate) (P(PEGMA-co-APMA)-b-PMMA), with their shell crosslinked to the TCPP photosensitizer, which was used as a fluorescence indicator and PDT agent. The shell was also tagged with Mn (II) ions, undergoing spontaneous oxidation to Mn(III) and forming Mn (III)-TCPP, serving as MRI CA. The IR825 dye, incorporated non-covalently into the micelle core, provided a PT effect and PAI ability (IR825@P(PEGMA-co-APMA)-b-PMMA@$TPPC_4$/MnP NPs). These NPs (80 nm diameter) were biocompatible, with high solubility and stability in physiological conditions, an *in vitro* $r_1 = 9.53\ mM^{-1}\ s^{-1}$ (3 T), and generated singlet oxygen ($^1O_2$) with high yield after irradiation at 660 nm and high PT conversion efficiency during 808 nm laser light exposure. Their use for PTT/PDT theranostics was studied *in vitro* in 4T1 cells. Combined *in vivo* PTT/PDT synergistic anti-tumour effects were demonstrated by i.v. injection in 4T1 tumour-bearing Balb/c mice, where the NPs had a long blood circulation half-life (~3.64 h) and a high *in vivo* tumour uptake through the EPR mechanism, as shown by a tumour positive contrast of the T_{1w} MRI, fluorescence and PAI images [133].

3.2.2.3. MRI-guided photodynamic therapy. Several theranostic nanocarriers containing Mn(III) porphyrins were developed for MRI-guided PDT cancer therapy. Porphyrin dyad NPs (TPD NPs) (spherical with ~60 nm size) were initially obtained by self-aggregation of a porphyrin grafted lipid (PGL) containing the $TPPS_3A$ porphyrin, followed by covalent binding of Mn(III)-$TPPS_3$—NH_2 to the terminal carboxyl groups at the PGL NPs surface. The Mn(III)-$TPPS_3$ complex was located in the hydrophilic shell of the TPD NPs, functioning as an MRI CA, while the $TPPS_3A$ porphyrin without metal, located in the hydrophobic core, functioned as a PDT photosensitizer. A 40.1 % porphyrin/Mn(III) porphyrin ratio optimized the PDT and MRI properties of the TPD NPs.

The quenching effect of the Mn(III) porphyrin on the production of $^1O_2$ by the PGL porphyrin at the TPD NPs surface was minimized. The immobilization of Mn(III)-$TPPS_3$ on the hydrophilic shell of the NPs led to a $r_1 = 20.58\ mM^{-1}\ s^{-1}$ (0.5 T, 298 K), a four-fold increase relative to free Mn(III)$TPPS_3A$ ($5.16\ mM^{-1}\ s^{-1}$). The uptake of the NPs by HeLa tumour cells *in vitro* was by a passive mechanism. I.v. administration of the optimized TPD NPs into HT-29 tumour nude mice caused an *in vivo* positive contrast of the tumour in T_{1w} MRI images (7 T), which allowed guidance of laser light to the tumour site, causing 100 % effective PDT ablation within 7 days [134].

A porous porphyrinic NMOF was obtained by hydrothermal synthesis using Mn(III)-TCPP with Zr^{4+} ions as Zr_6 clusters, and used for MRI-guided PDT capable of overcoming the severe limitations of this technique in hypoxic tumour regions. These water stable PCN-222(Mn) NPs (300×130 nm size) had a high $r_1 = 35.3\ mM^{-1}\ s^{-1}$ (1 T) due to their good access to water in the NMOF channels resulting from the Mn^{3+} ions uniformly distributed in the open framework (3.7 nm pore size). The Mn (III)-TCPP in the NPs catalysed efficiently the conversion of H_2O_2 present in hypoxic tumours into O_2 in a catalase-like process, which could improve tumour hypoxia during the PDT process. *In vivo* T_{1w} MRI images of 4T1 tumour mice upon i.v. injection of PCN-222(Mn) induced a high positive contrast on the tumour. The injected NPs also inhibited the tumour growth effectively during laser irradiation, as a result of the efficient generation of $^1O_2$ at the tumour and the effect of MRI-guided PDT [135].

Finally, Wan et al. reported a theranostic GSH responsive Mn(III)-TCPP porphyrinic NMOF for bimodal MRI/fluorescence imaging-guided PDT of cancer. The r_1 relaxivity of the Mn(III)-TCPP NMOF in the absence of GSH, 2.65 $mM^{-1}.s^{-1}$, increased to 6.08 $mM^{-1}.s^{-1}$ in the presence of 2.5 mM GSH due to the reduction of Mn(III) to free Mn^{2+}. The high GSH concentration in the TME reduced Mn(III) to Mn(II) forming GSSG and releasing free TCPP, which simultaneously triggered positive tumour contrast in T_{1w} MRI images and $TPPC_4$ fluorescence imaging, while TCPP generated $^1O_2$ for PDT under laser irradiation. These effects were observed *in vitro* in 4T1 cells and *in vivo* using 4T1 tumour bearing BALB/c mice [136].

3.2.2.4. MRI-guided sonodynamic therapy. Several MRI-guided SDT Mn (III) porphyrin-based systems were developed, some of which are described here. A sonosensitizer associated with shockwaves (SWs), consisting of core-shell NPs of poly(methyl methacrylate) (PMMA) loaded with the tetraphenylporphine tetrasulfonic acid porphyrin ($TPPS_4$) at their surface as a sonosensitizer for SDT ($TPPS_4$-PMMA NPs), was investigated. These NPs (93 nm average hydrodynamic diameter) showed no release of $TPPS_4$ in physiological medium. The sonodynamic treatment with the NPs coupled with SWs had a cytotoxic effect reflected in a decrease of proliferation of human neuroblastoma cells after SDT and SWs, increasing the population of necrotic (16.91 %) and apoptotic (27.45 %) cells after 48 h. After 1 hour, ROS production increased 15-fold compared to free $TPPS_4$, demonstrating the enhancement of the sonosensitizing properties of $TPPS_4$ loaded to the NPs [137]. This study was continued *in vivo* by loading the $TPPS_4$-PMMA NPs for anticancer SDT theranostics with ^{64}Cu(II)$TPPS_4$ as a radiotracer in biodistribution studies using PET imaging and with Mn(III)$TPPS_4$ and a CA to evaluate their tumour accumulation by MRI. The Mn(III)-$TPPS_4$-PMMA NPs has a good tumour biodistribution in Mat B III syngeneic breast cancer rats, as monitored by PET. T_{2w} MRI (7 T) images reported a tumour volume decrease of 50 % upon treatment, confirming the SW SDT responsiveness. $TPPS_4$-PMMA NPs plus SW showed highly increased treatment efficiency relative to free $TPPS_4$ [138].

Multifunctional surface PEGylated hollow mesoporous organosilica (HMON) NPs (HMONs-MnPpIX-PEG NPs) were reported as a theranostic agent for *in vivo* MRI-guided SDT of cancer. The paramagnetic Mn(III) PpIX MRI *CA* and the organic sonosensitizer protoporphyrin (PpIX) were conjugated to 3-aminopropyltriethoxysilane (APTES) bound at the surface of HMON inner pores (Fig. 21a). The NPs (50 nm size) had a spherical mesoporous structure (Fig. 21b), which allowed $^1O_2$ generation after US irradiation, which diffused freely out from the mesopores (3.4 nm size), causing the SDT effect. These NPs had high $r_1 = 9.43\ mM^{-1}\ s^{-1}$ resulting from the high access of the paramagnetic Mn(III) ions to the solvent water molecules, which was maximized by their large surface area. The NPs were highly biocompatible, undergoing efficient endocytosis into 4T1 cancer cells, which biodegraded them using intracellular glutathione. They induced cancer-cell death *in vitro* as a result of their high SDT efficiency. *In vivo* T_{1w} MRI of 4T1 tumour-bearing BALB/c nude mice after i.v. administration of the NPs showed an increase of the tumour positive contrast and a suppression of the tumour growth after US irradiation (Fig. 21c-f) [139].

Finally, a system based on red blood cells (RBCs) was reported (DOX/Mn-$TPPS_4$@RBCs) capable of improving the SDT efficacy in hypoxic tumour regions. The RBCs were able of combining the SDT and ChT therapies upon loading with the DOX drug and the hydrophilic Mn(III) $TPPS_4$, which worked simultaneously as MRI CA and sonosensitizer. The RBCs had a high *in vitro* catalase activity, producing O_2 efficiently, promoting the RBCs rupture and improving the DOX release promoted by US irradiation. At the same time, H_2O_2 and ROS oxidized haemoglobin (Hb) to highly oxidative and cytotoxic ferryl-Hb species. Ferryl-

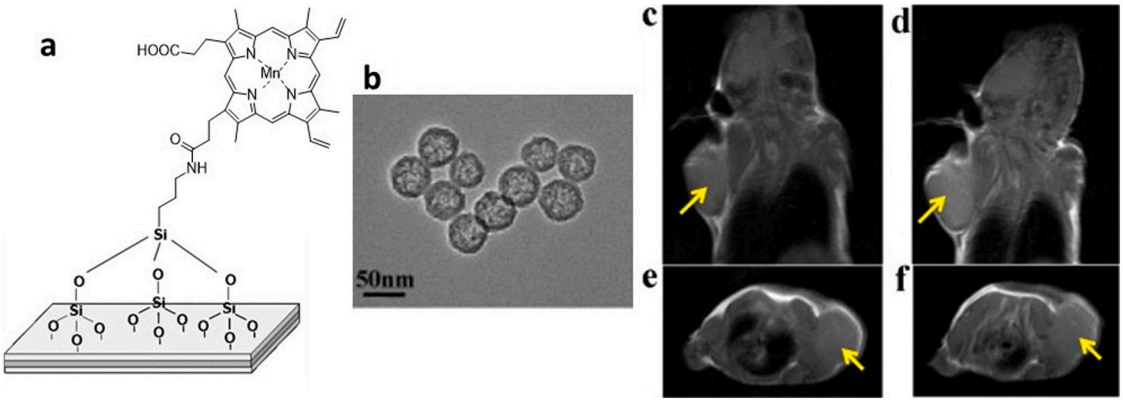

Fig. 21. a) Schematic illustration of Mn(III)PpIX anchored on the surface of PEGylated HMON NPs; b) TEM image of HMONs-MnPpIX-PEG; c-f) *In vivo* T_{1w} MRI of 4T1 tumour mice (c, axial and e, coronal) before and (d, axial and f, coronal) upon i.v. injection of HMONs-MnPpIXPEG. Adapted from Ref. [139].

Hb could diffuse more efficiently into cancer cells than ROS, due to a longer half-life, causing larger oxidative damage (Fig. 22). Fluorescence microscopy was used to verify the increased cytotoxicity of the combined RBCs/H_2O_2/US NPs in MCF-7 cells loaded with the NPs. They had a $r_1 = 18.32\ mM^{-1}\ s^{-1}$ (3 T) in water, indicative of good potential as positive MRI CAs of a tumour site. *In vivo* T_{1w} MRI and fluorescence imaging of MCF-7 tumour mice upon being *i.v.* injected with the NPs labelled with the optical probe IR783, showed that they were able to overcome tumour hypoxia and enhance the SDT efficacy in this combination therapy [140].

3.3. Mn(IV) systems

Some Mn(IV)-containing NPs for tumour theranostics by MRI are not based on MnO_2. For example, Mn(IV)-HDCL (HDCL= hexa-hydrazide clathrochelate ligand) Mn-HDCL has a 2D sheet structure, obtained by scanning tunnelling microscopy (STM). Single crystal X-ray diffraction (XRD) analysis showed that Mn(IV) is bound in the cavity of the HDCL cage, shielding it from the external environment, providing high thermal stability (as measured by thermogravimetric analysis, TGA) and good water solubility. Deep black crystalline Mn-HDCL essentially does not transmit visible light. Its UV−Vis−NIR spectrum contains a broad band absorbing in the 200 - 1000 nm range with a large extinction coefficient. It had a high photothermal conversion ability (*ca.* 71 %) in water solution upon NIR 730 nm laser irradiation, which was equivalent to solid state single walled carbon nanotubes (SWCNTs). The very low cytotoxicity of Mn-HDCL towards 4T1 cancer cells and HUVEC endothelial cells observed in normal conditions, increased very much upon 730 nm laser irradiation. The cell viability at [Mn-HDCL] = 1.0 mM decreased to 5 %, as seen by fluorescence microscopic images of 4T1 cells labelled with calcein AM and propidium iodide, which was coherent with high photothemal conversion and photothermal ablation of cells. Mn(IV)-HDCL (Mn(IV) has $S = 3/2$), with low $r_1 = 0.357\ mM^{-1}\ s^{-1}$ (0.5 T, 298 K) provided a small positive contrast in T_{1w} MRI images both *in vitro* and *in vivo* when a BALB/c mouse was i.v. injected with Mn-HDCL (0.05 mmol/kg). Mn-HDCL targeted tumours passively and the tumour margins became visible *in vivo* images. It also showed an efficient laser-triggered PTT effect *in vitro* and *in vivo*, showing potential as a tumour-targeting photothermal sensitizer [141].

4. Conclusions

Non-oxide nanoparticles utilizing manganese ions in various oxidation states [Mn(II/III/IV)] have been extensively investigated as

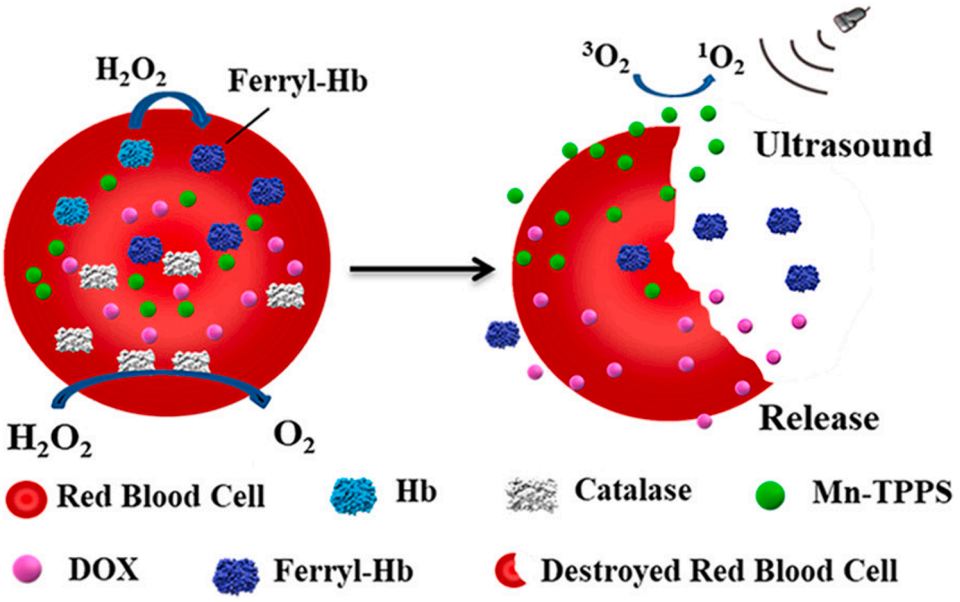

Fig. 22. Schematic representation of the mode of action of DOX/Mn-TPPS4@RBCs as an MRI-guided SDT platform Reproduced with permission from Ref. [140]. Copyright (2018) from the American Chemical Society.

alternatives to Gd(III) and high-spin Fe(III) for the design of nanosystems in T_1-weighted MRI imaging and MRI-guided theranostics. This review highlights several recent examples of these systems, including Mn(II) chelates incorporated into micelles or liposomes via hydrophobic interactions, conjugated to hydrophilic dendrimers and polysaccharides, or anchored onto inorganic NPs composed of silica, carbon, and iron oxides. Additionally, Mn(II)-based metal-organic frameworks (MOFs), Mn(III)-porphyrin systems, and a notable example of an Mn(IV)-based system were also examined.

This review has highlighted key aspects of Mn-based nanoparticles (NPs), which can be summarized as follows:

1) NPs containing Mn(II), Mn(III), or Mn(IV) ions exhibit a progressive decrease in paramagnetic relaxation efficiency. This trend is attributed to the reduction in the number of unpaired electrons across their electronic configurations, leading to lower spin values ($S = 5/2$, 2, and 3/2, respectively) and decreased effective magnetic moments (μ_{eff}) (Table 1).
2) Greater attention must be paid to safety considerations, which are important even for preclinical animal studies. Careful testing for the potential release of manganese ions should always be conducted. To mitigate the potential toxicity associated with free Mn^{2+} ions, the incorporation of chelating ligands should be prioritized. These ligands help form thermodynamically stable and kinetically inert complexes, either anchored to or encapsulated within the NPs, ensuring safer and more effective Mn-based nanosystems.
3) In this regard, porphyrin ligands are highly effective in forming strong chelates with both Mn(II) and Mn(III). The natural tendency of Mn(III)-porphyrins to accumulate in tumour tissues makes them particularly promising as MRI contrast agents for MRI-guided therapies. Additionally, their intrinsic optical properties render them valuable for theranostic applications, including photothermal therapy, photodynamic therapy, and sonodynamic therapy.
4) Optimizing the chemical structure of nanoparticles represents a crucial step towards enhancing their MRI efficacy and sensitivity. To this end, it is essential to fully understand the fundamental importance of studying relaxivity as a function of the applied magnetic field. A deeper and more systematic understanding of the relationship between r_1 and r_2 relaxation efficiencies and the structural features of NPs, such as composition, size, and shape, requires relaxivity measurements at multiple proton Larmor frequencies. Specifically, these values should be assessed at least at three different frequencies within the 20–120 MHz range (equivalent to 0.5–3 T). Given the strong dependence of relaxivity on the observation frequency, the scarcity of such data hinders the rational design and optimization of Mn-based NPs, potentially slowing their development. Furthermore, the currently reported ionic relaxivities remain well below their theoretical limits, leaving substantial room for improvement. Enhancing these values could boost the sensitivity of nanoprobes and lower detection limits in molecular MRI applications.

Despite the many improvements in the development of Mn-based MRI-guided theranostic nanosystems outlined in this review, none have yet progressed to clinical application. More broadly, only a limited number of hybrid nanotheranostic systems have reached clinical trials. This slow translation may be attributed to several challenges, including the difficulty of precisely controlling nanoparticle size, shape, and structural complexity, as well as their intricate biological interactions at the animal level, such as immune responses, toxicity, pharmacokinetics, and biodistribution. To advance these nanosystems to Phase I clinical trials, more comprehensive preclinical studies are needed using human-relevant *in vivo* models. Critical aspects that require further investigation include biodistribution, targeting efficiency (comparing targeted *vs.* non-targeted systems in tumor models), biodegradation, long-term toxicity, and elimination pathways, areas where reported data remain limited. However, even within the context of preclinical applications, substantial room for improvement remains regarding the efficacy and safety of these nanoprobes.

Funding

This manuscript is part of the project NODES which has received funding from the MUR-M4C2 1.5 of PNRR with grant agreement no ECS00000036 (M.B.). C.F.G.C.G. acknowledges the Foundation for Science and Technology (FCT), Portugal, for funding the Coimbra Chemistry Centre (UID/QUI/00313/2020, UIDP/00313/2020 and POCI-01-0145-FEDER-027996) of the University of Coimbra. L.T. acknowledges financial support from PRIN 2022 project (ID 20224B4285).

CRediT authorship contribution statement

Lorenzo Tei: Writing – review & editing, Writing – original draft, Data curation, Conceptualization. **Mauro Botta:** Writing – review & editing, Writing – original draft, Data curation, Conceptualization. **Carlos F.G.C. Geraldes:** Writing – review & editing, Writing – original draft, Data curation, Conceptualization.

Declaration of competing interest

The authors declare that they have no known competing financial interests or personal relationships that could have appeared to influence the work reported in this paper.

References

[1] T.L. Doane, C. Burda, The unique role of nanoparticles in nanomedicine: imaging, drug delivery and therapy, Chem. Soc. Rev. 41 (2011) 2885–2911, https://doi.org/10.1039/C2CS15260F.
[2] P. Sharma, S. Brown, G. Walter, S. Santra, B. Moudgil, Nanoparticles for bioimaging, Adv. Colloid Interface Sci. 123–126 (2006) 471–485, https://doi.org/10.1016/j.cis.2006.05.026.
[3] G.R. Rudramurthy, M.K. Swamy, Potential applications of engineered nanoparticles in medicine and biology: an update, J. Biol. Inorg. Chem. 23 (2018) 1185–1204, https://doi.org/10.1007/s00775-018-1600-6.
[4] N. Feliu, W.J. Parak, Developing future nanomedicines, Science 384 (2024) 385–386, https://doi.org/10.1126/science.abq3711, 6694.
[5] S.P. Rowe, M.G. Pomper, Molecular Imaging in oncology: current impact and future directions, *CA* Cancer J. Clin. 72 (2022) 333–352, https://doi.org/10.3322/caac.21713.
[6] X. Han, K. Xu, O. Taratula, K. Farsad, Applications of nanoparticles in biomedical imaging, Nanoscale 11 (2019) 799–819, https://doi.org/10.1039/C8NR07769J.
[7] S.K. Nune, P. Gunda, P.K. Thallapally, Y.-Y. Lin, M.L. Forrest, C.J. Berkland, Nanoparticles for Biomedical imaging, Expert Opin. Drug Deliv. 6 (2009) 1175–1194, https://doi.org/10.1517/17425240903229031.
[8] D. Kim, J. Kim, Y. Il Park, N. Lee, T. Hyeon, Recent development of inorganic nanoparticles for biomedical imaging, ACS Cent. Sci. 4 (2018) 324–336, https://doi.org/10.1021/acscentsci.7b00574.
[9] F. Chen, E.B. Ehlerding, W. Cai, Theranostic nanoparticles, J. Nucl. Med. 55 (2014) 1919–1922, https://doi.org/10.2967/jnumed.114.146019.
[10] J. Lohrke, T. Frenzel, J. Endrikat, F.C. Alves, T.M. Grist, M. Law, J.M. Lee, T. Leiner, K.C. Li, K. Nikolaou, et al., 25 Years of contrast-enhanced MRI: developments, current challenges and future perspectives, Adv. Ther. 33 (2016) 1–28, https://doi.org/10.1007/s12325-015-0275-4.
[11] J. Wahsner, E.M. Gale, A. Rodríguez-Rodríguez, P. Caravan, Chemistry of MRI contrast agents: current challenges and new frontiers, Chem. Rev. 119 (2019) 957–1057, https://doi.org/10.1021/acs.chemrev.8b00363.
[12] S. Aime, M. Botta, E. Terreno, Gd(III)-based contrast agents for MRI, Adv. Inorg. Chem. 57 (2005) 173–237, https://doi.org/10.1016/S0898-8838(05)57004-1.
[13] A.E. Merbach, L. Helm, É. Tóth, The Chemistry of Contrast Agents in Medical Magnetic Resonance Imaging, (Second), John Wiley & Sons Ltd, Chichester (UK), 2013, https://doi.org/10.1002/9781118503652.
[14] H. Li, T.J. Meade, Molecular Magnetic resonance imaging with Gd(III)-based contrast agents: challenges and key advances, J. Am. Chem. Soc. 141 (2019) 17025–17041, https://doi.org/10.1021/jacs.9b09149.
[15] M. Botta, L. Tei, Relaxivity enhancement in macromolecular and nanosized Gd^{III}-based MRI contrast agents, Eur. J. Inorg. Chem. 2012 (2012) 1945–1960, https://doi.org/10.1002/ejic.201101305.
[16] A.J.L. Villaraza, A. Bumb, M.W. Brechbiel, Macromolecules, dendrimers, and nanomaterials in Magnetic resonance imaging: the interplay between size, function, and pharmacokinetics, Chem. Rev. 110 (2010) 2921–2959, https://doi.org/10.1021/cr900232t.

[17] G.J. Soufi, A. Hekmatnia, S. Iravani, R.S. Varma, Nanoscale contrast agents for magnetic resonance imaging: a review, ACS Appl. Nano Mater. 5 (2022) 10151–10166, https://doi.org/10.1021/acsanm.2c03297.
[18] D. Ni, W. Bu, E.B. Ehlerding, W. Cai, J. Shi, Engineering of inorganic nanoparticles as magnetic resonance imaging contrast agents, Chem. Soc. Rev. 46 (2017) 7438–7468, https://doi.org/10.1039/C7CS00316A.
[19] R. Du, Z. Zhao, J. Cui, Y. Li, Manganese-based nanotheranostics for Magnetic resonance imaging-mediated precise cancer management, Int. J. Nanomed. 18 (2023) 6077–6099, https://doi.org/10.2147/IJN.S426311.
[20] R.R. Zairov, B.S. Akhmadeev, S.V. Fedorenko, A.R. Mustafina, Recent progress in design and surface modification of manganese nanoparticles for MRI contrasting and therapy, Chem. Eng. J. 459 (2023) 141640, https://doi.org/10.1016/j.cej.2023.141640.
[21] L. Zhang, S. Roy, B. Guo, The role of manganese-based MRI contrast agents for cancer theranostics: where do we stand in 2025? Theranostics 15 (2025) 4147–4174, https://doi.org/10.7150/thno.108705.
[22] B. Drahoš, I. Lukeš, É. Tóth, Manganese(II) complexes as potential contrast agents for MRI, Eur. J. Inorg. Chem. 12 (2012) 1975–1986, https://doi.org/10.1002/ejic.201101336.
[23] M. Botta, F. Carniato, D. Esteban-Gomez, C. Platas-Iglesias, L. Tei, Mn(II) compounds as an alternative to Gd-based MRI probes, Future Med. Chem. 11 (2019) 1461–1483, https://doi.org/10.4155/fmc-2018-0608.
[24] S.L. O'Neal, W. Zheng, Manganese toxicity upon overexposure: a decade in review, Curr. Envir. Health Rpt. 2 (2015) 315–328, https://doi.org/10.1007/s40572-015-0056-x.
[25] D.S. Avila, R.L. Puntel, M. Aschner, Manganese in health and disease, in: A. Sigel, H. Sigel, R. Sigel (Eds.), Interrelations Between Essential Metal Ions and Human Diseases. Metal Ions in Life Sciences, Vol 13, Springer, Dordrecht, 2013, https://doi.org/10.1007/978-94-007-7500-8_7.
[26] R.G. Lucchini, C.J. Martin, B.C. Doney, From manganism to manganese-induced parkinsonism: a conceptual model based on the evolution of exposure, Neuromol. Med. 11 (2009) 311–321, https://doi.org/10.1007/s12017-009-8108-8.
[27] B.Y.W. Hsu, G. Kirby, A. Tan, A.M. Seifalian, X. Li, J. Wang, Relaxivity and toxicological properties of manganese oxide nanoparticles for MRI applications, RSC Adv. 6 (2019) 45462–45474, https://doi.org/10.1039/C6RA04421B.
[28] R. Antwi-Baah, Y. Wang, X. Chen, Y. Kui, Metal-based nanoparticle Magnetic resonance imaging contrast agents: classifications, issues, and countermeasures toward their clinical translation, Adv. Mater. Interfaces, 9 (2022) 2101710, https://doi.org/10.1002/admi.202101710.
[29] X. Cai, Q. Zhu, Y. Zeng, Q. Zeng, X. Chen, Y. Zhan, Manganese oxide nanoparticles as MRI contrast agents in tumour multimodal imaging and therapy, Int. J. Nanomed. 14 (2019) 8321–8344, https://doi.org/10.2147/IJN.S218085.
[30] C.F.G.C. Geraldes, Manganese oxide nanoparticles for MRI-based multimodal imaging and theranostics, Molecules 29 (2024) 5591, https://doi.org/10.3390/molecules29235591.
[31] P. Jain, A.K. Jangid, D. Pooja, H. Kulhari, Design of manganese-based nanomaterials for pharmaceutical and biomedical applications, J. Mater. Chem. B 12 (2024) 577–608, https://doi.org/10.1039/D3TB00779K.
[32] P. Caravan, C.T. Farrar, L. Frullano, R. Uppal, Influence of molecular parameters and increasing magnetic field strength on relaxivity of gadolinium- and manganese-based T_1 contrast agents, Contrast Media Mol. Imaging 4 (2009) 89–100, https://doi.org/10.1002/cmmi.267.
[33] S. Aime, M. Botta, D. Esteban-Gómez, C. Platas-Iglesias, Characterisation of magnetic resonance imaging (MRI) contrast agents using NMR relaxometry, Mol. Phys. 117 (2019) 898–909, https://doi.org/10.1080/00268976.2018.1516898.
[34] S.H. Koenig, Classes of hydration sites at protein-water interfaces: the source of contrast in magnetic resonance imaging, Biophys. J. 69 (1995) 593–603, https://doi.org/10.1016/S0006-3495(95)79933-7.
[35] P. Caravan, J.J. Ellison, T.J. McMurry, R.B. Lauffer, Gadolinium(III) chelates as MRI contrast agents: structure, dynamics, and applications, Chem. Rev. 99 (1999) 2293–2352, https://doi.org/10.1021/cr980440x.
[36] L. Vander Elst, A. Roch, P. Gillis, S. Laurent, F. Botteman, J.W.M. Bulte, R. N. Muller, Dy-DTPA derivatives as relaxation agents for very high field MRI: the beneficial effect of slow water exchange on the transverse relaxivities, Magn. Reson. Med. 47 (2002) 1121–1130, https://doi.org/10.1002/mrm.10163.
[37] B. Misselwitz, B.H. Schmitt-Willich, W. Ebert, T. Frenzel, H.J. Weinmann, Pharmacokinetics of Gadomer-17, a new dendritic magnetic resonance contrast agent, MAGMA 12 (2001) 128–134, https://doi.org/10.1007/BF02668094.
[38] Y. Gossuin, P. Gillis, A. Hocq, Q.L. Vuong, A. Roch, Magnetic resonance relaxation properties of superparamagnetic particles, Wiley Interdiscip. Rev. Nanomed. Nanobiotechnol. 1 (3) (2009) 299–310, https://doi.org/10.1002/wnan.36.
[39] G. Jung, W. Heindel, T. Krahe, H. Kugel, C. Walter, R. Fischbach, H. Klaus, K. Lackner, Influence of the hepatobiliary contrast agent Mangafodipir trisodium (Mn-DPDP) on the imaging properties of abdominal organs, Magn. Reson. Imaging 16 (1998) 925–931, https://doi.org/10.1016/S0730-725X(98)00086-1.
[40] E.M. Gale, H.-Y. Wey, I. Ramsay, Y.-F. Yen, D.E. Sosnovik, P. Caravan, A manganese-based alternative to gadolinium: contrast-enhanced MR angiography, excretion, pharmacokinetics, and metabolism, Radiology 286 (2018) 865–872, https://doi.org/10.1148/radiol.2017170977.
[41] D. Ndiaye, P. Cieslik, H. Wadepohl, A. Pallier, S. Meme, P. Comba, É. Tóth, Mn^{2+} bispidine complex combining exceptional stability, inertness, and MRI efficiency, J. Am. Chem. Soc. 144 (2022) 22212–22220, https://doi.org/10.1021/jacs.2c10108.
[42] I. Bertini, C. Luchinat, G. Parigi, E. Ravera, NMR of Paramagnetic Molecules. Applications to Metallobiomolecules and Models, 2nd Edition, 2, Elsevier Science, 2016. ISBN: 9780444634368.
[43] K.D.W. Vollett, D.A. Szulc, H.- L.M. Cheng, A Manganese porphyrin platform for the design and synthesis of molecular and targeted MRI contrast agents, Int. J. Mol. Sci. 24 (2023) 9532, https://doi.org/10.3390/ijms24119532.
[44] C.F.G.C. Geraldes, M.M.C.A. Castro, J.A. Peters, Mn(III) porphyrins as potential MRI contrast agents for diagnosis and MRI-guided therapy, Coord. Chem. Rev. 445 (2021) 214069, https://doi.org/10.1016/j.ccr.2021.214069.
[45] L. García-Hevia, M. Bañobre-López, J. Gallo, Recent progress on manganese-based nanostructures as responsive MRI contrast agents, Chem. Eur. J. 25 (2019) 431–441, https://doi.org/10.1002/chem.201802851.
[46] A. Sharma, L. Feng, D.F. Muresanu, S. Sahib, Z.R. Tiane, J.V. Lafuente, A. D. Buzoianu, R.J. Castellani, A. Nozari, L. Wiklund, H.S. Sharma, Manganese nanoparticles induce blood-brain barrier disruption, cerebral blood flow reduction, edema formation and brain pathology associated with cognitive and motor dysfunctions, Prog. Brain Res. 265 (2021) 385–406, https://doi.org/10.1016/bs.pbr.2021.06.015.
[47] M. Parvaneh, S. Samaneh, F. Hashemi, Ale-Ebrahim. Tau folding and cytotoxicity of neuroblastoma cells in the presence of manganese oxide nanoparticles: biophysical, molecular dynamics, cellular, and molecular studies, Int. J. Biol. Macromol. 125 (2018) 674–682, https://doi.org/10.1016/j.ijbiomac.2018.11.191.
[48] J.A. Roth, B. Ganapathy, A.J. Ghio, Manganese-induced toxicity in normal and human B lymphocyte 655 cell lines containing a homozygous mutation in parkin, Toxicol. *In Vitro* 26 (2012) 1143–1149, https://doi.org/10.1016/j.tiv.2012.07.005.
[49] D. Ding, J. Roth, R. Salvi, Manganese is toxic to spiral ganglion neurons and hair cells *in vitro*, Neurotoxicology 32 (2011) 233–241, https://doi.org/10.1016/j.neuro.2010.12.003.
[50] R. Uzal-Varela, F. Pérez-Fernández, L. Valencia, A. Rodríguez-Rodríguez, C. Platas-Iglesias, P. Caravan, D. Esteban-Gómez, Thermodynamic stability of Mn (II) complexes with aminocarboxylate ligands analyzed using structural descriptors, Inorg. Chem. 61 (2022) 14173–14186, https://doi.org/10.1021/acs.inorgchem.2c02364.
[51] L. Lattuada, A. Barge, G. Cravotto, G.B. Giovenzana, L. Tei, The synthesis and application of polyamino polycarboxylic bifunctional chelating agents, Chem. Soc. Rev. 40 (2011) 3019–3049, https://doi.org/10.1039/c0cs00199f.
[52] A. Accardo, D. Tesauro, L. Aloj, C. Pedone, G. Morelli, Supramolecular aggregates containing lipophilic Gd(III) complexes as contrast agents in MRI, Coord. Chem. Rev. 253 (2009) 2193–2213. doi:10.1016/j.ccr.2009.01.015.
[53] S. Langereis, T. Geelen, H. Grull, G.J. Strijkers, K. Nicolay, Paramagnetic liposomes for molecular MRI and MRI-guided drug delivery, NMR Biomed. 26 (2013) 728–744, https://doi.org/10.1002/nbm.2971.
[54] M. Filippi, D. Remotti, M. Botta, E. Terreno, L. Tei, GdDOTAGA(C18)2: an efficient amphiphilic Gd(III) chelate for the preparation of self-assembled high relaxivity MRI nanoprobes, Chem. Commun. 51 (2015) 17455–17458, https://doi.org/10.1039/c5cc06032j.
[55] M. Elsabahy, G.S. Heo, S.M. Lim, G. Sun, K.L. Wooley, Polymeric nanostructures for imaging and therapy, Chem. Rev. 115 (2015) 10967–11011, https://doi.org/10.1021/acs.chemrev.5b00135.
[56] M. Filippi, J. Martinelli, G. Mulas, M. Ferraretto, T. Eline, M. Botta, L. Tei, E. Terreno, Dendrimersomes: a new vesicular nano-platform for MR-molecular imaging applications, Chem. Commun. 50 (2014) 3453–3456, https://doi.org/10.1039/c3cc49584a.
[57] E. Terreno, D. Delli Castelli, C. Cabella, W. Dastru, A. Sanino, J. Stancanello, L. Tei, S. Aime, Paramagnetic liposomes as innovative contrast agents for magnetic resonance (MR) molecular imaging applications, Chem. Biodivers. 5 (2008) 1901–1912, https://doi.org/10.1002/cbdv.200890178.
[58] C. Wu, D. Li, L. Yang, B. Lin, H. Zhang, Y. Xu, Z. Cheng, C. Xia, Q. Gong, B. Song, H. Ai, Multivalent manganese complex decorated amphiphilic dextran micelles as sensitive MRI probes, J. Mater. Chem. B 3 (2015) 1470–1473, https://doi.org/10.1039/C4TB02036G.
[59] J.M. Keca, J. Chen, M. Overchuk, N. Muhanna, C.M. MacLaughlin, C.S. Jin, W. D. Foltz, J.C. Irish, G. Zheng, Nanotexaphyrin: one-pot synthesis of a Manganese texaphyrin-phospholipid nanoparticle for Magnetic resonance imaging, Angew. Chem. Int. Ed. 55 (2016) 6187–6191, https://doi.org/10.1002/anie.201600234.
[60] G.A. Rolla, V. De Biasio, G.B. Giovenzana, M. Botta, L. Tei, Supramolecular assemblies based on amphiphilic Mn2+-complexes as high relaxivity MRI probes, Dalton Trans. 47 (2018) 10660–10670, https://doi.org/10.1039/c8dt01250d.
[61] G.A. Rolla, C. Platas-Iglesias, M. Botta, L. Tei, L. Helm, 1H and 17O NMR relaxometric and computational study on macrocyclic Mn(II) complexes, Inorg. Chem. 52 (2013) 3268–3279, https://doi.org/10.1021/ic302785m.
[62] Z. Garda, A. Forgács, F.K. Kálmán, S. Timári, I. Tóth, Z. Baranyai, L. Tei, Z. Kovács, G. Tircsó, Physico-chemical properties of MnII complexes formed with cis- and trans-DO2A: thermodynamic, electrochemical and kinetic studies, J. Inorg. Biochem. 163 (2016) 206–213, https://doi.org/10.1016/j.jinorgbio.2016.07.018.
[63] G. Mulas, G.A. Rolla, C.F.G.C. Geraldes, L.W.E. Starmans, M. Botta, E. Terreno, L. Tei, Mn(II)-based lipidic nanovesicles as high-efficiency MRI probes, ACS Appl. Bio Mater. 3 (2020) 2401–2409, https://doi.org/10.1021/acsabm.0c00138.
[64] J. Wang, J. Wang, P. Ding, W. Zhou, Y. Li, M. Drechsler, X. Guo, M.A. Cohen Stuart, A supramolecular crosslinker to give salt-resistant polyion complex micelles and improved MRI contrast agents, Angew. Chem. Int. Ed. 57 (2018) 12680–12684, https://doi.org/10.1002/anie.201805707.
[65] X. Liu, S. Fu, C. Xia, M. Li, Z. Cai, C. Wu, F. Lu, J. Zhu, B. Song, Q. Gongde, H. Ai, PEGylated amphiphilic polymeric manganese(II) complexes as magnetic resonance angiographic agents, J. Mater. Chem. B 10 (2022) 2204–2214, https://doi.org/10.1039/D2TB00089J.

[66] Y. Jiang, Z. Cai, S. Fu, H. Gu, X. Fu, J. Zhu, Y. Ke, H. Jiang, W. Cao, C. Wu, C. Xia, S. Lui, B. Song, Q. Gong, H. Ai, Relaxivity enhancement of hybrid micelles via modulation of water coordination numbers for magnetic resonance lymphography, Nano Lett. 23 (2023) 8505–8514, https://doi.org/10.1021/acs.nano.

[67] K. Chen, Z. Cai, Y. Cao, L. Jiang, Y. Jiang, H. Gu, S. Fu, C. Xia, S. Lui, Q. Gong, B. Song, H. Ai, Kinetically inert manganese (II)-based hybrid micellar complexes for magnetic resonance imaging of lymph node metastasis, Regener. Biomater. 10 (2023) rbad053, https://doi.org/10.1093/rb/rbad053.

[68] E.C. Wiener, M.W. Brechbiel, H. Brothers, R.L. Magin, O.A. Gansow, D. A. Tomalia, P.C. Lauterbur, Dendrimer-based metal chelates: a new class of magnetic resonance imaging contrast agents, Magn. Reson. Med. 31 (1994) 1–8, https://doi.org/10.1002/mrm.1910310102.

[69] T.T. McMahon, J.W.M. Bulte, Two decades of dendrimers as versatile MRI agents: a tale with and without metals, Wiley Interdiscip. Rev. Nanomed. Nanobiotechnol. 10 (2018) e1496, https://doi.org/10.1002/wnan.1496.

[70] L. Tei, G. Gugliotta, G. Gambino, M. Fekete, M. Botta, Developing high field MRI contrast agents by tuning the rotational dynamics: bisaqua GdAAZTA-based dendrimers, Isr. J. Chem. 57 (2017) 887–895, https://doi.org/10.1002/ijch.201700041.

[71] M. Tan, Z. Ye, E.-K. Jeong, X. Wu, D.L. Parker, Z.-R. Lu, Synthesis and evaluation of nanoglobular macrocyclic Mn(II) chelate conjugates as non-gadolinium(III) MRI contrast agents, Bioconjugate Chem. 22 (2011) 931–937, https://doi.org/10.1021/bc100573t.

[72] M. Tan, X. Wu, E.-K. Jeong, Q. Chen, D.L. Parker, Z.-R. Lu, An effective targeted nanoglobular manganese(II) chelate conjugate for magnetic resonance molecular imaging of tumour extracellular matrix, Mol. Pharm. 7 (2010) 936–943, https://doi.org/10.1021/mp100054m.

[73] R. Wang, Y. Luo, S. Yang, J. Lin, D. Gao, Y. Zhao, J. Liu, X. Shi, X. Wang, Hyaluronic acid-modified manganese-chelated dendrimer-entrapped gold nanoparticles for the targeted CT/MR dual-mode imaging of hepatocellular carcinoma, Sci. Rep. 6 (2016) 33844, https://doi.org/10.1038/srep33844.

[74] C. Sun, Z. Yang, P. Wu, X. Luo, K. Liu, B. Wang, H. Lin, J. Gao, Multinuclear Mn (II) united-DOTA complexes with enhanced inertness and high MRI contrast ability, Cell Rep. Phys. Sci. 3 (2022) 100920, https://doi.org/10.1016/j.xcrp.2022.100920.

[75] Y. Shen, X. Li, H. Huang, Y. Lan, L. Gan, J. Huang, Embedding Mn2+ in polymer coating on rod-like cellulose nanocrystal to integrate MRI and photothermal function, Carbohydr. Polym. 297 (2022) 120061, https://doi.org/10.1016/j.carbpol.2022.120061.

[76] Y. Shen, X. Li, Y. Lan, M. Zu, X. Liu, H. Huang, N. Zhou, R. Duan, L. Gan, J. Huang, Enhancing magnetic resonance imaging of bio-based nano-contrast via anchoring manganese on rod-shaped cellulose nanocrystals, Cellulose 28 (2021) 2905–2916, https://doi.org/10.1007/s10570-021-03693-1.

[77] X. Wang, L. Xu, Z. Ren, M. Fan, J. Zhang, H. Qi, M. Xu, A novel manganese chelated macromolecular MRI contrast agent based on O-carboxymethyl chitosan derivatives, Coll. Surf. B: Biointerfaces 183 (2019) 110452, https://doi.org/10.1016/j.colsurfb.2019.110452.

[78] K.D. Addisu, B.Z. Hailemeskel, S.L. Mekuria, A.T. Andrgie, Y.-C. Lin, H.-C. Tsai, Bioinspired, Manganese-chelated alginate–Polydopamine nanomaterials for efficient *in vivo* T1-weighted Magnetic resonance imaging, ACS Appl. Mater. Interf. 10 (2018) 5147–5160, https://doi.org/10.1021/acsami.7b13396.

[79] F. Carniato, M. Ricci, L. Tei, F. Garello, C. Furlan, E. Terreno, E. Ravera, G. Parigi, C. Luchinat, M. Botta, Novel nanogels loaded with Mn(II) chelates as effective and biologically stable MRI probes, Small (2023) 2302868, https://doi.org/10.1002/smll.202302868.

[80] F. Carniato, L. Tei, M. Botta, Gd-based mesoporous silica nanoparticles as MRI probes, Eur. J. Inorg. Chem. 46 (2018) 4936–4954, https://doi.org/10.1002/ejic.201801039.

[81] M. Palmai, A. Petho, L.N. Nagy, S. Klebert, Z. May, J. Mihaly, A. Wacha, K. Jemnitz, Z. Veres, I. Horvath, K. Szigeti, D. Mathe, Z. Varga, Direct immobilization of manganese chelates on silica nanospheres for MRI applications, J. Colloid Interface Sci. 498 (2017) 298–305, https://doi.org/10.1016/j.jcis.2017.03.053.

[82] D. Lalli, G. Ferrauto, E. Terreno, F. Carniato, M. Botta, Mn(II)-conjugated silica nanoparticles as potential MRI probes, J. Mater. Chem. B 9 (2021) 8994–9004, https://doi.org/10.1039/D1TB01600H.

[83] R. Mallik, M. Saha, C. Mukherjee, Porous silica nanospheres with a confined mono(aquated) Mn(II)-complex: a potential T1–T2 dual contrast agent for Magnetic Resonance Imaging, ACS Appl. Bio Mater. 4 (2021) 8356–8367, https://doi.org/10.1021/acsabm.1c00937.

[84] W. Hou, T.B. Toh, L.N. Abdullah, T.W.Z. Yvonne, K.J. Lee, I. Guenther, E.K.-H. Chow, Nanodiamond–manganese dual mode MRI contrast agents for enhanced liver tumour detection nanomedicine: nanotech, Biol. Med. 13 (2017) 783–793, https://doi.org/10.1016/j.nano.2016.12.013.

[85] R. Qin, S. Li, Y. Qiu, Y. Feng, Y. Liu, D. Ding, L. Xu, X. Ma, W. Sun, H. Chen, Carbonized paramagnetic complexes of Mn(II) as contrast agents for precise magnetic resonance imaging of sub-millimeter-sized orthotopic tumours, Nat. Commun. 13 (2022) 1938, https://doi.org/10.1038/s41467-022-29586-w.

[86] X. Huang, Z. Wang, S. Li, S. Lin, L. Zhang, Z. Meng, X. Zhang, S.-K. Sun, Non-invasive diagnosis of acute kidney injury using Mn-doped carbon dots-based magnetic resonance imaging, Biomater. Sci. 11 (2023) 4289–4297, https://doi.org/10.1039/d2bm02134j.

[87] C. Wu, T. Chen, L. Deng, Q. Xia, C. Chen, M. Lan, Y. Pu, H. Tang, Y. Xu, J. Zhu, C. Xu, C. Shena, X. Zhang, Mn(II) chelate-coated superparamagnetic iron oxide nanocrystals as high-efficiency magnetic resonance imaging contrast agents, Nanoscale Adv. 2 (2020) 2752–2757, https://doi.org/10.1039/D0NA00117A.

[88] C. Ye, E.-K. Jeong, X. Wu, M. Tan, S. Yin, Z.-R. Lu, Polydisulfide manganese(II) complexes as non-gadolinium biodegradable macromolecular MRI contrast agents, J. Magn. Res. Imaging 35 (2012) 737–744, https://doi.org/10.1002/jmri.22848.

[89] S. Fu, M. Rizwan Younis, Z. Cai, L. Liu, H. Gu, G. Ni, S. Lui, H. Ai, B. Song, M. Wu, One-pot fabrication of kinetically inert ultrasmall manganese(II) chelate-backboned polymer contrast agents for high-performance magnetic resonance imaging, Nano Lett. 24 (2024) 14252–14262, https://doi.org/10.1021/acs.nanolett.4c03804.

[90] W.-L. Lu, Y.-Q. Lan, K.-J. Xiao, Q.-M. Xu, L.-L. Qu, Q.-Y. Chen, T. Huang, J. Gao, Y. Zhao, BODIPY-Mn nanoassemblies for accurate MRI and phototherapy of hypoxic cancer, J. Mater. Chem. B 5 (2017) 1275–1283, https://doi.org/10.1039/C6TB02575G.

[91] X.-J. Tang, J. Wu, B.-l. Lin, S. Cui, H.-M. Liu, R.-T. Yu, X.-D. Shen, T.-W. Wang, W. Xia, Near-infrared light-activated red-emitting upconverting nanoplatform for T1-weighted magnetic resonance imaging and photodynamic therapy, Acta Biomater. 74 (2018) 360–373, https://doi.org/10.1016/j.actbio.2018.05.017.

[92] D. An, X. Wu, Y. Gong, W. Li, G. Dai, X. Lu, L. Yu, W. Ren, M. Qiu, J. Shu, Manganese-functionalized MXene theranostic nanoplatform for MRI-guided synergetic photothermal/chemodynamic therapy of cancer, Nanophotonics 11 (2022) 5177–5188, https://doi.org/10.1515/nanoph-2022-0533.

[93] P. Galiyeva, H. Rinnert, S. Bouguet-Bonnet, S. Leclerc, L. Balan, H. Alem, S. Blanchard, J. Jasniewski, G. Medjahdi, B. Uralbekov, R. Schneider, Mn-doped quinary Ag-In-Ga-Zn-S quantum dots for dual-modal imaging, ACS Omega 6 (2021) 33100–33110, https://doi.org/10.1021/acsomega.1c05441.

[94] M. Peller, A. Lanza, S. Wuttke, MRI-active metal-organic frameworks: concepts for the translation from lab to clinic. 4 (2021) 2100067. https://doi.org/10.1002/adtp.202100067.

[95] Y. Liu, T. Jiang, Z. Liu, Metal-organic frameworks for bioimaging: strategies and challenges, Nanotheranostics 6 (2022) 143–160, https://doi.org/10.7150/ntno.63458.

[96] M. Peller, K. Boll, A. Lanza, S. Wuttke, Metal–organic framework nanoparticles for magnetic resonance imaging, Inorg. Chem. Front. 5 (2018) 1760–1779, https://doi.org/10.1039/C8QI00149A.

[97] M.L. Kathryn, W.J.R. Taylor, W. Lin, Manganese-based nanoscale metal-organic frameworks for Magnetic resonance imaging, J. Am. Chem. Soc. 130 (2008) 14358–14359, https://doi.org/10.1021/ja803777x.

[98] L. Qin, Z.-Y. Sun, L. Cheng, S.-W. Liu, J.-X. Pang, L.-M. Xia, W.-H. Chen, Z. Cheng, J.-X. Chen, Zwitterionic manganese and gadolinium metal-organic frameworks as efficient contrast agents for *in vivo* magnetic resonance imaging, ACS Appl. Mater. Interfaces 9 (2017) 41378–41386, https://doi.org/10.1021/acsami.7b09608.

[99] N. Iki, R. Nakane, A. Masuya-Suzuki, Y. Ozawa, T. Maruoka, M. Iiyama, A. Sumiyoshi, I. Aoki, MRI contrasting agent based on Mn-MOF-74 nanoparticles with coordinatively unsaturated sites, Mol. Imag. Biol. 25 (2023) 968–976, https://doi.org/10.1007/s11307-023-01801-0.

[100] Y. Wu, L. Xu, J. Qian, L. Shi, Y. Su, Y. Wang, D. Li, X. Zhu, Methotrexate–Mn2+ based nanoscale coordination polymers as a theranostic nanoplatform for MRI guided chemotherapy, Biomater. Sci. 8 (2020) 712–719, https://doi.org/10.1039/c9bm01584a.

[101] S. Yu, X. Huang, C. Xu, L. Xu, Y. Sun, Q. Shen, B. Wang, H. Zhu, W. Lin, Q. Hu, Fabrication of metal-organic framework Mn-PBC for theranostic application, J. Solid State Chem. 313 (2022) 123349, https://doi.org/10.1016/j.jssc.2022.123349.

[102] L. Hang, M. Li, Y. Zhang, W. Li, L. Fang, Y. Chen, C. Zhou, H. Qu, L. Shao, G. Jiang, Mn(II) optimized sono/chemodynamic effect of porphyrin-metal–organic framework nanosheets for MRI-guided colon cancer therapy and metastasis suppression, Small 20 (15) (2024) 2306364, https://doi.org/10.1002/smll.202306364.

[103] P. Geng, Y. Li, D.K. Macharia, X. Ren, R. Meng, W. Wang, H. Lan, S. Xiao, One stone, three birds: design and synthesis of “all-in-one” nanoscale Mn-porphyrin coordination polymers for magnetic resonance imaging-guided synergistic photodynamic-sonodynamic therapy, J. Colloid. Interf. Sci. 660 (2024) 1021–1029, https://doi.org/10.1016/j.jcis.2024.01.157.

[104] V. Dahanayake, C. Pornrungroj, M. Pablico-Lansigan, W.J. Hickling, T. Lyons, D. Lah, Y. Lee, E. Parasido, J.A. Bertke, C. Albanese, E. Van Keuren, S.L. Stoll, Paramagnetic clusters of $Mn_3(O_2CCH_3)_6(Bpy)_2$ in polyacrylamide nanobeads as a new design approach to a T1–T2 multimodal Magnetic resonance imaging contrast agent, ACS Appl. Mater. Interfaces 11 (2019) 18153–18164, https://doi.org/10.1021/acsami.9b03216.

[105] B.S. Akhmadeev, I.R. Nizameev, K.V. Kholin, A.D. Voloshina, T.P. Gerasimova, A. T. Gubaidullin, M.K. Kadirov, I.E. Ismaev, K.A. Brylev, R.R. Zairov, A. R. Mustafina, Molecular and nano-structural optimization of nanoparticulate Mn^{2+}-hexarhenium cluster complexes for optimal balance of high T1- and T2-weighted contrast ability with low hemoagglutination and cytotoxicity, Pharmaceutics 14 (2022) 1508, https://doi.org/10.3390/pharmaceutics14071508.

[106] Q. Zou, R. Tang, H.-X. Zhao, J. Jiang, J. Li, Y.-Y. Fu, Hyaluronic acid-assisted facile synthesis of MnWO4 single-nanoparticle for efficient tri-modal imaging and liver-renal structure display, ACS Appl. Nano Mater. 1 (2018) 101–110, https://doi.org/10.1021/acsanm.7b00047.

[107] F. Carniato, K. Thangavel, L. Tei, M. Botta, Structure and dynamics of the hydration shells of citrate-coated GdF_3 nanoparticles, J. Mater. Chem. B 1 (2013) 2442–2446, https://doi.org/10.1039/c3tb20174k.

[108] N. Halttunen, F. Lerouge, F. Chaput, M. Vandamme, S. Karpati, S. Si-Mohamed, M. Sigovan, L. Boussel, E. Chereul, P. Douek, S. Parola, Hybrid Nano-GdF_3 contrast media allows pre-clinical *in vivo* element-specific K-edge imaging and quantification, Sci. Rep. 9 (2019) 12090, https://doi.org/10.1038/s41598-019-48641-z.
[109] Z.-J. Liu, X.-X. Song, Q. Tang, Development of PEGylated $KMnF_3$ nanoparticle as a T1-weighted contrast agent: chemical synthesis, In-vivo brain MR images, and account for high relaxivity, Nanoscale 5 (2013) 5073–5079, https://doi.org/10.1039/c3nr00721a.
[110] X. Qian, X. Han, L. Yu, T. Xu, Y. Chen, Manganese-based functional nanoplatforms: nanosynthetic construction, physiochemical property, and theranostic applicability, Adv. Funct. Mater. 30 (2020) 1907066, https://doi.org/10.1002/adfm.201907066.
[111] B. Ding, P. Zheng, P.A. Ma, J. Lin, Manganese oxide nanomaterials: synthesis, properties, and theranostic applications, Adv. Mater. 32 (2020) 51905823, https://doi.org/10.1002/adma.201905823.
[112] J.E. Mertzman, S. Kar, S. Lofland, T. Fleming, E. Keuren, Y.Y. Tong, S.L. Stoll, Surface attached manganese–oxo clusters as potential contrast agents, Chem. Commun. (2009) 788–790, https://doi.org/10.1039/b815424d.
[113] D. Pan, A.H. Schmieder, S.A. Wickline, G.M. Lanza, Manganese-based MRI contrast agents: past, present, and future, Tetrahedron 67 (2011) 8431–8444, https://doi.org/10.1016/j.tet.2011.07.076.
[114] D. Pan, A.H. Schmieder, S.D. Caruthers, A.H. Schmieder, S.A. Wickline, G. M. Lanza, Revisiting an old friend: manganese-based MRI contrast agents, WIREs Nanomed. Nanobiotechnol. 3 (2011) 162–173, https://doi.org/10.1016/j.tet.2011.07.076.
[115] S. Shao, V. Rajendiran, J.F. Lovell, Metalloporphyrin nanoparticles: coordinating diverse theranostic functions, Coord. Chem. Rev. 379 (2019) 99–120, https://doi.org/10.1016/j.ccr.2017.09.002.
[116] L. Guan, F. Liu, C. Zhang, W. Wang, J. Zhang, Q. Liang, Porphyrin-based metal–Organic frameworks for Cancer theranostics, Adv. Sens. Energy Mater. 3 (2024) 100123, https://doi.org/10.1016/j.asems.2024.100123.
[117] K. Choi, D.-H. Lee, W.-D. Jang, Supramolecular micelle from amphiphilic Mn(III)-porphyrin derivatives as a potential MRI contrast agent, Bull. Korean Chem. Soc. 31 (2010) 639–644, https://doi.org/10.5012/bkcs.2010.31.03.639.
[118] X. Liu, G. Yang, L. Zhang, Z. Liu, Z. Cheng, X. Zhu, Photosensitizer cross-linked nano-micelle platform for multimodal imaging guided synergistic photothermal/photodynamic therapy, Nanoscale 8 (2016) 15323–15339, https://doi.org/10.1039/C6NR04835H.
[119] Z. Zhang, R. He, K. Yan, Q. ni Guo, Y. guo Lu, X. xia Wang, H. Lei, Z. ying Li, Synthesis and *in vitro* and *in vivo* evaluation of manganese(III) porphyrin-dextran as a novel MRI contrast agent, Bioorg. Med. Chem. Lett. 19 (2009) 6675–6678, https://doi.org/10.1016/j.bmcl.2009.10.003.
[120] A. Hong, K.D.W. Vollett, H.-L.M. Cheng, A nitric oxide-sensing T1 contrast agent for *In vivo* molecular MR imaging of inflammatory disease, ACS Sens. 9 (2024) 5374–5383, https://doi.org/10.1021/acssensors.4c01604.
[121] S. Shao, T.N. Do, A. Razi, U. Chitgupi, J. Geng, R.J. Alsop, B.G. Dzikovski, M. C. Rheinstädter, J. Ortega, M. Karttunen, J.A. Spernyak, J.F. Lovell, Design of hydrated porphyrin-phospholipid bilayers with enhanced magnetic resonance contrast, Small 13 (2017) 1602505, https://doi.org/10.1002/smll.201602505.
[122] I.G. Meerovich, A. Brandis, G.A. Meerovich, A.A. Stratonnikov, P. Bendel, N. A. Oborotova, A. Shertz, A.Y. Baryshnikov, Study of manganese bacteriopheophorbide as a potential contrast agent for magnetic resonance tomography, Bull. Exp. Biol. Med 143 (2007) 452–454, https://doi.org/10.1007/s10517-007-0154-3.
[123] S. Qazi, M. Uchida, R. Usselman, R. Shearer, E. Edwards, T. Douglas, Manganese (III) porphyrins complexed with P22 virus-like particles as T1-enhanced contrast agents for magnetic resonance imaging, JBIC, J. Biol. Inorg. Chem. 19 (2014) 237–246, https://doi.org/10.1007/s00775-013-1075-4.
[124] M. Chen, X. Liang, Dai Z, Manganese(III)-chelated porphyrin microbubbles for enhanced ultrasound/MR bimodal tumour imaging through ultrasound-mediated microto-nano conversion, Nanoscale 11 (2019) 10178–10182, https://doi.org/10.1039/c9nr01373c.
[125] D. Pan, S.D. Caruthers, G. Hu, A. Senpan, M.J. Scott, P.J. Gaffney, S.A. Wickline, G.M. Lanza, Ligand-directed nanobialys as theranostic agent for drug delivery and Manganese-based magnetic resonance imaging of vascular targets, J. Am. Chem. Soc. 130 (2008) 9186–9187, https://doi.org/10.1021/ja801482d.
[126] L. Jing, X. Liang, X. Li, Y. Yang, Z. Dai, Covalent attachment of Mn-porphyrin onto doxorubicin-loaded poly(lactic acid) nanoparticles for potential magnetic resonance imaging and pH-sensitive drug delivery, Acta Biomater. 9 (2013) 9434–9441, https://doi.org/10.1016/j.actbio.2013.08.018.
[127] T.D. MacDonald, T.W. Liu, G. Zheng, An MRI-sensitive, non-photobleachable porphysome photothermal agent, Angew. Chem., Int. Ed. 53 (2014) 6956–6959, https://doi.org/10.1002/anie.201400133.
[128] J.F. Lovell, C.S. Jin, E. Huynh, H. Jin, C. Kim, J.L. Rubinstein, W.C.W. Chan, W. Cao, L.V. Wang, G. Zheng, Porphysome nanovesicles generated by porphyrin bilayers for use as multimodal biophotonic contrast agents, Nat. Mater. 10 (2011) 324–332, https://doi.org/10.1038/nmat2986.
[129] L. Jing, X. Liang, X. Li, L. Lin, Y. Yang, X. Yue, Z. Dai, Mn-porphyrin conjugated Au nanoshells encapsulating doxorubicin for potential magnetic resonance imaging and light triggered synergistic therapy of cancer, Theranostics 4 (2014) 858–871, https://doi.org/10.7150/thno.8818.
[130] H. Zhang, X.-T. Tian, Y. Shang, Y.-H. Li, X.-B. Yin, Theranostic Mn-porphyrin metal-organic frameworks for Magnetic resonance imaging-guided nitric oxide and photothermal synergistic therapy, ACS Appl. Mater. Interfaces. 10 (2018) 28390–28398, https://doi.org/10.1021/acsami.8b09680.
[131] J. Bao, X. Wang, Y. Shi, J. Cheng, J. Bao, X. Zu, J. Li, D. Fan, Q. Xia, Multifunctional Hf/Mn-TCPP metal-organic framework nanoparticles for triple-modality imaging-guided PTT/RT synergistic cancer therapy, Int. J. Nanomed. 15 (2020) 7687–7702, https://doi.org/10.2147/IJN.S267321.
[132] H. Zhang, X.-B. Yin, Mixed-ligand metal–organic frameworks for all-in-one theranostics with controlled drug delivery and enhanced photodynamic therapy, ACS Appl. Mater. Interfaces 14 (2022) 26528–26535, https://doi.org/10.1021/acsami.2c06873.
[133] X. Liu, G. Yang, L. Zhang, Z. Liu, Z. Cheng, X. Zhu, Photosensitizer cross-linked nano-micelle platform for multimodal imaging guided synergistic photothermal/photodynamic therapy, Nanoscale 8 (2016) 15323–15339, https://doi.org/10.1039/C6NR04835H.
[134] X. Liang, X. Li, L. Jing, X. Yue, Z. Dai, Theranostic porphyrin dyad nanoparticles for magnetic resonance imaging guided photodynamic therapy, Biomaterials 35 (2014) 6379–6388, https://doi.org/10.1016/j.biomaterials.2014.04.094.
[135] M. He, Y. Chen, C. Tao, Q.Q. Tian, L. An, J. Lin, Q.Q. Tian, H. Yang, S. Yang, Mn-porphyrin-based metal-organic framework with high longitudinal relaxivity for magnetic resonance imaging guidance and oxygen self-supplementing photodynamic therapy, ACS Appl. Mater. Interfaces. 11 (2019) 41946–41956, https://doi.org/10.1021/acsami.9b15083.
[136] S.-S. Wan, Q. Cheng, X. Zeng, X.-Z. Zhang, A Mn(III)-sealed metal–organic framework nanosystem for redox unlocked tumor theranostics, ACS Nano 13 (2019) 6561–6571, https://doi.org/10.1021/acsnano.9b00300.
[137] R. Canaparo, G. Varchi, M. Ballestri, F. Foglietta, G. Sotgiu, A. Guerrini, A. Francovich, P. Civera, R. Frairia, L. Serpe, Polymeric nanoparticles enhance the sonodynamic activity of meso-tetrakis (4-sulfonatophenyl) porphyrin in an *in vitro* neuroblastoma model, Int. J. Nanomed. 8 (2013) 4247–4263, https://doi.org/10.2147/IJN.S51070.
[138] G. Varchi, F. Foglietta, R. Canaparo, M. Ballestri, F. Arena, G. Sotgiu, A. Guerrini, C. Nanni, G. Cicoria, G. Cravotto, S. Fanti, L. Serpe, Engineered porphyrin loaded core-shell nanoparticles for selective sonodynamic anticancer treatment, Nanomedicine 10 (2015) 3483–3494, https://doi.org/10.2217/nnm.15.150.
[139] P. Huang, X. Qian, Y. Chen, L. Yu, H. Lin, L. Wang, Y. Zhu, J. Shi, Metalloporphyrin-encapsulated biodegradable nanosystems for highly efficient Magnetic resonance imaging-guided sonodynamic cancer therapy, J. Am. Chem. Soc. 139 (2017) 1275–1284, https://doi.org/10.1021/jacs.6b11846.
[140] B. Du, X. Yan, X. Ding, Q. Wang, Q. Du, T. Xu, G. Shen, H. Yao, J. Zhou, Oxygen self-production red blood cell carrier system for MRI mediated cancer therapy: ferryl-Hb, sonodynamic and chemical therapy, ACS Biomater. Sci. Eng. 4 (2018) 4132–4143, https://doi.org/10.1021/acsbiomaterials.8b00497.
[141] Y. Xu, C. Li, X. Wu, M.-X. Li, Y. Ma, H. Yang, Q. Zeng, J.L. Sessler, Z.-X. Wang, Sheet-like 2D manganese(IV) complex with high photothermal conversion efficiency, J. Am. Chem. Soc. 144 (2022) 18834–18843, https://doi.org/10.1021/jacs.2c04734.